Department of Precision and Microsystems Engineering

Distributed optical sensor surface concept for planar object detection

Using optical fibers as a vision distributor

R.A.J.F. Fritz

Report no : 2021.018
Coaches : Dr. ir. R.A.J. van Ostayen
: Dr. ir. J.F.L. Goosen
Specialisation : Mechatronic System Design
Type of report : Master Thesis
Date : 3 March 2021

Distributed optical sensor surface concept for planar object detection

Using optical fibers as a vision distributor

by

R.A.J.F. Fritz

to obtain the degree of Master of Science
at the Delft University of Technology,
to be defended publicly on Monday March 22, 2021 at 13:30 CET.

Student number:	4429311	
Project duration:	Oktober, 2019 – March, 2021	
Thesis committee:	Dr. ir. R.A.J. van Ostayen,	TU Delft, supervisor
	Dr. ir. J.F.L. Goosen,	TU Delft, supervisor
	Dr. N. Bhattacharya,	TU Delft

This thesis is confidential and cannot be made public until March 22, 2023.

TU Delft

Abstract

With the ever-increasing demand for a more efficient production process, the thickness of silicon wafers for the solar cell industry has shown a decreasing trend over the years. This makes the substrates more and more fragile, with an increasing breakage rate as a result. The breakage is caused by mechanical contact during the handling of the thin wafers. Research at the TU Delft has been done on contactless handling, using air bearings and actuators. A suitable and integrated sensor in the air bearings would complete the package of actuator and sensor. This would make it more attractive for manufacturers to switch to the contactless handling principle. In Fig. 1, the principle of an integrated sensor in an air bearing transport system is schematically drawn.

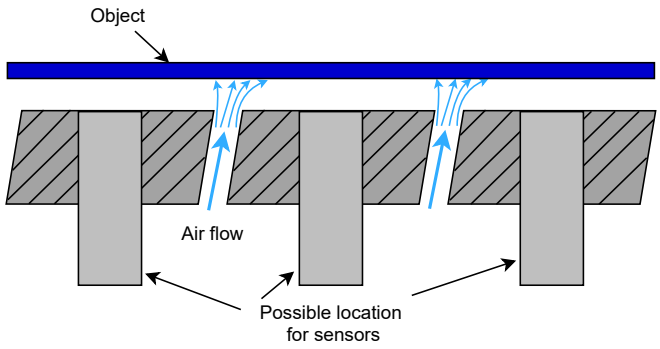

Figure 1: Possible placement and integration of a sensor in an air bearing. Thickness of the air layer not in scale.

Such a sensor has to be distributed across the plane of the air bearing actuator, to track the motion of objects flying above it. Previous work on such a distributed sensor has been done where for example photodiodes, but also camera vision sensors were looked at. Regular camera vision sensors require a direct line of sight onto the plane it needs to measure. A proposed method to distribute the vision of a camera sensor was with the use of optical fibers placed in a grid in the measurement plane. This proved to be a promising concept, but the vision of an optical fiber is very narrow, limiting the measurement reach of each optical fiber.

In the previously designed sensor concepts, only two possible outputs of the optical fiber were measured, namely 'on' and 'off'. Where 'on' indicated that the object was above the optical fiber and 'off' indicated that the object was not above the optical fiber. This research focusses on increasing the vision, and thus the measurement reach, of an individual optical fiber. It will be investigated if a transition between the 'on' and 'off' can be achieved.

A theoretical analysis is done on increasing the measurement reach of an optical fiber. The vision of an optical fiber itself can be easily increased using an optical lens. It is however found that the vision of the optical fiber of a specific source of light is always limited to its own diameter. A light diffuser spreads out the light coming from a light source across its surface, acting as an infinite amount of light sources. This avoids the limitation that the vision of an optical fiber of a light source is limited to its own diameter.

The effects of a light diffuser on the vision of an optical fiber is experimentally tested. A test setup is designed that can simulate the motion of a moving rectangular object that resembles a solar cell. The transmission of the light source into the optical fiber is simulated and measured. The simulation is performed by taking pictures with a camera of the created light spot through the diffuser by the light source. An optical fiber can then be simulated by combining the intensity values of a few pixels, which combined are the same size as the optical fiber. This way, an infinite amount of optical fibers and their optimal position with respect to the light source can be simulated. The optimal position was found to be $9.2mm$ from the light source but

this is dependant on the size of the created light spot. The received transmission signal from the simulation is compared with the received transmission of an actual optical fiber and showed similar behaviour. In Fig. 2, the experimentally received transmission trends for three different angles of motion of the object can be seen.

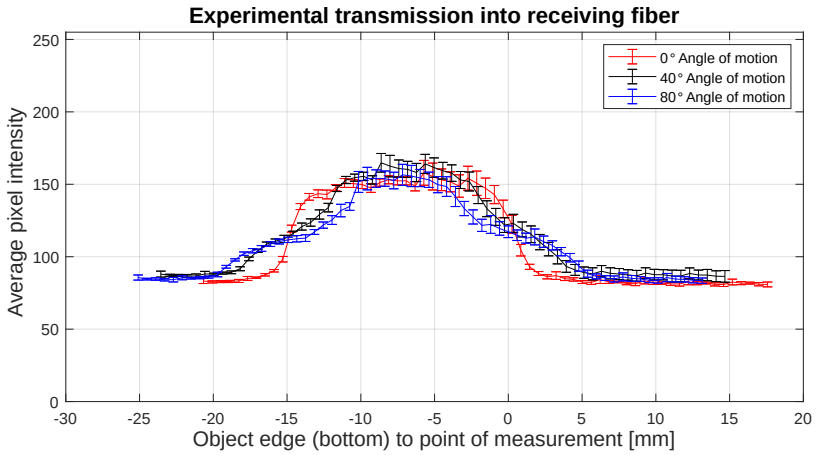

Figure 2: The experimental transmission into a receiving optical fiber for three angles of motion of the object. The drawn lines are the averages of the eleven measurements done, where the one-sigma uncertainty for each point is indicated by the size of the marker.

From the figure it can be clearly seen that there are two main intensity levels, these are the 'on' and 'off' signals as found in previous research. The two intensity levels are however connected by a transition going from low to high and from high to low intensity. This already shows that the measurement reach of the optical fiber has been increased. It can also be seen that the transition between the two intensity levels is different for each angle of motion, allowing to also measure the angle of motion of the object, besides only the position of the object.

The transmission trends from Fig. 2 for the three angles of motion can be extrapolated to all 360 degrees angles of motion. The result is the surface plot seen in Fig. 3. In this plot, a slice can be made at any angle of motion resulting in the transmission trend line for that specific angle of motion.

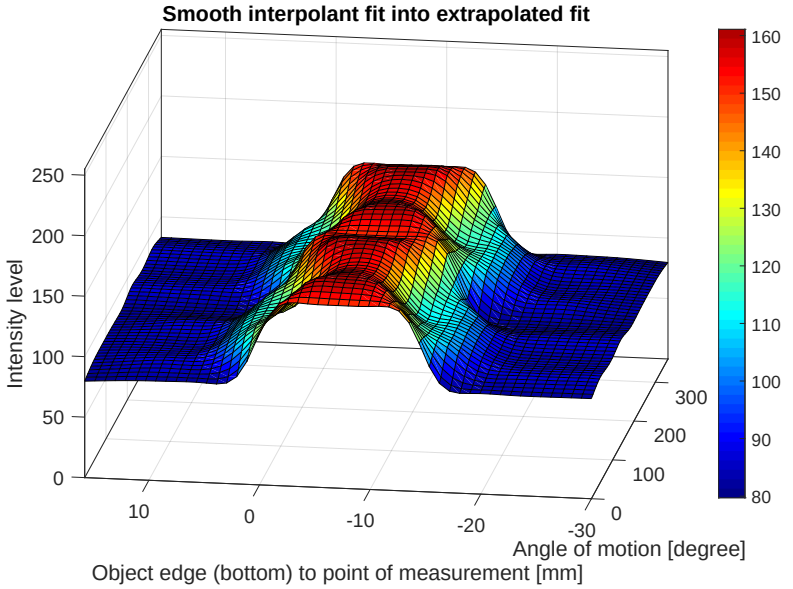

Figure 3: Surface plot of all the possible transmission trends received by the optical fiber. Every possible intensity level received by the receiving optical fiber can be traced back to object edge position and angle of motion.

To finalize and validate the concept of the distributed sensor, the experimentally received transmission of the optical fiber is given as input into the inverse data-matrix that can be made out of the surface seen in Fig. 3. Any range of subsequent points of intensity received by the optical fiber is successfully calculated back to object position and direction of motion, only making use of one set of light source and receiving optical fiber. The measurement reach of a single optical fiber lies between $2.25mm$ and $7.2mm$, depending on the angle of motion of the object. The one-sigma uncertainty in determining the angle of motion is found to be on average 4.8 degrees across all angles of motion of the object. The one-sigma uncertainty in position is found to be anywhere between $0.06mm$ and $1.2mm$, depending on the motion direction of the object.

In conclusion, the measurement reach of an optical fiber has been successfully increased resulting in a measurable transition between the low and high intensity levels. The sensor concept has been validated by feeding the observed intensity levels back as input and traced this back to object position and motion direction. This thesis only looked at one set of light source and receiving optical fiber, a so called 'building block' of the full sensor system. The actual sensor would consist of many building blocks, which all would have a positive impact on the total accuracy of the measurement system.

Contents

1

Introduction

When thinking of optical fibers, people often limit themselves to the use of large cables across oceans for our internet connection, as seen in Fig. 1.1a, and other data transfer such as fast internet to their house. Optical fibers can however also be used as a strain, pressure and temperature sensor, for example along large sections of a pipeline transporting oil and gas, like in Fig. 1.1b [18, 37]. A novel use of optical fibers as described in this thesis is in a distributed sensor for edge detection, which can be integrated into a contactless handling system. A possible application would be in an air bearing transport or positioning system for handling thin substrates such as solar cell wafers and flat panel displays.

In this introductory chapter, the motivation for such a novel sensor is discussed. Other possible and existing methods for planar object detection are investigated. A starting point for this research is given. This chapter is concluded by stating the research objective and the focus of this thesis.

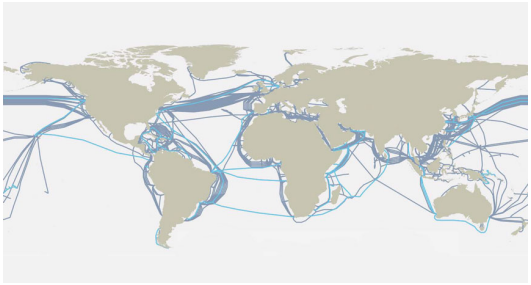

(a) Fiber optic cables across the oceans [43]

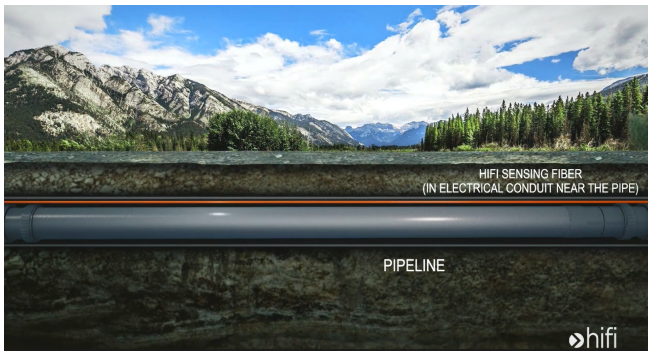

(b) Optical fiber on an oil pipeline [14]

Figure 1.1: Uses of fiber optics

1.1. Motivation

With the increasing energy consumption in the world and the ambition set by the United Nations to be carbon-neutral in 2050, the demand for clean energy is rising. Solar energy using photovoltaic (PV) solar cells is one of the ways to produce clean energy.

Silicon wafers used for the production of solar cells are thinner than wafers used for the production of microchips, with solar cells having a thickness of around 180 μm. Thinner silicon wafers would reduce the production cost due to the material requirements and would increase the efficiency of the solar cell. According to a recent study by Liu et al. [27] an optimum thickness of the silicon wafer would be 50μm. With current optimized manufacturing methods, the breakage rate of 160 μm thick wafers is around 1.5 % [13]. With the desired decrease in thickness, the breakage rate significantly increases, as seen in Fig. 1.2a, up to above 20 % with a thickness of 80 μm. This increased breakage rate is one of the reasons the wafer thickness used for

solar cells has not decreased since 2009 [1]. In Fig. 1.2b, it can be seen that in each yearly report of the International Technology Roadmap for Photovoltaic, the predicted future thickness of the wafers is increased due to this problem not being resolved, even in the most recent report [2].

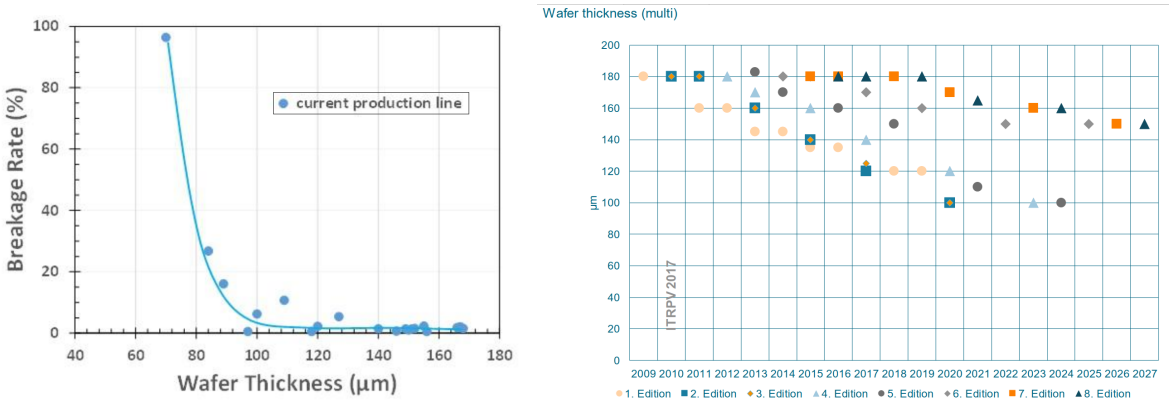

(a) Increase in breakage rate with decreasing wafer thickness [13]

(b) Increase in the predicted wafer thickness of the years [1]

Figure 1.2

The problem of the high breakage rate of the silicon wafer is caused during the handling of the solar cells [5, 49]. The handling of the wafers is mostly done by a pick and place machine and a conveyor belt. Both of these methods of transportation have a chance of breaking the wafer and adding impurities to the wafer, resulting in a possible malfunction of the printed devices [6]. Advances in decreasing the thickness of the wafer are limited by the handling of the wafers. Manual reconstruction of broken solar panels is done to decrease the loss rate as seen in Fig. 1.3.

Figure 1.3: Broken solar panel reconstruction [38]

A possible solution to reduce the breakage of the substrates is the use of an air bearing system that levitates the to be transported object. Work has been done in the PhD research by Wesselingh [50] and Vuong [48] and in the Master's thesis projects by Voorrips [47], Vagher [46] and Snieder [40] on air bearings for the levitation of substrates. Several prototypes have shown successfully that this is a feasible solution for the transportation of thin silicon wafers.

1.2. Integrated sensor

Just an air bearing is however not the solution. A suitable sensor is needed to transform an air bearing system into an air transport system, for example for the transportation and placement of solar cell silicon wafers. It is desired to have a continuous sensor system that can track wafers coming from an operating station to the next operating station in the assembly steps of the solar cell. There are several options where the sensor can be

placed to view the wafer, namely to the side of the wafer, to the top of the wafer and to the bottom of the wafer.

In Fig. 1.4 a schematic representation of an air bearing can be seen. The blue object is floating on a thin layer of air that comes out of the air actuator indicated by the dashed grey blocks. A sensor system from the sides of the transportation system is not feasible due to the thinness of the wafer and especially the solar cell. With a thickness of around 100 to 200 μm a small offset of the air bearing could lead to the wafer not being detected.

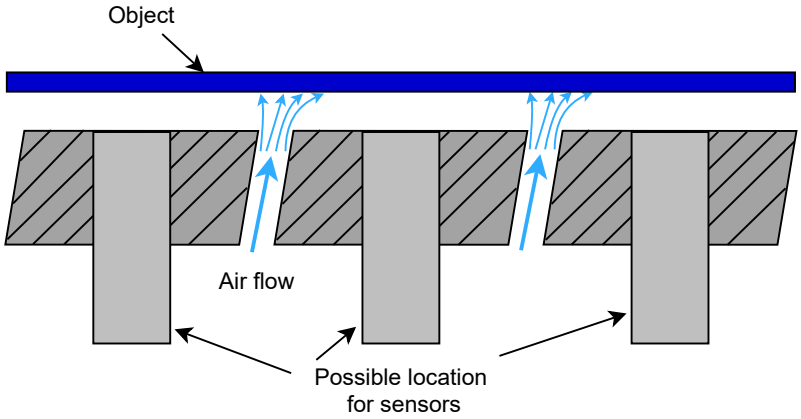

Figure 1.4: Possible placement and integration of a sensor system in an air bearing. Thickness of the air layer not in scale.

A camera system tracking the wafer position from the top of the transportation system could be possible. Cameras with image recognition can be used to track the wafer position and orientation. Free space above the wafer would be needed for a clear vision of the cameras. This limits the application of production facilities on the top surface of the wafer. Moving robot arms or any other type of obstruction could interfere with the image recognition, resulting in a wrongly detected wafer. Another drawback of topside image recognition using cameras is the speed at which the image recognition script can be processed. In the master thesis of Vagher [46] the achieved bandwidth was 60 Hz.

This leaves a sensor from the bottom as a promising solution worth investigating. In Fig. 1.4, possible sensors are placed inside the schematic representation of the air bearing. If a sensor could be integrated into the air bearing actuation system, a contactless handler is achieved, instead of a contactless actuator requiring a separate sensor system. In the master thesis of Voorrips [47], Linear Sensor Arrays were used to sense the position and height of the wafer. This project was continued by three groups of bachelor students using optical fibers to transport the signal to a sensor where multiple fibers were read out in a grid [8, 16, 23]. The prototype of the third bachelor group can be seen in Fig. 1.5. The concept of optical fiber bundles on a CMOS or CCD sensor proved to be promising.

1.3. Review on bottom side sensors

This section explains the possible types of sensors that can be used from the bottom side of the system to keep track of the wafer position. A limiting factor is that the working distance of the sensor location to the to be sensed object is very small, in the same order as the levitation height of the air jets of approximately 10 μm. A lot of possible principles can be used, like capacitive sensors, ultrasonic distance sensors, pressure sensors and various optical sensors. The current design choice is the use of an optical vision sensor looking through optical fibers. In the following subsections, some possible sensor solutions are analysed. More solutions are possible however, the use of a vision sensor in combination with optical fibers that distribute the vision has not been done before and the focus will be on this choice.

1.3.1. Ultrasonic sensors

Ultrasonic sensors can be used to detect an upcoming object. The working principle would be similar to that of in cars, namely that a sound transmission is sent which bounces off an object back into the reception sensor. The time of flight can be determined to calculate the distance of the object [19, 33, 39]. It is thus

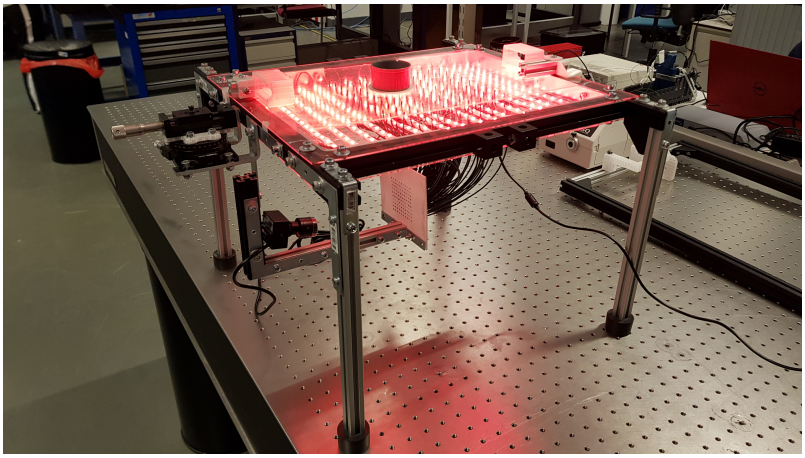

Figure 1.5: The prototype of the third bachelor group [8]

possible to sense the fly height of the silicon wafer. The downside is the low resolution in x-y plane, an object distance is received which can be in any direction. A proposed method by Shin et al. [39] improves the efficiency of the ultrasonic sensors by using modulation of the sound pulses. This principle of modulating a source could be used for other types of sensors, for instance in optical sensors.

1.3.2. Optical sensors

There is a large variety of optical sensors, not all are useful for the intended application. Position sensing detectors (PSD) for example are used to detect the position of a light spot on the sensor [36]. This would thus require a laser beam to get an accurate reading, while for example, a photodiode would not. Photodiodes, like the previous explained ultrasonic, would require a large number of sensors to cover a certain area. An Optical vision sensor is an alternative that would require fewer sensors to cover the same area. The discussed optical sensors all require a light source for their function. The light source will be discussed first followed by the optical sensors themselves.

Light source

The light source can be either from the topside or the bottom side of the solar cell. A bottom side light source would make use of the reflectivity of the wafer surface to reflect light back into a receiving sensor. When the source is from the topside, the sensor would be "on" (light fall into the sensor) and "off" when the light is blocked by the solar cell. With a bottom side source, the receiving sensor is always "off" and goes "on" when the light is reflected by the solar cell into the sensor. For choosing where the light source needs to be placed, the same argument can be used from section 1.2 for the position of the sensor, namely that the top side above the wafer would be preferred to be free. Moving objects like robot arms for the production process would cause a shadow if the light source is on the top side of the wafer. This could lead to a wrongly detected wafer. A bottom side light source would not suffer from this problem.

An option for a bottom side light source could be an array of small LEDs directly into the object plane, lighting only small sections. A variation of this would be to couple light coming out of the LEDs into the optical fiber and place the other end of the optical fiber in the measurement plane. Another option could be only a small amount of LEDs placed further away from the object plane covering larger sections per LED.

Photodiodes

An option that was investigated in a previous master project by Voorrips [47] was the use of photodiodes. Photodiodes generate an electric current based on the incoming light. This does mean that there needs to be a light source that produces light. Berlin et al. [3] designed a paper mover using air jets, with photodiodes as the sensor to locate the paper edges. In Fig. 1.6 such a module can be seen, where the black lines are Selfoc lens arrays with photodiode sensors beneath them.
The price of a photodiode can vary from a few cents to a euro per piece, depending on the quality and size, making them not too expensive. Printed circuit boards, like an Arduino, are used to connect the photodiodes.

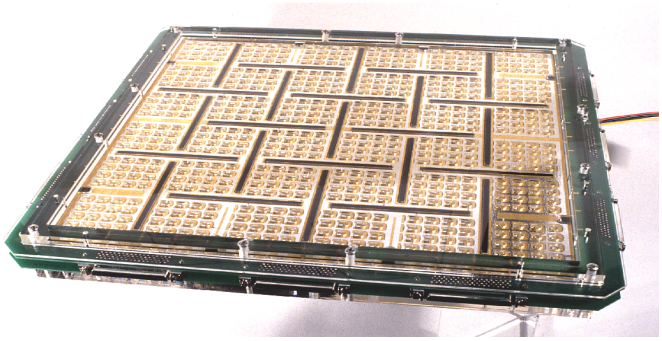

Figure 1.6: An actuation module with integrated sensor system using photodiodes [3]

CCD/CMOS Vision Sensor

Optical vision sensors, or cameras, can be used in combination with image recognition to track the position of an object. A big advantage of using a single camera sensor instead of large arrays of photodiodes is that only one sensor can be used to cover a large area. This eliminates the need for complex and complicated connector schemes for a large number of sensors.

A camera could be used to look directly at the measurement plane to track the position of the solar cell. Holz and Baudisch [15] made a touchscreen that can recognise the fingerprints of the persons touching the screen. It makes use of a fiber optic plate, a plate made out of millions of small optical fibers. The ridges of a finger will appear as dark due to the light being blocked, while at no ridge the light gets reflected back through the fiber and thus creates a bright spot. In Fig. 1.7, the setup can be seen. An interesting point is that the light source is at the side, but gets reflected by a mirror onto the measurement plane. The high-resolution camera senses the fingerprint and by the use of image processing, the fingerprint is compared to known fingerprints.

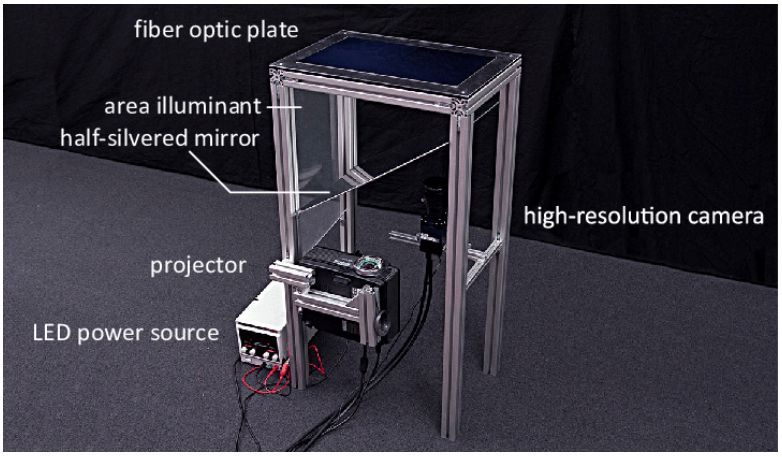

Figure 1.7: Fiberio setup of the touchscreen with fingerprint recognition [15]

A downside of looking with the camera directly at the measurement plane is that the vision of the camera is limited by the distance from the camera to the measurement plane. A larger view can be achieved with the use of a wide-angle lens, or by moving the camera further away from the measurement plane.

Displaced and distributed vision sensor

A newly looked at method is a displaced and distributed vision sensor, as done previously at the TU Delft [8, 23]. With displaced it is meant that the camera does not look directly at the to be measured object, but the vision is displaced via the use of optical fibers, requiring less room inside the actuator plane. Placing the optical fibers in a grid, in the air actuator, a distributed vision is obtained, with a minimum footprint on the air actuator. Optical fibers are chosen to displace and distribute the vision of the camera as the fibers offer the most freedom in distributing the vision of the camera sensor over for example a mirror.

A start in the development of this principle has been done by three groups of bachelor students. The experimental setup of the last bachelor group was already shown in Fig. 1.5. The working principle of the system is schematically shown in Fig. 1.8. The blue object is moving from right to left and covers the LED light source and optical fibers along its way. If the object is not above the optical fibers, no red light from the LEDs gets reflected into them and the other end of the fiber remains neutral. With the object above the optical fibers, the red light from the LEDs gets reflected by the object into the optical fibers, resulting in an output of red light. In Fig. 1.8a, a square section can be seen containing eight optical fibers. The four on the left are not covered by the object and the four on the right are. The output of the optical fibers is schematically shown in Fig. 1.8b, where the four fibers on the left are not covered and the four fibers on the right are and give a red output.

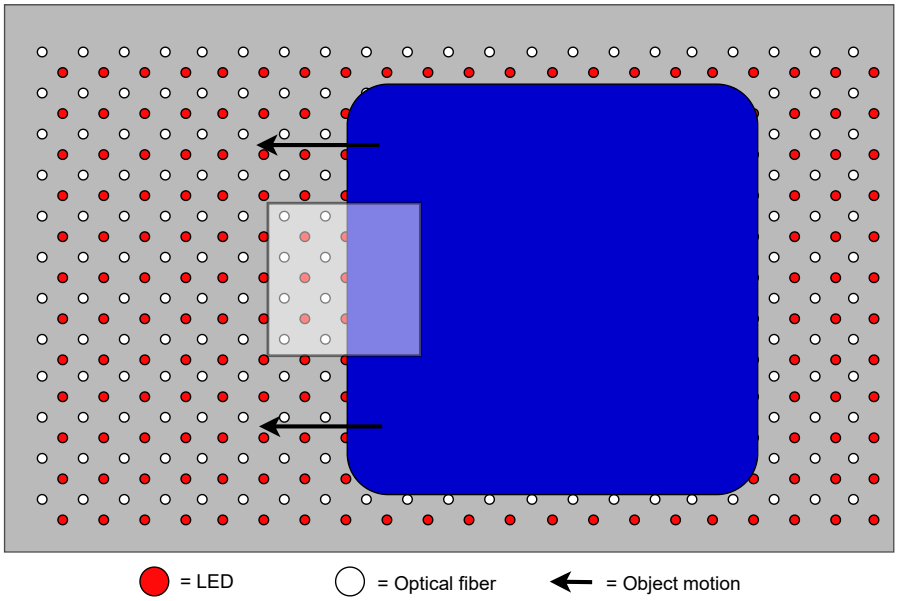

(a) Schematic of an object moving from right to left. The object reflect the light from the LEDs into the optical fibers.

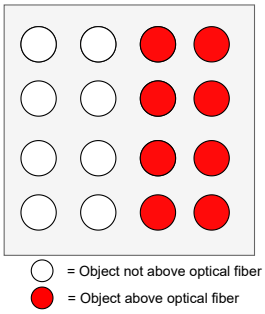

(b) Output of the optical fibers within the transparent square from (a). It can be seen that 4 of the eight optical fibers are covered by the object.

Figure 1.8: Working principle of the setup of third bachelor group.

The free ends of the optical fibers were bundled together, with a camera collecting all the outputs. This allowed a single camera to cover a large area while minimizing the footprint of the sensor on the air bearing system.

1.3.3. Conclusion sensor type

In this section, possible sensor types that could be used as bottom side sensors were discussed. Ultrasonic sensors have a low resolution in the position sensing, making them less suitable. Photodiodes work on incoming light. A bottom side light source is required, along with the photodiodes. Electronic boards are needed for the photodiodes, which can be very complicated when a large amount of sensors is used.

A solution to this is using one sensor to cover a large area. A camera vision sensor could cover a large area with only one sensor. The view of the camera sensor is still limited by the direct line of sight and the distance to the measurement plane. With its line of sight distributed by optical fibers placed in the air actuator, one sensor could cover a larger area, not limited by the line of sight of the camera. Low-resolution pixelated information is then seen by the camera. Light has to come from the bottom side, either by LEDs, or optical fibers if the actuator layer is not transparent. Reflection of the light on the wafer surface into the optical fibers gives a certain intensity seen by the camera.

The concept of using a set of optical fibers as a discrete sensor system, like the prototype demonstrator of the third bachelor group is deemed interesting enough to investigate this more thoroughly. The bachelor group only measured two intensity levels, namely high and low intensity. A lot more information on the object position could be gathered from one optical fiber if more intensity levels could be found. In Fig. 1.9, this is

schematically shown. The different intensities red would give an indication of how far the edge of the object would be from that specific optical fiber.

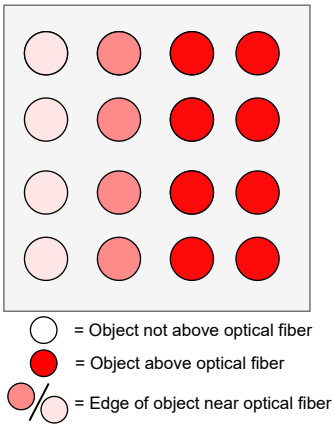

Figure 1.9: An example of how figure 1.8b could be improved, where the shaded colours of red would indicate how far the object is from that specific optical fiber.

1.4. Research Objective

In this thesis, a design concept for a new type of planar sensor will be made. With a working concept shown in Fig. 1.5 as the starting point, steps are made to optimize the view of a single optical fiber. The numerical aperture of an optical fiber is limited, with an increased measurement reach of a singular optical fiber, fewer fibers per area are needed to detect an object. Thus, an optimized view of a single optical fiber is desired to minimize the footprint of the sensor when it is implemented in, for instance, an air bearing transport system. To be suitable for use in an air bearing transport system, the surface does need to be flat and smooth.

A motion system simulating the movement of an object over an optical fiber will be needed. Image recognition software needs to translate intensity differences, caused by the overhead movement seen by the optical fiber, back to the position of the object. The design concept must be compact and portable, suitable for experiments at home. A complete sensor system will not be the objective; instead, one building block of a light source and a measurement fiber that can be expanded to a complete system will be the goal. Furthermore, a dark environment sealed from ambient light is highly desired to avoid the need for filtering out the ambient light.

The research objective is thus stated as follows:

"Design and experimental validation of a design base concept for an edge detection sensing surface with the use of optical fibers."

1.5. Thesis Outline

In this Chapter, the motivation for the research objective was given. In Chapter 2 the working principle of optical fibers is investigated. Possible suggestions on how the vision of the optical fibers can be improved are given. The next step is a theoretical analysis of the points that could improve the vision of the optical fibers. This is done in Chapter 3. In Chapter 4, the design and results of a first experimental model are given that investigates the use of diffusers as vision expander for optical fibers. A second experimental model is designed in Chapter 5 that also looks at the light transmission from a light source into an optical fiber by a reflective object. Several steps of image analysis are required on the obtained images of the second experimental model and are done in Chapter 6. In Chapter 7, data analysis is done to track the different received intensities back to a position and a movement direction of the object. The conclusion of this thesis is given Chapter 8, followed by the recommendations for further research in Chapter 9. In Appendix A, the most important MATLAB codes developed in this thesis can be found.

2

System Overview and Literature Research

This chapter discusses the points of interest on the prototype demonstrator from the third bachelor group as well the knowledge needed to improve upon them or to make it suitable to form a sensor system. This chapter will start with an overview of the working principle of optical fibers, followed by the fiber choice for use in this thesis. One of the aims of this thesis is to increase the view of the optical fibers, thus increasing their detection range. Two methods to achieve this, namely with the use of lenses and with light diffusers, are discussed based on examples found in the literature. The chapter ends with ways to optimize the readout of a bundle of optical fibers by a vision camera.

2.1. Background on Optical fibers

A key component in the design of the planar sensor system will be the optical fibers. They will transport and distribute the vision of a camera to and across the measurement surface.

Optical fibers are wires consisting of a core with a refractive index of n_1 and an outer cladding with a different refractive index of n_2. The refractive index is the ratio between the speed of light in a vacuum and in another medium. It determines how a beam of light is bent when it encounters a different medium. The transmittance of light through a fiber can occur due to the differences in the index of refraction of the two materials, which causes total internal reflection of light rays. Snell's law, as in equation 2.1 and visualized in Fig. 2.1, describes the relation between the angle of incidence and the angle of refraction. In this equation, n_1 and n_2 are the indexes of refraction of the first and second medium and θ_1 is the angle of incidence and θ_2 the outgoing angle of refraction.

$$n_1 \sin(\theta_1) = n_2 \sin(\theta_2) \tag{2.1}$$

Light travelling in the optical fiber is trapped when the angle of incidence of a light ray on the wall of the fiber core is equal to or greater than the critical angle θ_c, as shown in Fig. 2.2. The critical angle is defined when in equation 2.1, $\theta_2 = 90°$. The following equation 2.2 is received:

$$\theta_c = \arcsin(\frac{n_2}{n_1}) \tag{2.2}$$

The cone of acceptance of the optical fiber, for which rays entering the fiber within the cone will be transmitted through the optical fiber can be found by using Snell's law again on the air-fiber interface, with the angle of refraction being $90° - \theta_c$. This gives the Numerical Aperture (NA) of the fiber.

$$NA = \sin(\alpha) = \sqrt{n_1^2 - n_2^2} \tag{2.3}$$

2.1.1. Fiber types

Although the principle of fiber optics is the same, multiple types of optical fibers exist. The main differences are the material of the fiber and the mode type of the light going through the fiber.

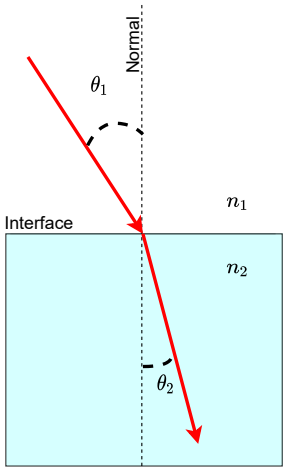

Figure 2.1: Schematic of Snell's law. The incoming ray has a certain angle and is bend at the interface between the two mediums, depending on Snell's law.

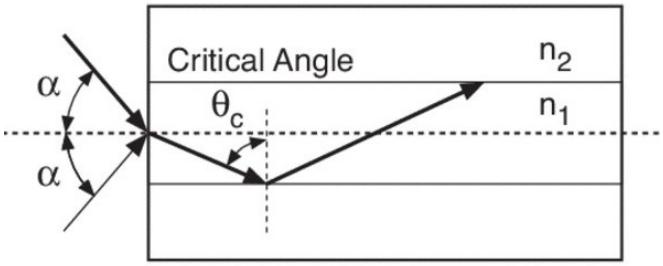

Figure 2.2: Working principle of an optical fiber [29]

The core material can be either from glass or plastic (polymers). Glass Optical Fibers (GOF) have lower losses than Plastic Optical Fibers (POF) due to higher material purity and lower power absorption. Glass fibers are however more expensive than POF and are much more difficult to handle than POF since GOF cannot be cut to size on the spot while POF can be cut on the spot. Additionally, POF are flexible while GOF break very easily and thus have to be protected against bending.

Glass Optical fibers can come in either multimode or single-mode form, whereas Plastic Optical fibers are always multimode due to their larger core size. Single-mode fibers can only transmit one mode type, namely the axial mode, while multimode fibers can transmit multiple modes due to their larger core size. In Fig. 2.3 the different modes are schematically shown. Modal dispersion limits the maximum propagation length of the multimode fiber due to the losses it causes of around 1 dB/km [22]. Modal dispersion is the difference in propagation time that signals get because the path that goes straight down the middle is shorter than the path that gets continuously reflected during its propagation along the fiber. This phenomenon can also be seen in Fig. 2.3. A new type of fiber has been recently developed, namely Graded-Index optical fibers. These differ from the step-index optical fibers as described above in that their index of refraction of the core is varying along its radius. This causes the propagation speed of light to increase along the radius of the optical fiber, so there is minimal to none modal dispersion, significantly decreasing the losses [22].

The type of fiber needed depends on the intended use and the distance the signal needs to travel. For high bandwidth, large distance transmission, for instance across oceans, single-mode fiber cables are used because of their very low signal loss of around 0.2 dB/km [32]. For shorter distances and even higher bandwidth, multimode glass fibers are chosen. Plastic optical fibers are for instance used when the travelled distance is small since their signal loss is around two orders of magnitude higher than multimode GOF [20, 31, 45]. An example of the use of POFs is for instance in vehicle applications and fast home and industrial networks.

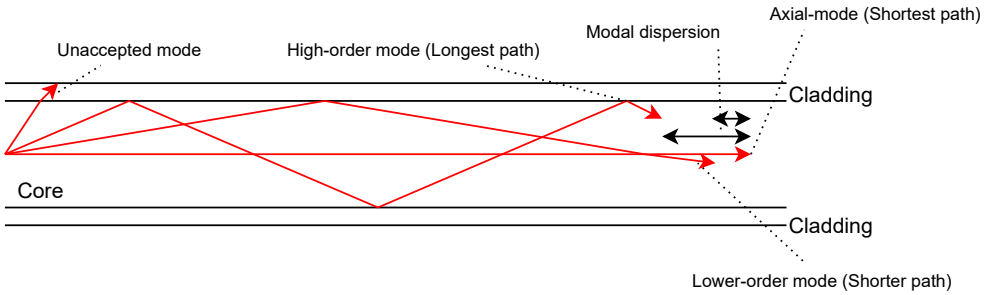

Figure 2.3: Schematic drawing of the different mode types that an optical fiber can transmit along its axis. Modal dispersion is indicated by the black arrows.

The main advantage of plastic optical fibers is their ease of use. As said, a POF can be cut on the spot and allows some bending of the wire. Next to this, due to its larger core size and high numerical aperture, low-cost LEDs can be used as the light source instead of higher-cost lasers and expensive laser to fiber couplers.

2.1.2. Fiber choice

For this intended application, the optical fibers are not used for data transmission, but instead just used to transport the light from one end of the optical fiber to the other end. The fibers will need to allow bending, as well as be able to cut the fiber on the spot without specialized tools and to be suitable for use with LEDs. This excludes glass optical fibers as both their bending and cutting is very restricted. The length of the fibers will be within the centimetre range, the higher loss rate of the plastic optical fibers is thus not an issue. A higher numerical aperture fiber would be desired, since this would allow for easier coupling from LED to fiber, and increases the range of which an object can be detected.

2.2. Microlenses

This section explains the possible lenses that can be used on the ends of the fiber. There are of course two ends of the fiber: namely one end mounted in the measurement plane, where the to be detected object is moving and the other end pointed at the camera. In order to get the most amount of information out of a single fiber, it might be desirable to have a large field of view on the end mounted in the measurement plane, so the substrate can be seen from a larger distance away compared to when no lens is used. The lenses are thus used to increase the numerical aperture of the fibers.

2.2.1. Microlens Array

The microlens arrays are mostly very compact, with little unused space between the microlenses. This is because most of the applications for such arrays, as sold by for example Thorlabs [44], is for concentrating more light into photodiodes in CCD sensors.

For the intended application in the air-bearing system, a microlens array could be an interesting option. Several other applications for microlens arrays in combination with optical fibers have been found in literature [4, 10–12]. Fukushima [10] uses a combination of a microlens array with a GRIN-rod lens as a fiber multiplexer to focus the output of several fibers into a single fiber. In the articles of Hahn and Brown et al. [4, 11, 12], a free-space optical communication technique is described. A microlens array is used to focus light into a fiber bundle, where each microlens focusses to seven fibers in a bundle.

All of the found microlens arrays have the lenses close to each other, an example is seen in Fig. 2.4 from SQS Vláknová optika [41]. The optical fibers might want to be spaced further apart in some areas of the transportation system, depending on the needed resolution. Existing arrays have not been found for that type of application.

2.2.2. Individual lenses

The most common use of a dedicated lens for a single fiber is fiber collimators. These are mounting pieces for optical fibers, consisting of single or multiple lenses in a lens holder. Fiber collimators are used to couple

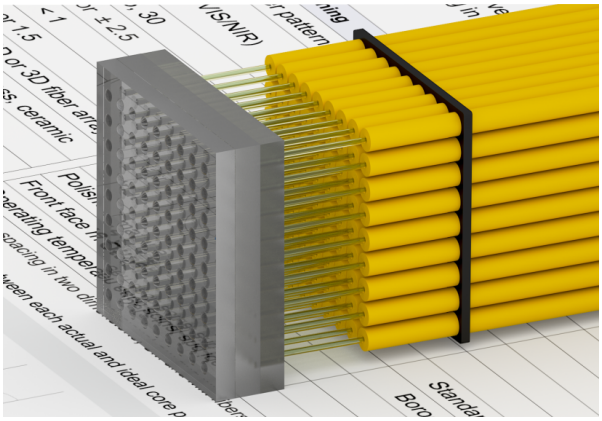

Figure 2.4: Microlens array [41]

laser light into a fiber or to focus the light coming out of the fiber into another fiber or camera sensor. Fiber collimators are relatively large and very expensive to use in large numbers, with a price between 150 to 250 euros per piece. This would make them not suitable to be used in a large array with optical fibers.

Other types of fiber couplers exist, that instead of collimating the light beam just focusses more light into the fiber. Lens assemblies as used in collimators and endoscopes are not suitable for large scale use due to their complexity and cost. A simple single interface lens would be cost-efficient, an example would be a curved surface just before the optical fiber. The microlens arrays as described in the section above are designed this way. A curved surface for a wider light input can be created for each fiber separately, by for instance heating and melting the tip of the optical fiber itself. Reshaping the tip of the plastic optical fiber is possible when slightly heated, as the material of which the fiber is made, PMMA, is thermoplastic. This means that the material softens when heated and becomes moldable.

2.3. Light Diffuser

Where lenses are used to direct the light into a specific beam pattern, diffusers spread the light in any direction. Diffusers are often used in the lighting industry in LED panels to smooth out each individual light dot of the LEDs, as seen in Fig. 2.5. This could be implemented in the sensor system by placing a diffusing layer over the optical fibers placed in the measurement plane. It could possibly increase the vision of the optical fibers, with a downside of receiving a blurred image. There are two main types of diffusers to be distinguished, namely surface diffusers and volumetric diffusers.

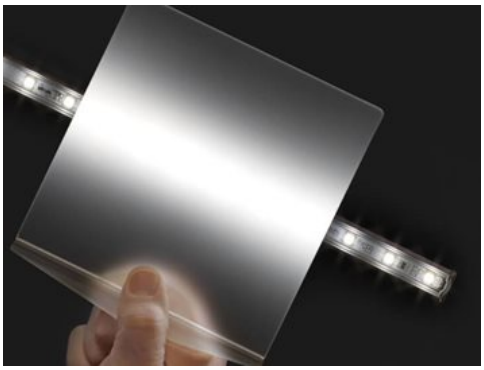

Figure 2.5: Diffusion of LED light [7]

2.3.1. Surface diffuser

Surface diffusers scatter the light based on their surface textures. The usually very small microtextures cause light to refract along a different angle at the interfaces, just like with lenses. The difference with lenses is that

a lens is designed and works from a specific point along its optical axis, while a surface filled with microstructures does not have a specific optical axis and works when the beam of light covers multiple structures. An example of a possible surface type diffuser can be seen in Fig. 2.6a.

The microstructures can vary from simple scratches made into glass or plastic to complicated and specialized surface textures. Diffusing effects of glass grounded by abrasive particles of different sizes has been investigated by Middleton [28]. He reported that the scratches made into the glass did cause the light to be diffused slightly, where finer grinds are less effective than coarser grinds, although it is far from a perfect diffuser.

A greater diffusion can be accomplished with imprinted microstructures onto the surface of for instance PMMA sheets. Lin et al. [25] imprinted micropyramids with a base width of $30\mu m$ with various angles of the sides of the pyramids onto PMMA sheets. Their research showed that the micropyramids diffuse the light to various widths depending on the angles of the pyramids. Different types of microstructures give different types of scattering in different directions, as done in [26] by Liu and Huang. An obvious downside for the use of surface type diffusers in an air bearing application is that their surface is not flat. The surface textures could cause leakage of pressurised air, this is something to consider in the design of the sensor system.

2.3.2. Volumetric diffusers

Volumetric diffusers, or also called particle diffusing type diffusers, relies on transparent particles or fillers inside the plastic mixture of the diffuser sheet to scatter light. Unlike the surface diffusers, where the scattering effect is caused at the surfaces, volumetric diffusers scatter the light inside its volume.

When light enters the diffuser, it will encounter several particles which have a different index of refraction than the base material. This will change the direction and sometimes split the incoming light ray. In Fig. 2.6b it can be seen that four rays enter the light diffuser film, which contains hollow nanoparticles, and the outgoing light gets distributed across the width of the diffuser with various angles.

A combination of surface and volumetric diffusers also exist. Where surface diffusers have a higher light transmission, volume diffusers have an enhanced haze. Both Park and Khang [30] and Huang et al. [17] report that combining both types of diffusers gives the advantages of both types.

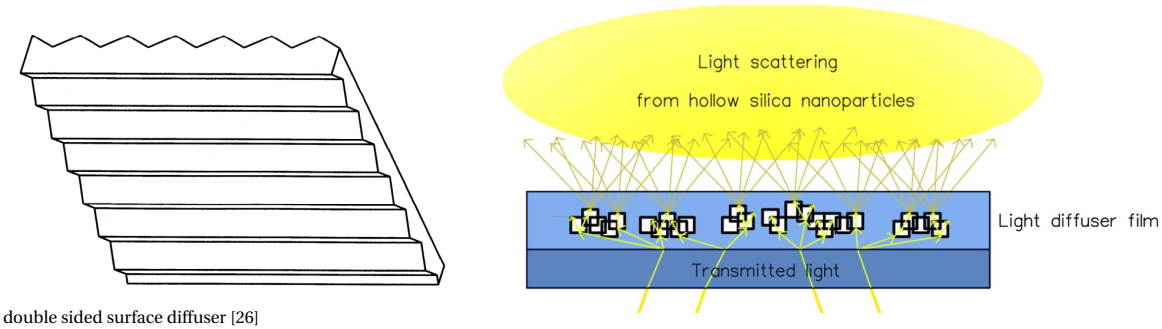

(a) A double sided surface diffuser [26]

(b) Volumetric diffuser with hollow nanoparticles [42]

Figure 2.6: Two types of diffusers: surface (a) and volumetric/particle (b) diffusers.

2.4. Fiber bundle readout

Two possible solutions to increase the view for one end of the fiber, looking at the object side, has been given, namely lenses and diffusers. For the other end of the fiber it is important that the camera can get a good view of the ends of the fibers. The camera sensor will capture an image that contains the intensity values of each fiber. A clear picture of the fiber bundle is needed to differentiate the intensities of each individual fiber.

2.4.1. Coupling to sensor

The readout of a fiber bundle can be done efficiently with a CCD or CMOS sensor. There does need to be a good connection between the sensor and the ends of the fiber bundle. It is desired to have enough spacing available to arrange the fiber bundle in a matrix for the readout. However, a larger size of the matrix will re-

quire the camera sensor to be larger, or a lens has to be used to place the camera further away, with sufficient resolution.

A disadvantage of the use of a lens is that the camera needs to be at a distance away from its objective, increasing the size of the system. An alternative to a lens is a fiber optic taper as in Fig. 2.7. The fiber optic taper can be directly glued to a CCD or CMOS sensor and the ends of the fiber bundle to the taper. This leaves more space for the fiber bundles to be organized in a matrix.

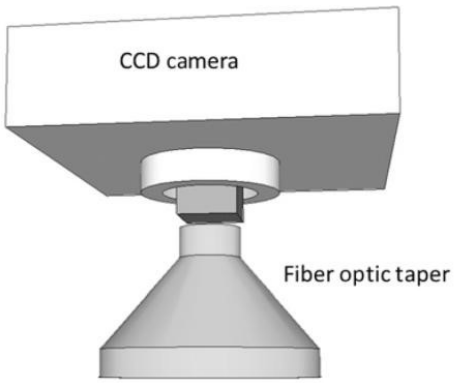

Figure 2.7: A fiber optic taper connected to a CCD sensor[21].

The tapers can vary in size and magnification, depending on the manufacturer a size up to 150 mm in diameter with magnification is possible. Prices vary greatly, from €1000,- for a small taper (Edmund Optics) to US$900,- for a larger taper (Alibaba). Due to the cost and complexity of coupling the taper directly to the camera sensor, a regular camera with a lens is used.

2.4.2. Camera sensor

Various types of camera sensors are available that would be suitable for the readout of the bundle of optical fibers. To directly read out and process the camera images, a USB connection from the camera to the computer is required. This gives the advantage that the camera settings can be controller from the computer, given consistent images. Consumer DSLR cameras provide high-quality images however, they are large in size, costly and require special software to function as a direct USB camera.

USB camera's for various applications exist. From webcams for video call purposes to camera surveillance webcams and high quality, high speed and high priced scientific cameras.

For a complete design of a planar object detection sensor as proposed, a high frame rate camera would be needed to reach high bandwidths. This thesis only focusses on the optimization of the view of a single fiber and the experimental validation of the concept of planar object detection through the use of optical fibers. Specialized cameras will not be needed, it will however be important that the camera can be controlled and set from a computer to give consistent images. The previous bachelor group bought a webcam from ELP that is capable of capturing video's in 60 frames per seconds in 720p HD and 30 frames per seconds in 1080p full HD. This webcam will be used in this thesis as well.

2.4.3. Image processing

The received images by the camera will need to be processed in order to translate intensity differences of the fiber ends to object position. The image received by the camera would be similar to that as seen in Fig. 2.8 by the third bachelor group. The first processing steps are to eliminate the background noise and to translate the image into greyscale.

Depending on how differentiating the received greyscales are, different methods can be used. A processing step to a binary image can be done if the received greyscales are not differentiating enough from each other. This is done in the earlier discussed system by Holz and Baudisch [15] to recognize fingerprints in

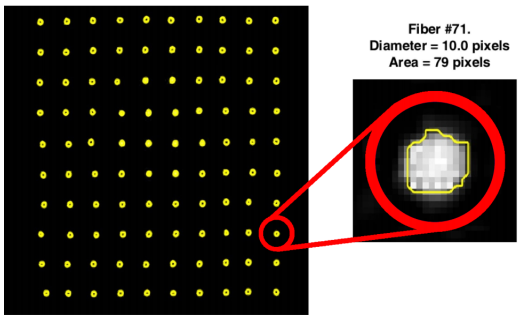

Figure 2.8: Image received by the third bachelor group [8]

section 1.3.2. This will give a clear on/off signal with an "on" if the object if covering a receiving fiber. The position of the object can then be determined by coupling the active fibers to their known position in the measurement plane.

If the greyscales differ sufficiently from each other, the greyscale of each fiber can be used to get extra information on object position. The brighter the spot of a fiber end is, the closer the object edge is to that receiving fiber. A fully covered fiber on the measurement plane will give the brightest spot, while a totally uncovered fiber will give the darkest spot. An experiment is required to couple the intensity to the distance between the object edge and the receiving fiber. When this is known, image recognition can be done on the entire grid of the fibers with the greyscale of each fiber as extra information on object position.

2.5. Conclusion

In this chapter the working principle of optical fibers is explained. The related physics regarding light transmission through a fiber is discussed. The type of fiber used in this thesis is given, namely plastic optical fibers due to their ease of handling. Optical fibers have however a limited view and microlenses and diffusers have the possibility to enhance that view. A more in-depth analysis of these two methods is needed. This covered one end of the optical fibers. The other ends of the optical fibers will be read out by a camera with a direct connection to a computer. The last step needed to complete the synthesis of the new sensor system is to do image processing on the received pictures.

3

Theoretical analysis

In this chapter, the modelling of a light source and an optical fiber receiving the light from the light source is done. Parameters that have an effect on the field of view of an optical fiber will be investigated. With an increased view, a larger area can be scanned with a single fiber, decreasing the number of fibers needed for a specific area. First, it is explained which type of optical domain is best suited for modelling this problem. Then, the effects of fiber placement and lenses are modelled, first in an analytic approximation, then compared with the results of simulations done in COMSOL Multiphysics. After that, the alternative to lenses is discussed, namely diffusers.

3.1. Field of study

For modelling the propagation of light, different methods can be used, namely geometrical ray optics, wave optics and quantum optics. These different methods vary in complexity with ray optics being the most simplified and quantum optics the most complex.

Geometrical optics describes the light as rays coming from a light source travelling in straight lines. The rays change direction at interfaces between two different media, according to the laws of refraction and reflection. The main equation is Snell's law (eq. 2.1), as explained in section 2.1 and visualized in Fig. 2.1. Geometrical optics cannot describe diffraction or interference of light waves. In general, geometrical optics holds if the smallest feature size of the to be modelled object is much larger than the wavelength of the light.

In wave optics, the light propagates as a wave. The propagation is described by Maxwell's equations of electromagnetic waves. The electric and magnetic fields are varying. Wave optics can describe the phenomenons of diffraction and interference, which geometrical optics can not. These effects need to be taken into account when the smallest feature size of the to be modelled object is in the same order as the wavelength of the light.

Quantum optics also describes the propagation of light as a wave; however, that it consists of small particles, namely photons. Lasers are an application of the field of quantum optics.

The smallest feature size in this study is far greater than the wavelength of the light of around $600nm$. The effects of diffraction and interference will be assumed to be of negligible impact and not worth the extra computational time, thus this study will be in the geometrical optics domain.

3.2. Analytical model without lenses or diffuser

Various models will be analysed, in this section without lenses to see how much light is transmitted from a light source to a receiving fiber, placed at various distances from each other and from the measurement plane. For the light source, a duplicate fiber is modelled with equal specifications as the receiving fiber in which light is travelling that is within the accepted modes of the optical fiber. The duplicate fiber is used as a source of light in the measurement plane instead of a LED placed there because it will visualize the cone of acceptance of both optical fibers. The fiber guiding light to the measurement plane will be called the transmitting fiber. The created spot of light coming out of the transmitting fiber will be the same size as what the receiving fiber

can maximally receive.

In Fig. 3.1, the first model can be seen. It is a 2D model consisting of two optical fibers, a PMMA plate in which the fibers are pushed into, an object which acts as a mirror, reflecting the light into the receiving fiber and an air gap between the object and the PMMA plate. The air gap represents the $10\mu m$ layer of pressurised air of an air bearing. The object represents a reflective object, similarly to thin wafers, solar cells and other thin flat objects. The starting point of the light rays is a light source at the transmitting fiber. A standard type of plastic optical fiber is chosen with a diameter of $1mm$. The specifications of the fibers can be seen in Table 3.1. The distance between the fibers and the measurement plane is h, the distance between the fibers is t and the indexes of refraction of the PMMA plate and the surrounding air are $n_{material}$ and n_{air} respectively.

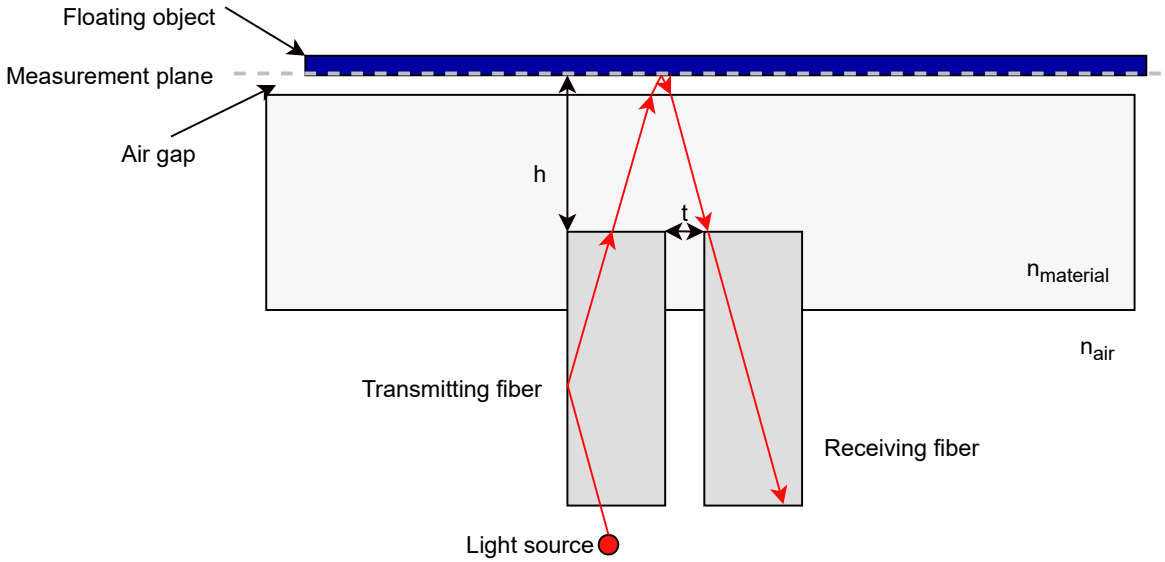

Figure 3.1: A visualization of the two-dimensional analytical model. In red, a possible light ray is drawn that is transmitted through the transmitting fiber, reflected by the floating object and received by the receiving fiber. The air gap is enlarged for visibility.

	Core	Cladding
Material	PMMA	Fluoropolymer
Diameter [mm]	0.98	0.01
Index of refraction	1.492	1.405

Table 3.1: Plastic optical fiber specifications [24]

3.2.1. Light spot size

The size of the light spot the transmitting fiber can create is dependant on the distance between the end of the fiber and the measurement plane h, the refractive index of the material after leaving the optical fiber $n_{material}$ and the shape of the material interfaces (lenses). A bigger spot size of the light coming out of the transmitting fiber would mean that a single optical fiber could cover a larger area to measure. This section will focus on the influence on the distance and the refractive indexes, lenses will be covered in the next section. The light spot is a two-dimensional circle on a surface. In this analytical model, the size of the light spot is calculated and shown by its diameter.

Influence of distance

The influence of the distance between the fiber end and the measurement plane can be easily calculated using the tangent function. The light coming out of the fiber will have a maximum angle, α_{max}, depending on the index of refraction of the material. The diameter of the light spot can then be calculated as follows:

$$\text{Spot size} = 2h \cdot \tan(\alpha_{max}) + \text{Diameter Fiber} \tag{3.1}$$

In equation 3.1, α_{max}, is dependant on the refractive index of the medium at the fiber exit. If that medium is PMMA, which is currently used in developed air bearings, then there is no material discontinuity since the core of the optical fiber is of the same material and thus there is no change of angle. The maximum angle follows from the numerical aperture of the optical fiber, as in equation 2.3, with the specifications from Table 3.1. In this situation, $\alpha_{max} = 30°$ with respect to the vertical, the same angle as the maximum propagation angle in the optical fiber. This gives a diameter of the light spot of $2.15mm$ if the distance between the fiber end and the measurement plane is $h = 1mm$. The greater this distance, the larger the size of the light spot; however, the light intensity will also be more spread out. In Fig. 3.2, the diameter of the light spot (yellow) can be seen for this situation. The light coming out of the transmitting fiber will all fall between the two maximal rays, seen in red.

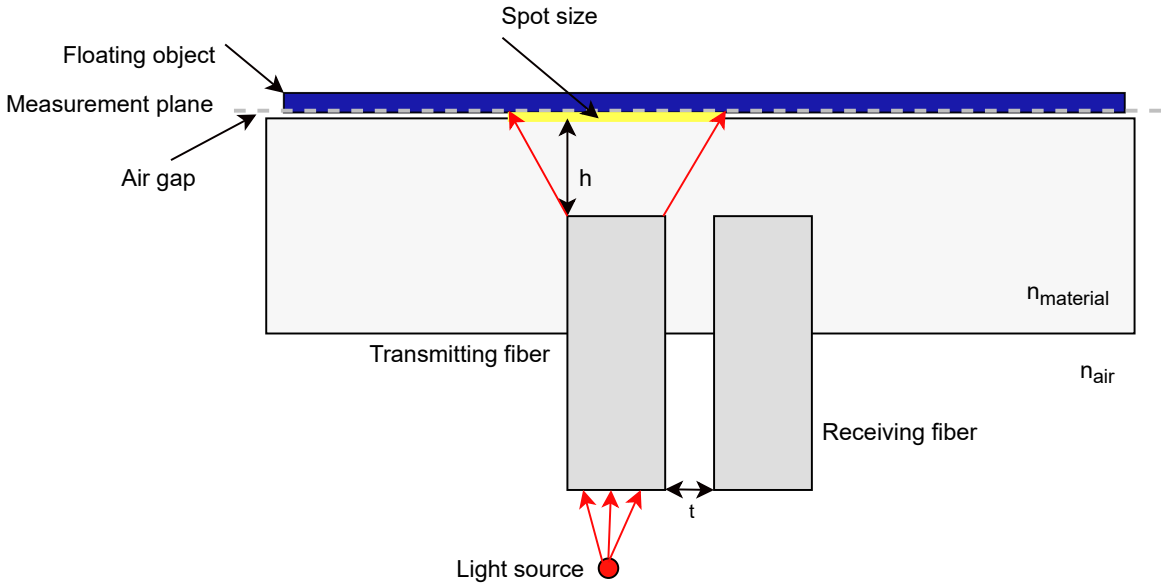

Figure 3.2: The analytical model with the diameter of the light spot (yellow) visualized. The red arrows coming out of the transmitting fiber indicate the maximum angles it can transmit.

Influence of refractive index

A medium with a lower refractive index compared to the refractive index of the PMMA of the fiber core would have a diverging impact on the rays. This would increase the size of the light spot at the measurement plane. Air (or vacuum) has the lowest refractive index of $n_{air} = 1$ and any material with a higher refractive index than PMMA would make the light spot smaller. Snell's law from equation 2.1 can be used to calculate the maximum output of the transmitting fiber in other media. Substituting equation 2.1 into equation 3.1, with media 1 being the optical fiber core:

$$\text{Spot size} = 2h \cdot \tan(\sin^{-1}(\frac{n_1}{n_2}\sin(\alpha_{max}))) + \text{Diameter Fiber} \tag{3.2}$$

The equation indicates that the lower the index of refraction of the other media, the larger the spot size will be. Purely air as the other media is not possible since the optical fibers will need to be placed in the air bearings. Setting the other media to air will give an indication of the maximum spot size achievable with the same distance $h = 1mm$. The angle of the light coming out of the fiber will then be 48°, resulting in a diameter of the light spot of $3.2mm$.

3.2.2. Transmittance

The amount of light that can be received by the receiving fiber is dependant on the overlap of the spot of both fibers and the angle of the rays in the overlapping area. The overlapping area can be approximated as follows, assuming the fiber is placed in a PMMA plate:

$$\text{Overlap} = 2h \cdot \tan(\alpha_{max}) - 2t \tag{3.3}$$

This approximation makes the assumption that the light spot is a line on a surface. It is however a circle on a surface and the overlapping area would be in the shape of an ellipse. Equation 3.3 thus calculates the semi-minor axis of the ellipse. The actual overlapping area would be less than what is calculated.

Light rays in the overlapping area must have an angle so that it travels to the receiving fiber. The further away from the receiving fiber, the higher the angle of a light ray has to be, to be captured by the receiving fiber. In the case that both fibers are half a millimetre from each other, $t = 0.5mm$ and the distance $h = 1mm$, the overlap percentage of the light spot of the transmitting fiber would be 7.2%, namely $0.15mm$ overlap of the total spot of $2.15mm$. This situation can be seen Fig. 3.3, where the spot size is indicated in yellow and an equal area indicated in green for the receiving fiber. The light blue lines at the top of the receiving fiber indicate the maximum ray angles that the fiber can accept. The overlap between the two areas is indicated in purple.

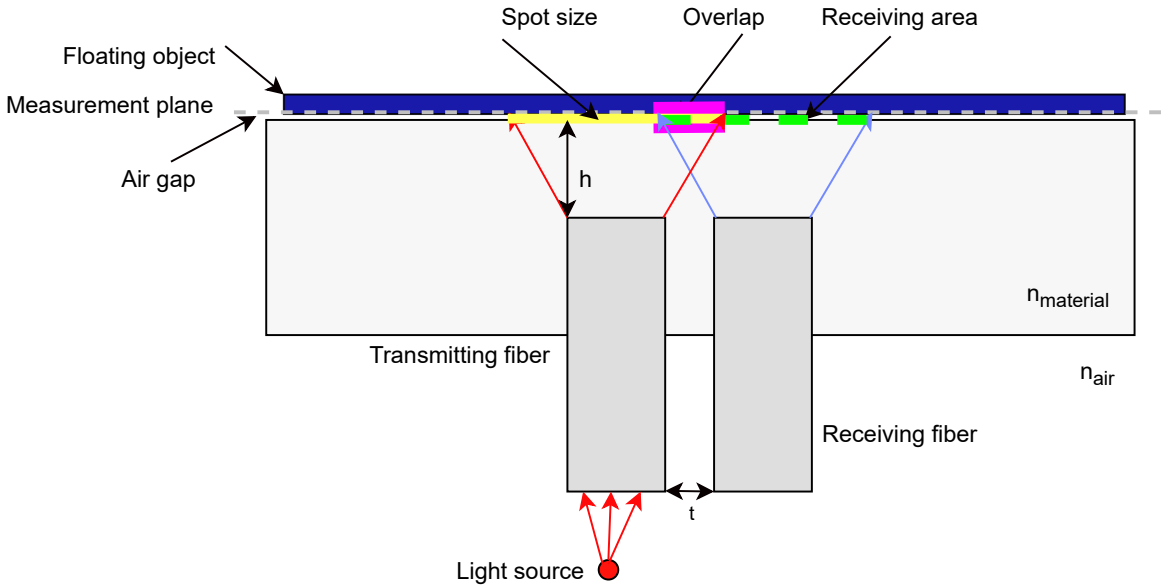

Figure 3.3: The analytical model with the spot size of the transmitting fiber (yellow), the cone of acceptance of the receiving fiber (green) and the overlap between them (purple) visualized. Light rays coming out of the transmitting fiber, hitting the overlapping area and have a correct angle can thus be received by the receiving fiber.

The amount of light rays in the overlapping area that will be received by the receiving fiber can be approximated to have a triangular distribution, with 0% of the light transmitted to the receiving fiber at the edges of the overlap and 50% of the light transmitted in the middle of the overlapping area (light ray angles 0° to 30°), with an average of transmission of 25%. Thus the maximum transmittance of the light coming out of the transmitting fiber into the receiving fiber is:

$$\begin{aligned} \text{Transmittance} &= \frac{\text{Overlap}}{\text{Spot size}} \cdot \text{Average fiber angle} \\ &= \frac{2\tan(\alpha_{max}) \cdot h - 2t}{2\tan(\alpha_{max}) \cdot h + \text{Diameter Fiber}} \cdot \text{Average ray angle} \end{aligned} \tag{3.4}$$

In the case of $h = 1mm$ and $t = 0.5mm$, the overlapping percentage is 53%, which would lead to a transmittance of 1.8%.

From the equation it can be seen that an increase in the distance h will lead to a higher transmittance and an increase of the overlap. There is however a limitation caused by the angles of the light rays. The more you increase the distance h for a bigger spot size and overlap, the fewer rays that will be captured by the receiving fiber. For a high distance h, and a small fiber to fiber distance t, only rays with a small angle with respect to the horizontal will be captured, as any ray with a larger angle will move past the fiber. Similarly, with a larger distance t, only rays with a larger angle will be captured and other rays lost.

To visualize the limitation caused by the angles of the light rays, the model as in Fig. 3.1 is changed. Instead of mirroring the light rays when the object is reached, the geometry is mirrored so that the light ray can be seen as a straight line. In Fig. 3.4a, the situation is shown where the overlap is smaller than the fiber diameter, with $h = 1mm$ and $t = 0.5mm$. It can be seen that the maximum ray coming out of the transmitting fiber of 30° will be captured by the receiving fiber. In Fig. 3.4b, only the distance h is increased to $h = 2mm$. The overlap increases, however light rays beyond the thickness of the optical fiber will not be received by the receiving fiber. A vision on the light source, broader than the actual diameter of the fiber is thus not possible with changing the distance h or changing the material with different indexes of refraction at the fiber ends.

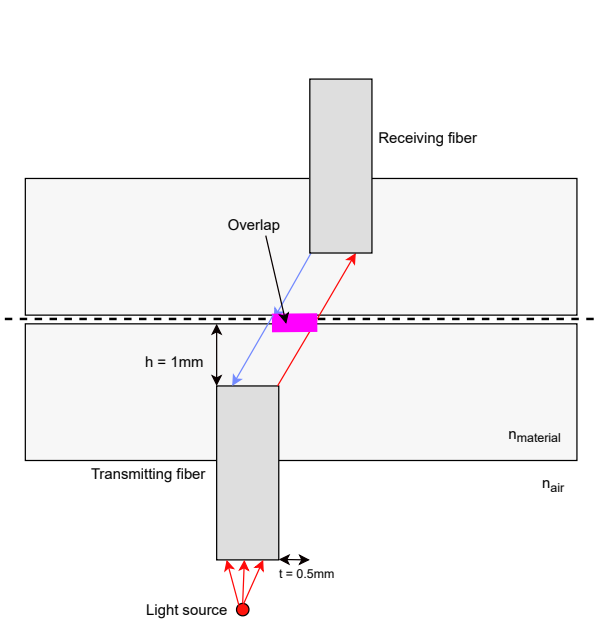

(a) Situation with $h = 1mm$ and $t = 0.5mm$. Light coming out of the transmitting fiber can be accepted by the receiving fiber, depending on the light ray angles.

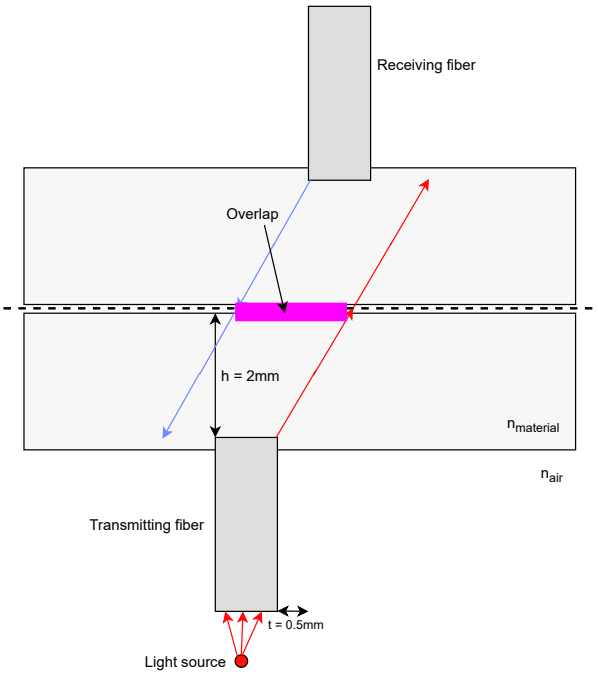

(b) Situation with $h = 2mm$ and $t = 0.5mm$. The light rays passing through the overlapping area, but beyond the diameter of the receiving fiber will move past the receiving fiber.

Figure 3.4: The analytic model from Fig. 3.1 is changed to show the limitations of the receivable spot area by the receiving fiber. The geometry next to the transmitting fiber is mirrored instead of mirroring the light rays at the measurement plane.

3.3. COMSOL simulation

The COMSOL model can be seen in Fig. 3.5. It is similar to the analytical model explained in section 3.2 and seen in Fig. 3.1, with a change in how the light source is modelled. The light source is modelled as a boundary condition on the bottom of the transmitting fiber, indicated in blue in Fig. 3.5. They are released from the boundary with angles within the allowed modes of the chosen optical fiber, namely between $-30°$ and $30°$ with respect to the vertical.

3.3.1. Light spot size

In the analytic model, the polarization state of the light was left out for simplicity and Snell's law is used at interfaces between two materials. A more complete model would take the polarization state of the light into account, resulting in secondary reflected and refracted rays, according to the Fresnel equations 3.5, 3.6, 3.7 and 3.8:

$$r_s = \frac{n_1 \cos\theta - n_2 \cos\phi}{n_2 \cos\theta + n_2 \cos\phi} \tag{3.5}$$

$$r_p = \frac{n_1 \cos\phi - n_2 \cos\theta}{n_1 \cos\phi + n_2 \cos\theta} \tag{3.6}$$

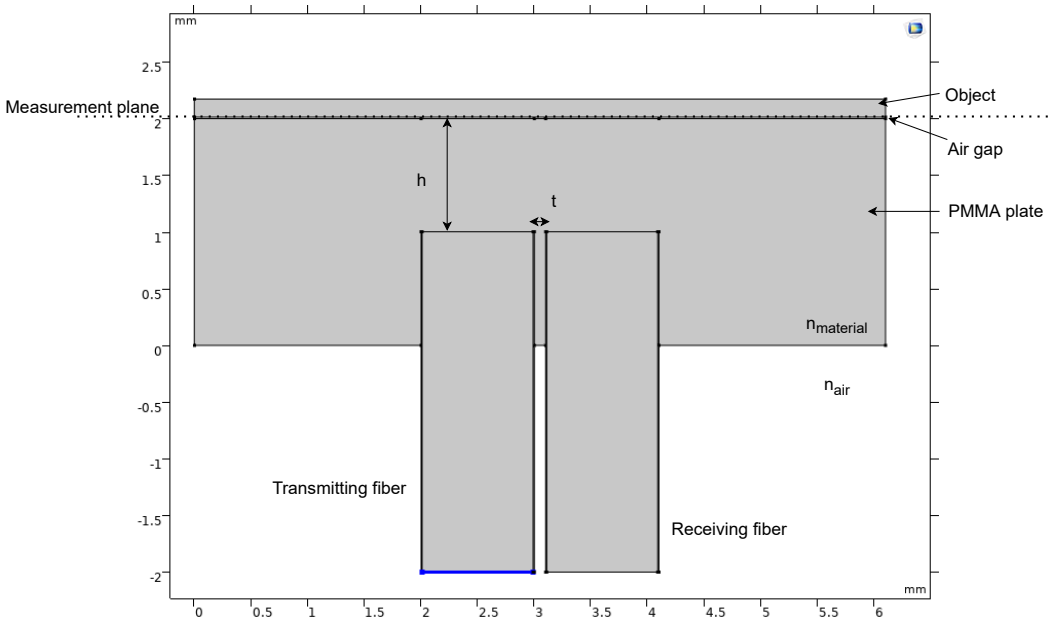

Figure 3.5: The model as used in the COMSOL simulations, with the starting point of the light rays at the blue line.

$$t_s = \frac{2n_1 \cos\theta}{n_1 \cos\theta + n_2 \cos\phi} \tag{3.7}$$

$$t_p = \frac{2n_1 \cos\theta}{n_1 \cos\phi + n_2 \cos\theta} \tag{3.8}$$

In these equations, r is the transmission coefficient and t is the transmission coefficient, with the subscript s for s-polarized light and subscript p for p-polarized light.

Without taking these secondary rays into account, the diameter of the produced light spot can be seen in Fig. 3.6. The material at the fiber end is the PMMA plate seen from Fig. 3.1. The distance $h = 1mm$ is kept the same as in the analytical approximation. At the point of ray release, the beam has been given a power of 1 W per unit thickness, $P_{start} = 1[W/m]$. 10 rays are released at 10 equally distributed points along the boundary for a total of 100 rays, giving an initial ray power of $0.01[W]$ per ray, as indicated in the colour bar on the graph. From the figure, it can also be seen that there is some leakage into the cladding of the optical fiber, which leaks out of the optical fiber when the surrounding material goes from air to PMMA. The diameter of the light spot including the leaked rays is roughly $3mm$; however, there are far fewer rays on the outer part of the spot. The diameter of the light spot without these leaked rays is around $1.6mm$.

Taking the secondary rays produced according to the Fresnel equations into account, the size of the produced light spot can be seen in Fig. 3.7. It can be seen that the secondary rays are at least one order lower in power, compared to the originally released rays. The secondary rays are produced at nearly every material discontinuity. For visibility purposes, a maximum of 100 secondary rays is produced. The spot size including the secondary rays is much larger; however, the seen intensity at the measurement plane is much lower.

The influence of the refractive index has been simulated by setting the index of refraction of the exiting material $n_{material}$ to $n = 1$. The result can be seen in Fig. 3.8, without secondary rays. The maximum angles of the light are larger as expected, but the diameter of the light spot is again slightly smaller compared to the analytical model with a total of $1.9mm$.

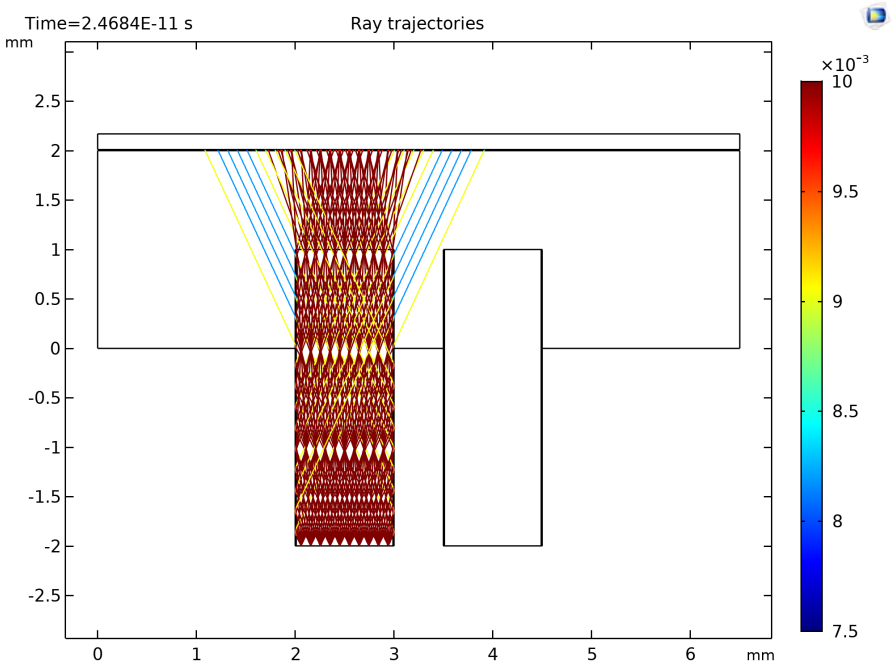

Figure 3.6: Size of the light spot with without secondary rays. Each light ray has an initial power of $0.01[W]$, as indicated by the colour bar. Light rays that are not fully internally reflected lose some of their initial power at each reflection, this can be seen by the light blue and yellow colours of the light rays.

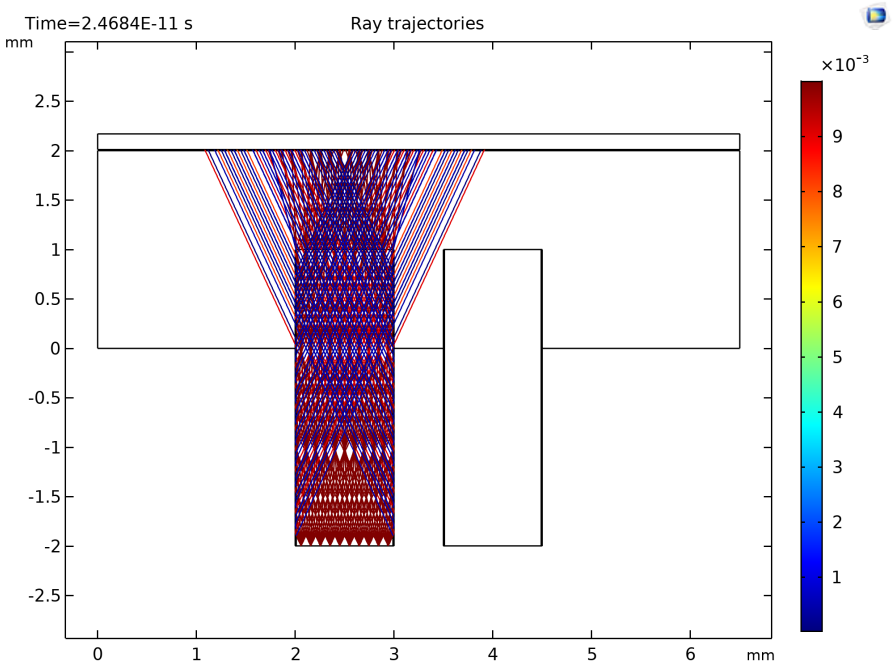

Figure 3.7: Size of the light spot taking the secondary rays produced according to the Fresnel equations into account. The secondary rays have significantly reduced power, as indicated by their colour.

3.3.2. Transmittance

In the COMSOL simulation for the transmittance, the settings are set the same as in section 3.2.2, with the distances set equal as for the analytical approximation of the transmittance, namely $h = 1mm$ and $t = 0.5mm$. The COMSOL model makes the same approximation as the analytical model in that the overlap is simulated as a line segment. A more complete model 3D model would simulate the overlap of the two circles as en ellipse.

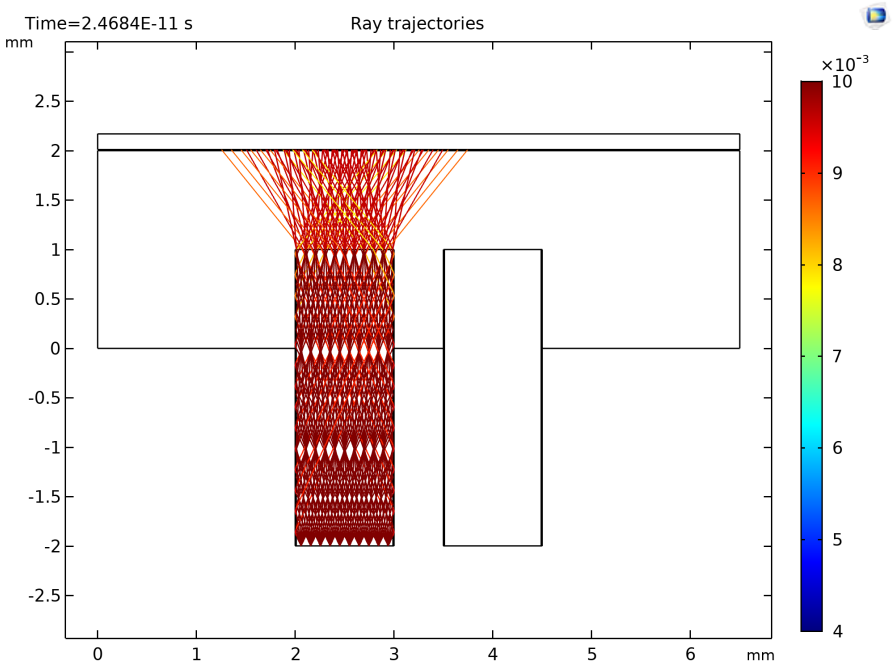

Figure 3.8: Size of the light spot without secondary rays, exiting the fiber in air.

In the result of the COMSOL simulation in Fig. 3.9, it can be seen that most of the light rays are not captured by the receiving fiber. In this figure, the secondary rays have been turned off for visibility and rays that will not end up at the end of the receiving fiber are stopped at boundaries.

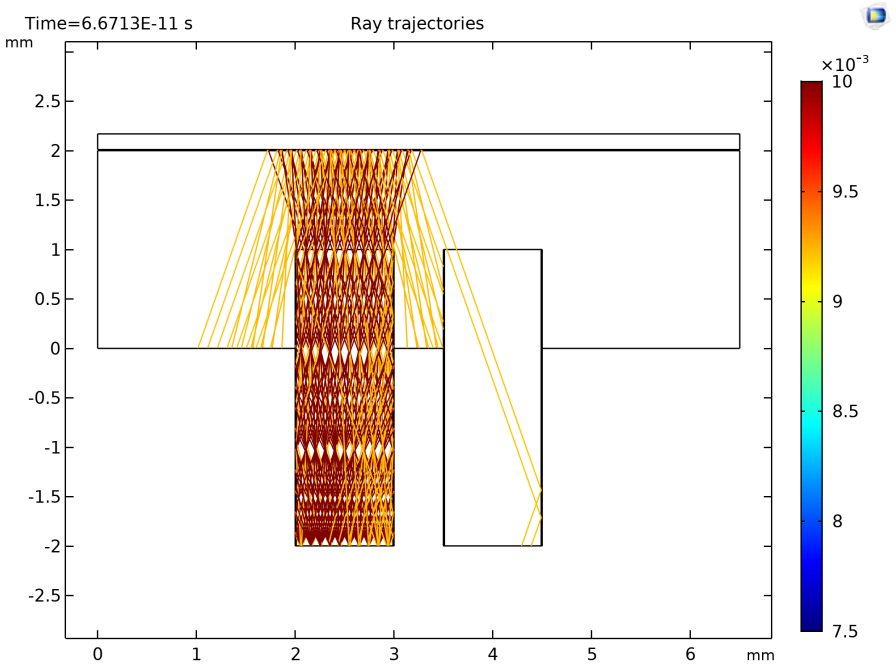

Figure 3.9: Reflectance into the receiving fiber, without secondary rays. 2 light rays out of a 100 are captured, resulting in a transmittance of 2%.

The transmittance can be seen in Fig. 3.10, wherein Fig. 3.10a, the secondary rays have been turned off and in Fig. 3.10b, the secondary rays are added. It can be seen that there is only a small increase in transmit-

tance when secondary rays are taken into account, namely from 1.83% to 2.03%.

The limitation of transmittance caused by the angles of the light rays can also be visualised with COMSOL. The geometry is again mirrored at the position of the measurement plane. In Fig. 3.11a, it can be seen that only light rays with a specific angle, dependant on the distance t between the two fibers, can be received by the receiving fiber, even though the lost light rays are in the overlapping area of both fibers.

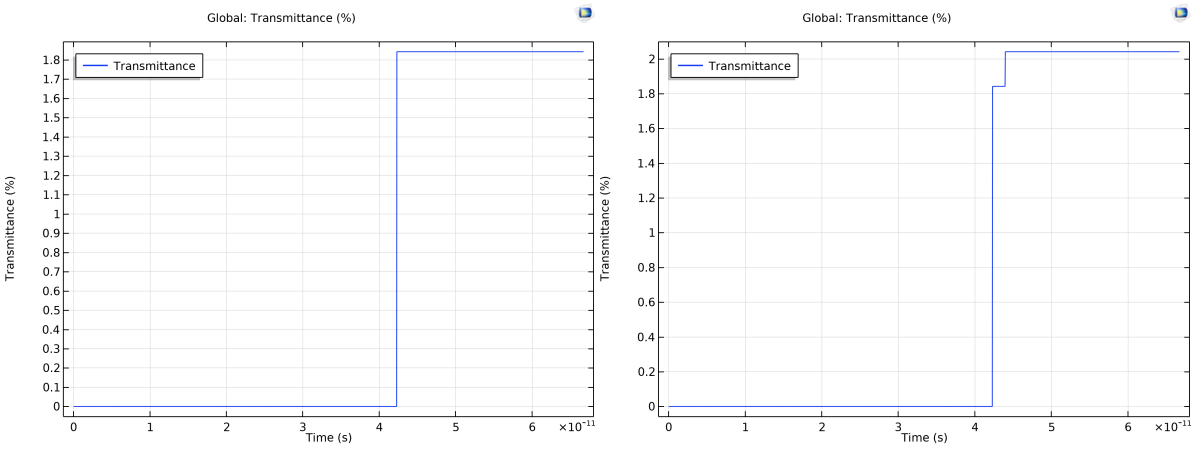

(a) Transmittance into the receiving fiber, without secondary rays.

(b) Transmittance into the receiving fiber, with secondary rays.

Figure 3.10: Transmittance of the transmitting fiber into the receiving fiber.

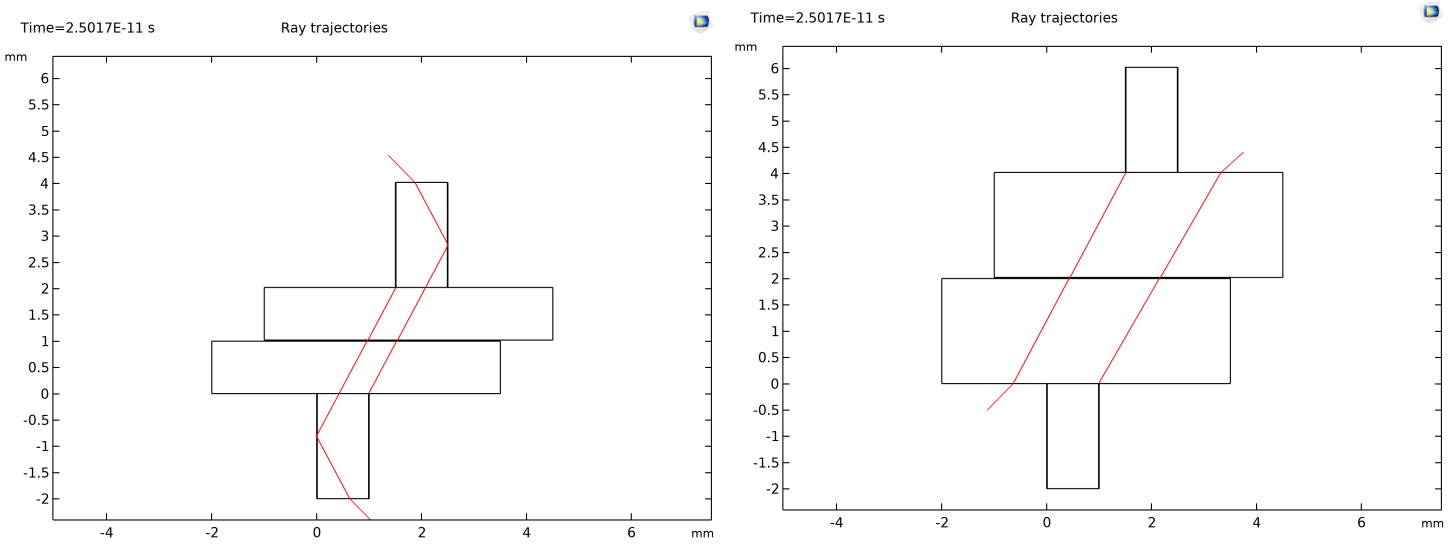

(a) Situation with $h = 1mm$ and $t = 0.5mm$. The light ray coming out of the transmitting fiber, with the maximum angle of 30 degrees is captured by the receiving fiber.

(b) Situation with $h = 2mm$ and $t = 0.5mm$. The light ray coming out of the transmitting fiber, with the maximum angle of 30 degrees and moving through the overlapping are is not captured by the receiving fiber.

Figure 3.11: Results of the altered model with the geometry instead of the light rays mirrored at the measurement plane.

3.4. Analysis of a lens

In the previous sections, it was concluded that the size of the light spot of the optical fiber can be increased, even without the use of lenses. However, when the light is transmitted from a source to the receiving fiber, the vision of the receiving fiber is always limited to its own diameter. This is because the light rays outside the fiber diameter will simply go past the optical fiber, as was shown in Fig. 3.4.

The placement of a lens would be a problem since a flat surface is required on the top surface of the air

bearing, a lens would not be suited there. Since the optical fibers will be pushed in a flat plate, for example in a PMMA plate, limited space is available to create a lens directly on the optical fibers. Some rays that would go past the optical fiber without a lens, might be directed into the optical fiber, however other rays will be rejected that would go into the optical fiber without the lens. In Fig. 3.12, a possible lens is shown. Two rays are drawn, one ray that is directed into the fiber due to the lens and another ray that is rejected due to the lens. The actual vision of the optical fiber will still be limited by its diameter and the diameter of the lens.

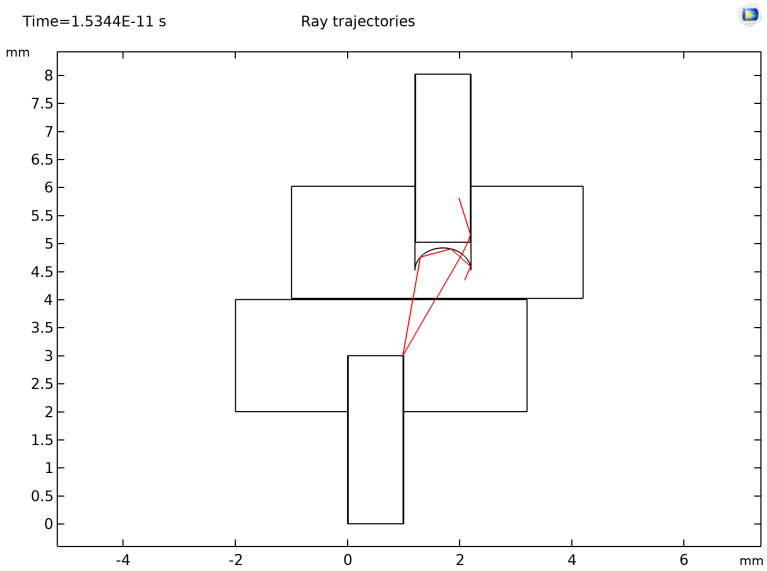

Figure 3.12: In the mirrored model, half a ball lens is created just before the tip of the receiving fiber. Between the lens shape and the receiving fiber is an air gap. Two light rays are simulated, showing that a lens can both capture rays otherwise missed, but can also reject rays otherwise received by the transmitting fiber.

3.5. Analysis of diffusers

To counter the problem of the vision of the optical fiber being limited to its diameter, diffusers can be used. Surface diffusers are not suited for an air bearing where a flat surface is required. Volumetric diffusers, as explained in section 2.3.2, diffuse the light inside the volume of the diffuser. This means that the light coming out of the diffuser could have any random angle, at all positions along its length. The intensity of the light will drop down the further it is from the light source. A diffuser avoids the problem that the light rays coming from the light source will move past the optical fiber. This is because the light source is spread out across the diffuser surface, virtually creating an infinite amount of light sources. If the diffuser would be placed on top of the optical fibers, the diffusing effect would be doubled: namely when the light goes from the transmitting fiber to the measurement surface and when the light gets reflected by the moving object back into the diffuser.

Simulating a volumetric diffuser would be difficult and complicated due to the very small, large amount of nanoparticles. Designing the most optimal diffuser for this problem is out of the scope of this thesis, thus various types of diffusers will be experimentally tested.

3.6. Conclusion

In this chapter, an analytical model and a simulation model was made to find how the vision of an optical fiber can be increased and how the transmission from a light source into an optical fiber can be increased. A model was made with a transmitting fiber and a receiving fiber, where the transmitting fiber acts as the light source in the measurement plane and the receiving fiber acts as the receiver of the light reflected by the floating object. Both the analytical model and the COMSOL simulation showed that the light spot can be increased by changing various parameters. The transmittance could also be increased; however, the vision of the receiving fiber towards the light source is limited by the receiving fiber diameter. Lenses for the receiving fiber will not break away from this limitation. Light diffusers randomize the light ray angles and thus avoid the limitation that a direct view of the light source is needed.

4

Experimental setup 1: Top side vision

In this chapter, the design and the results of the first setup are discussed. This setup will focus on testing various diffusers and comparing the size of the light spot received with a light spot without a diffuser. The cutting of the plastic optical fibers is discussed and the camera type and the different exposure settings are explained. Lastly, the light spots with and without a diffuser are measured in their size in pixels and average pixel intensity.

4.1. Requirements and wishes

At the time of designing this setup, the COVID-19 coronavirus outbreak was declared a pandemic and the first "intelligent" lockdown in the Netherlands was in effect. This has some influence on the design of the experimental setup, mostly that the experiments should be suitable to do at home. This gives the requirement that the setup should be compact, portable and adjustable. A consequence of this is that this thesis will only look at one building block of the complete measurement system: one set of receiving fiber(s) with one transmitting fiber. Next to this, there are some wishes:

- An environment completely sealed from ambient light
- The camera should write the pictures directly to a laptop for analysis
- The camera settings should be adjustable through the computer
- Re-use the materials and devices of the last bachelor group
- The diffusers should be easy to cut
- The setup should be cost-efficient

4.2. Design overview

In this section the design of the first setup will be shown, taking the requirements and wishes into account. In this setup the camera is placed above the transmitting fiber, looking down onto the light spot. This setup will not yet look into the transmittance into the receiving fiber, but only the size of the light spot the transmitting fiber can create. In Fig. 4.1 the complete setup can be seen. It is designed with two possible uses in mind. The setup shown in Fig. 4.1a is designed to test multiple diffusers placed on the PMMA plate containing the transmitting fiber (in red). The setup shown in Fig. 4.1b is designed to visualize the light spot without any diffusers. Two metal strips with a thickness of $20\mu m$ replicate the double thickness of the air layer and a PMMA plate (green) is placed on the strips with two brackets (in purple) to push the green PMMA plate downwards with the weight of the camera.

The realised setup can be seen in Fig. 4.2a with the two variations of the inside shown in Fig. 4.2b and 4.2c. All the PMMA plates are laser-cut and the other objects are 3D-printed. To counter reflections of the light, the printed parts are spray-painted with a matt black finish. The optical fiber is placed in an $8mm$ thick clear PMMA plate with one end pointed towards the camera and the other end placed closely above the LED. This creates a cheap and easy LED to fiber coupler. The LEDs themselves are standard red 12V LED strips, cut to the desired size, leftover by the last bachelor group. The camera holder is placed over the other objects and seals the light coming out of the transmitting fiber from the ambient light, avoiding the need for filtering

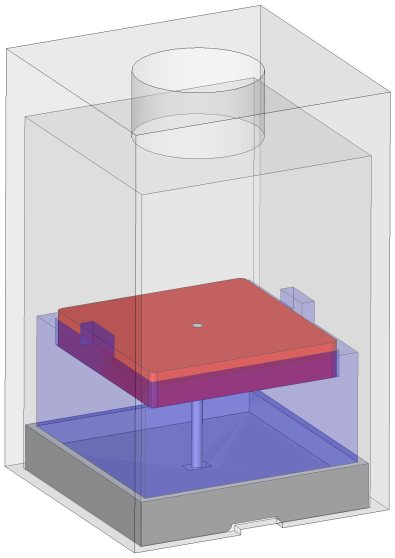

(a) SolidWorks model of the setup, without any diffuser placed on top. The blue part is made transparent to make the optical fiber visual.

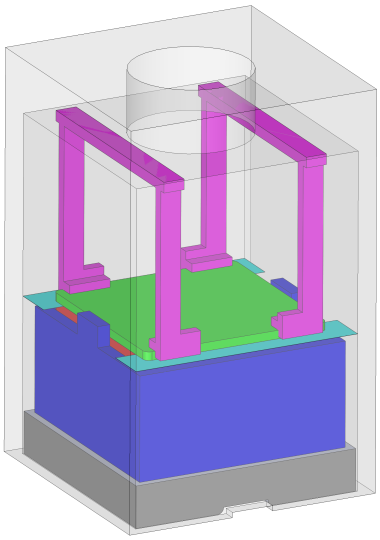

(b) SolidWorks model of the setup, with the spacers and the scratched PMMA plate and brackets.

Figure 4.1: SolidWorks model of the setup, the holder for the camera is the outer transparent object. The red object is the PMMA plate with the optical fiber pressed into it. The blue part is the holder for the PMMA plates. The grey object at the bottom holds the LED. The green part is a PMMA plate used to visualize the light spot without a diffuser, the light blue stripes are the thin 20μm metal stripes and the purple brackets pushes the green plate towards the red plate.

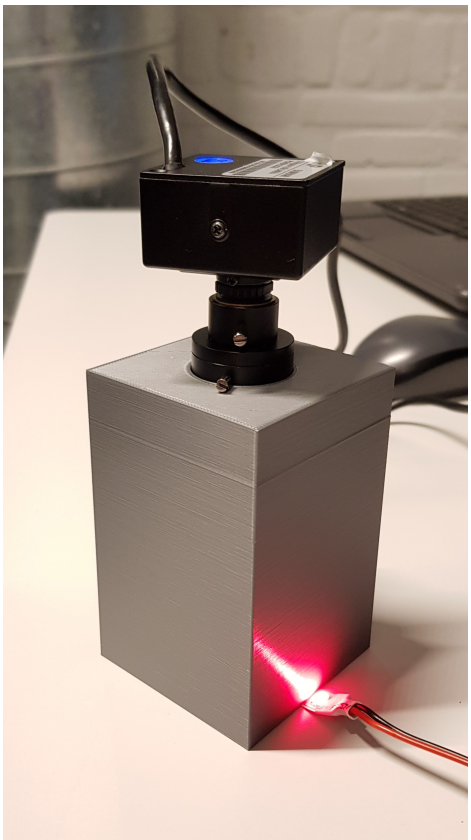

(a) The first setup with the camera mount completely isolating the measurement area from the ambient light.

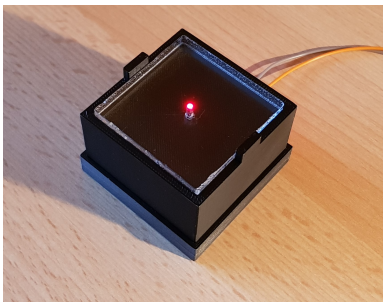

(b) The 3D-printed block, containing the PMMA plate with the transmitting fiber, placed in a holder for the LED.

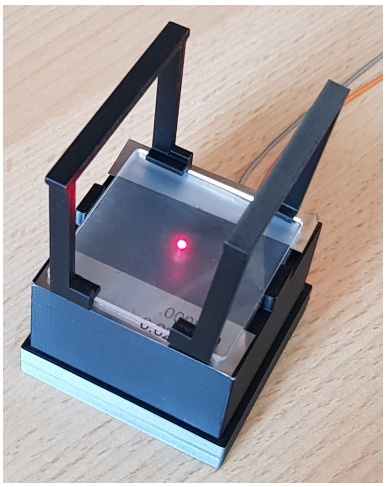

(c) The same 3D-printed block as in figure (b) above, with the 20μm spacers and an extra PMMA plate placed on top.

Figure 4.2: The realised first setup, showing the camera viewing the light spot from the top.

the ambient light. The camera holder is also used as a weight to push the top PMMA plate down with the brackets, as shown in Fig. 4.1b and 4.2c, to create a defined $20\mu m$ layer between the end of the optical fiber and a one-sided finely scratched PMMA plate. In the following subsections, some details of the setup will be discussed more thoroughly.

4.2.1. Optical fiber choice and handling

As mentioned in section 2.1.2, plastic optical fibers will be used for their ease of use and low cost. The last bachelor group had a few meters left of a plastic optical fiber cable. The fiber has a $980\mu m$ core of PMMA with a $10\mu m$ cladding of fluoropolymer resulting in a diameter of $1mm$. The cable is protected by a $0.6mm$ thick layer of polyethylene, brining the total diameter of the plastic optical fiber to $2.2mm$. The used optical fiber can be seen in Fig. 4.3.

Figure 4.3: The used plastic optical fiber, with the protective layer [24].

Fiber handling

It was found that when the protective was removed, the exposed optical fiber could be scratched and damaged easily, leading to leakage of the light. To prevent leakage of the light, the protective layer was left on the fibers. A benefit of leaving the outer sheath on was that it could be used to press the fibers in position in the PMMA plates.

Fiber cutting

Plastic optical fibers can be cut on the spot with a sharp razor blade, cutting pliers, or specialized tools. Cutting them with simple tools does however not give the best results. A sharp razor blade gives a smoother result compared to cutting pliers; however, the cut is still somewhat rough, as seen in Fig. 4.4a, which could lead to coupling losses in the input and intensity differences in the output due to the non-uniform shape. Tools specialized for crimping and cutting plastic optical fibers are available, however at extremely high costs. A complete set of tools would cost around $700 and only the finishing tool around $325 [9], which is deemed too much.

A way to produce a smooth finish on the plastic optical cable was to cut it as smooth as possible with a sharp razor blade, followed by grinding the end of the fiber on very fine grinding paper under some water. The fiber ends can be inspected by directly looking at fiber ends with the camera, completely isolated from the ambient light, as seen in Fig. 4.4c. The result of grinding the fiber ends with 2000 grit sandpaper can be seen in Fig. 4.4b. The fine scratches do not give a polished result; however, the light does come out uniformly.

(a) Plastic optical fiber cut with a razor blade.

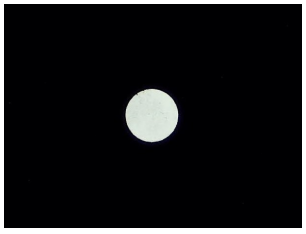

(b) Plastic optical fiber, ground with 2000 grit sandpaper after cutting with a razor blade.

(c) Optical fiber inspection setup.

Figure 4.4: Process of finishing the ends of the plastic optical fibers.

4.2.2. Diffuser types

Simulating the effects of a diffuser proved to be too difficult and time-consuming, thus various types of diffusers will be experimentally tested. The diffusers are bought at PyraSied Xtreme Acrylic, a company focused on acrylics and also light diffusers for the lighting industry. The light diffusers are classified based on their light transmission, diffusion and efficiency.

The retailer of the diffusers defines the light transmission as the amount of light that is measured at the other side of the diffuser then where the source of light is. There are always some losses due to reflections inside the diffuser and at the material interfaces of the diffuser.

The diffusers that the retailer sells are aimed at the lighting industry. The most important use of the diffusers is to cancel individual LED-dots from a LED-strip so that the surface at the other side of the diffuser looks uniformly lit. The diffusivity is defined as the distance needed between the LED-strip and the diffuser to get a uniform light distribution. A diffusivity of 90% means that if the individual LEDs are placed $9cm$ apart, the distance between the LED-strip and the diffuser needs to be $\frac{9cm}{90\%} = 10cm$.

Lastly, the efficiency of the diffusers is defined as their light transmission multiplied by their diffusivity. The full documentation on the diffusers sold by this particular retailer can be found on their website [35].

Several diffusers were chosen with high efficiency: both good light transmission as well as good transmission. A limitation was set on their thickness of $2mm$. The chosen diffusers can be seen Table 4.1.

Diffuser type	Light transmission	Diffusivity	Efficiency	Thickness [mm]
PRIMO® XT N381	71%	56%	40%	2
PyraLed® YT275	81%	67%	54%	1.8
PyraLed® YT575	71%	68%	48%	1.5

Table 4.1: Several diffusers from PyraSied Xtreme Acrylic [34]

Several surface diffusers were also bought. Their surface textures were however too large to be suitable for an air bearing.

In Fig. 4.5, a diffuser can be seen that is placed on top of the transmitting fiber from Fig. 4.2b. All, except YT575 (polystyrene), of the bought diffusers were made from acrylic (PMMA). This means they could be cut to shape using the laser cutter available at the TU Delft.

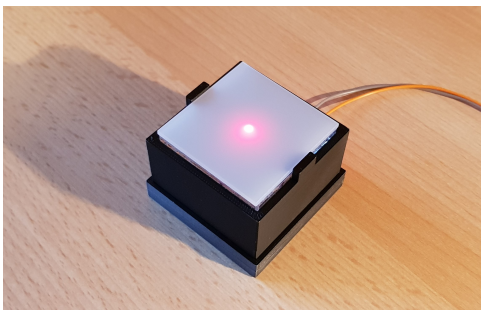

Figure 4.5: The N381 diffuser placed on top of the transmitting fiber.

4.2.3. Camera

The wish for the camera was that it should write pictures directly to a laptop for analysis and that the settings of the camera could be controlled from the laptop. This leaves two options:

1. A regular (DSLR/mirrorless) camera connected to the laptop using specialized software to directly write to the laptop

2. An USB webcam

A regular camera might provide higher quality images; however, they are much larger than USB webcams and require a workaround with software to write directly to a laptop using for instance MATLAB. USB webcams are usually lower in picture quality but are very easy to be used with MATLAB. MATLAB can be programmed to take a snapshot with filenames specified in the code.

The last bachelor group bought a USB webcam for this similar reason. Their choice was an ELP-USBFHD01M-BFV, which will also be used in this thesis, it can be seen in Fig. 4.2a. It captures images in maximally 1080p resolution, although at low frames per second. The frames per second of the webcam are not important for the use in this thesis, since only single-frame images will be taken. Due to the small size of the camera, it can be easily integrated into the setup.

The ELP-USBFHD01M-BFV webcam came with a varifocal 2.8mm to 12mm lens. This allows for a short distance between object and image sensor and thus a compact setup, due to the wide view of the lens. A downside of this wide view lens is the image distortion it causes. In this first setup, the distortion is not important and ignored, but will be addressed in the next chapter.

4.3. Received images

The received pictures and the achieved size of the light spot highly depend on the exposure setting of the camera. The camera adjusts its exposure setting by altering the framerate. At high exposure settings, the framerate is thus lower than with lower exposure settings. Every exposure setting for the three different diffusers can be seen in Fig. 4.6, 4.7 and 4.8 and without a diffuser, directly looking into the transmitting fiber in Fig. 4.9. The highest exposure setting is clearly overexposed since the centre of the spot is at the maximum pixel intensity value of 255 in all channels (red, green, blue). At lower exposures, the light spot is barely visible and thus underexposed.

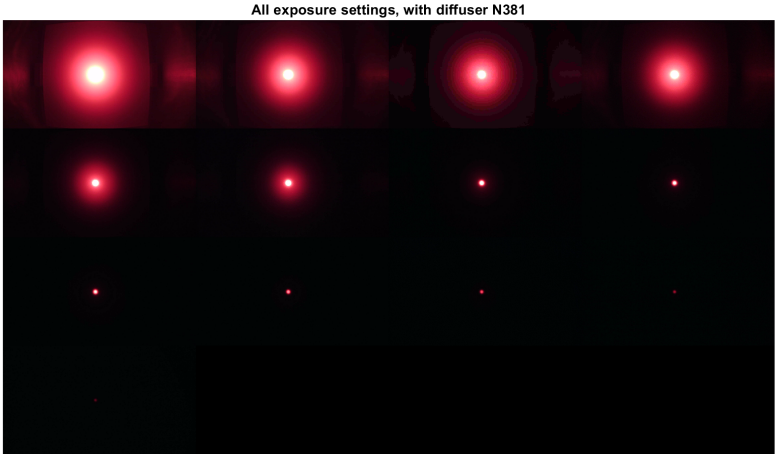

Figure 4.6: 13 images of the spot size of diffuser N381, with all possible exposure settings. The highest exposure is the top left image, counting down from left to right and from top to bottom.

4.3.1. Blooming

To find the correct exposures, a metal strip blocking the light is placed partly over the light spot. The metal strip should be completely dark, as the light coming out of the diffuser beneath it is reflected downwards. The pixel intensity values are tracked along a horizontal line and the intensity values should thus drop down to zero when the metal strip is reached. In Fig. 4.10 for exposure setting -1 and diffuser N381, it can be seen that the pixels values are not completely at zero when the metal strip is reached. When the exposure is set to below -5, as seen in Fig. 4.10b for exposure -5, the intensity values drop to around zero; however, some noise can be seen. It can also be seen that there is some blooming effect at the centre of the light spot. This also occurs at even lower exposure settings, this is however unavoidable since this setup looks directly into the light source. To avoid both over and underexposure, every picture is taken in both exposures setting -5 and -6.

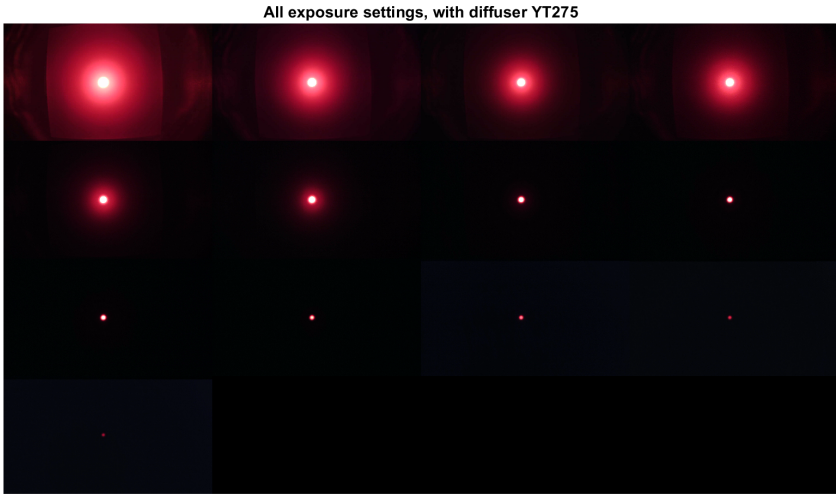

Figure 4.7: 13 images of the spot size of diffuser YT275, with all possible exposure settings. The highest exposure is the top left image, counting down from left to right and from top to bottom.

Figure 4.8: 13 images of the spot size of diffuser YT575, with all possible exposure settings. The highest exposure is the top left image, counting down from left to right and from top to bottom.

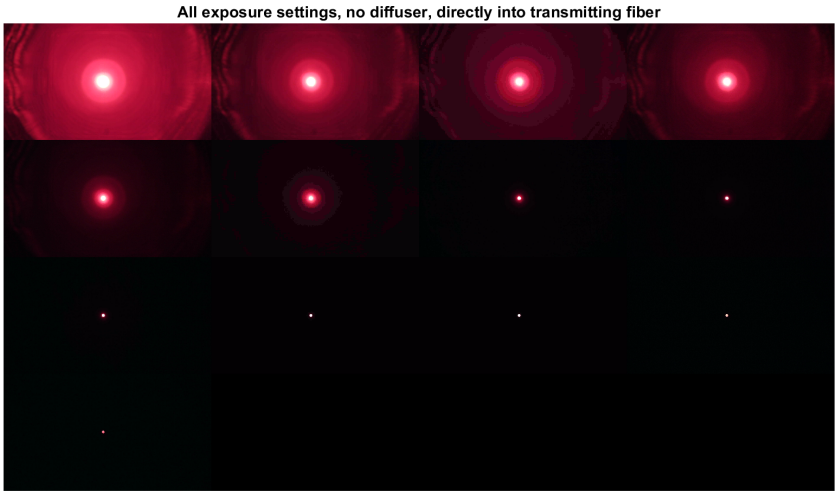

Figure 4.9: 13 images of the spot size directly looking into the transmitting fiber, without a diffuser, with all possible exposure settings. The highest exposure is the top left image, counting down from left to right and from top to bottom.

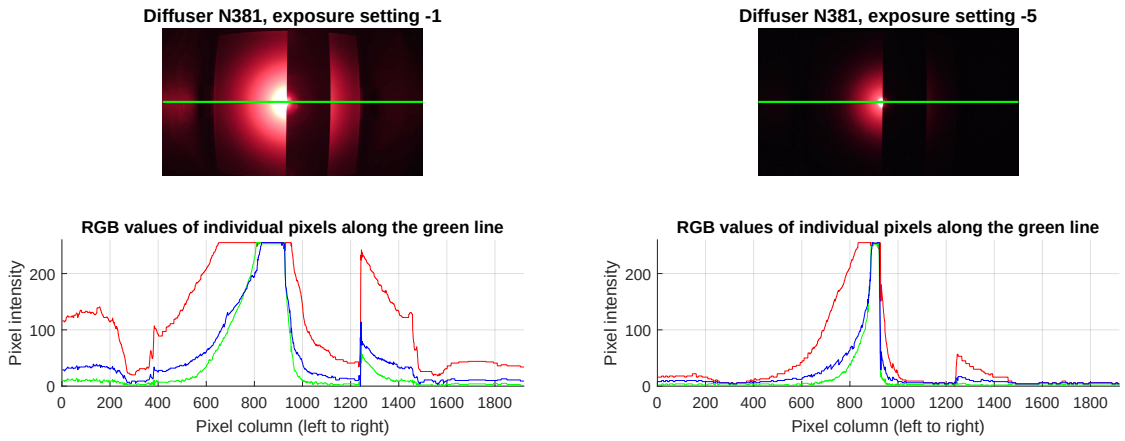

(a) Intensity values for camera exposure setting -1.

(b) Intensity values for camera exposure setting -5.

Figure 4.10: Partly blocked light spot with diffuser N381. The pixel intensity values are tracked along the green line and shown for all colour channels: red, green and blue.

4.3.2. Camera noise

In the previous section, shown in Fig. 4.10, some noise was found on the pixel intensities. The noise is investigated by taking images with the camera lens fully blocked off. In Fig. 4.11, two different pictures can be seen. The noise is different in both images and varies in intensity and noise type. Sometimes the noise is varying, like in Fig. 4.11a and other times it is constant, like in Fig. 4.11b. Since the noise can not be predicted, no steps are taken to control it.

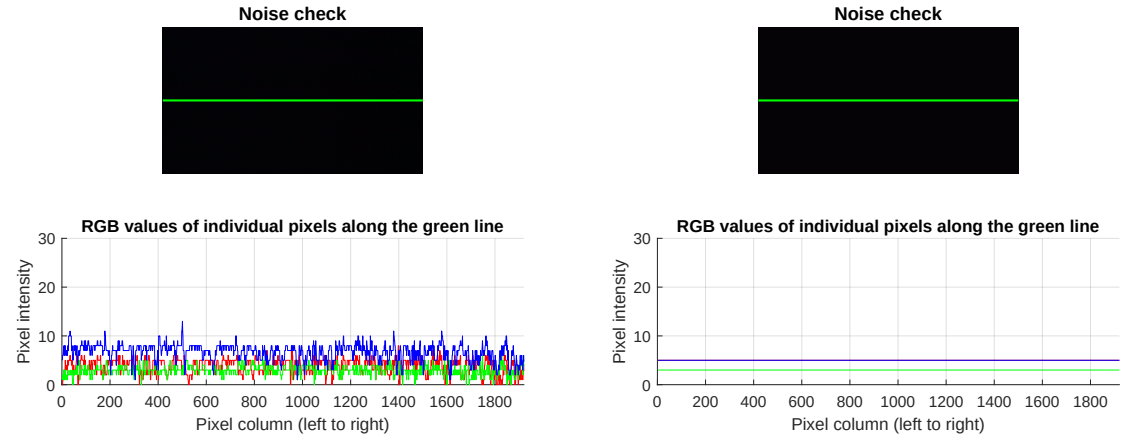

(a) White noise like signal, at a completely black image.

(b) Constant noise, at a completely black image.

Figure 4.11: Different types of received noise on the images, with the camera lens completely blocked. The shown pixel intensities are tracked along the horizontal green line.

Another effect caused by the camera is random bad pictures. When this occurs, it looks like the intensity of the image jumps from one level to another, while it should be a fluent transition. Every picture taken on the exposure setting -3 will give this results and it is not known why or when this happens for other exposure settings. In Fig. 4.12a, such a bad picture can be seen, next to a normal and good quality picture in Fig. 4.12b.

4.3.3. Light spot measurements

To compare the received size of each light spot caused by the different diffusers, an intensity threshold is set. A threshold can only be set for one colour channel or the average of all channels and since red is the dominant colour due to the LED light being red, the threshold is set for the red channel. In Fig. 4.13, the spot sizes can be seen for the three tested diffusers with the threshold set to 50 out of 255. In Table 4.2, the results can be

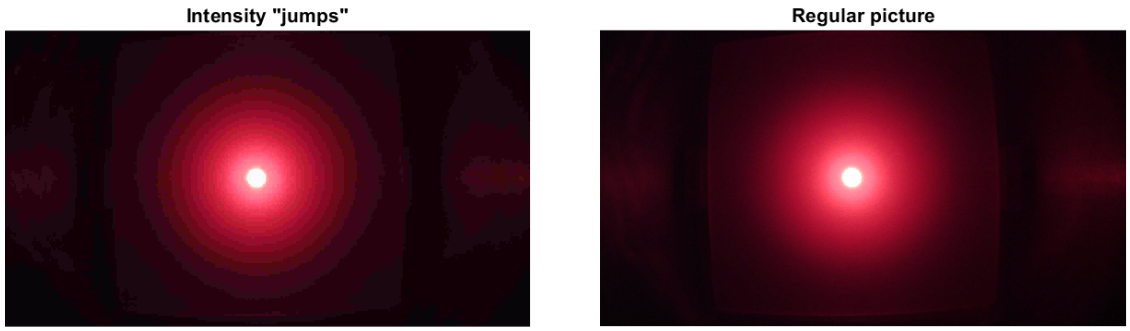

(a) Image with intensity jumps

(b) Image with fluent intensity change

Figure 4.12: An example of a picture with intensity jumps and one without.

seen for both exposure setting -5 and -6.

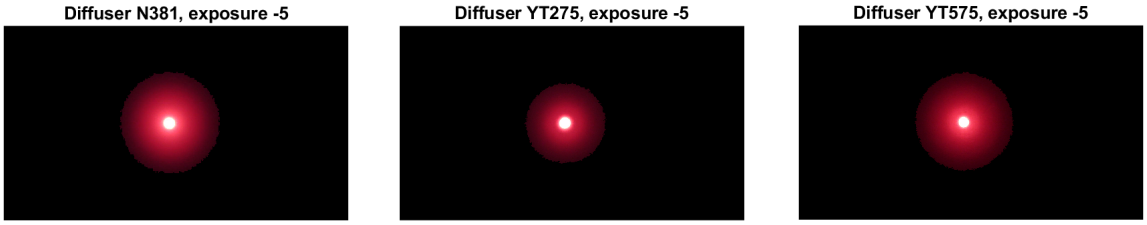

(a) Spot for diffuser N381

(b) Spot for diffuser YT275

(c) Spot for diffuser YT575

Figure 4.13: Images of the light spot, with a threshold set at intensity level 50 out of 255.

	Exposure -5		Exposure -6	
Diffuser type	Spot size [pixels]	Average intensity	Spot size [pixels]	Average intensity
PRIMO® XT N381	241690	125	155752	117
PyraLed® YT275	154022	109	82166	104
PyraLed® YT575	228996	115	135122	107

Table 4.2: Spot size in pixels and average pixel intensity level for both exposure setting -5 and -6 with the threshold set at 50 out of 255.

From the results, it can be observed that the N381 diffuser has both the highest light transmission as well as the highest diffusivity. According to the data of the retailer, as was given in Table 4.1, the YT575 diffuser should have both a higher transmission and diffusivity. The difference in results could be caused by the way the measurement was done. The retailer defines the diffusivity as the distance needed to diffuse a range of separate light sources (LED-strip) to a uniform lit surface, as was explained in section 4.2.2. In this thesis, the diffusers are placed directly on top of the light source (the transmitting fiber) and the diffusivity is measured as the area of the created light spot.

4.3.4. Spot size without a diffuser

To get an indication of how much the diffusers have increased the vision of the optical fibers, the spot size without a diffuser is also measured. The setup shown in Fig. 4.2c and 4.1b with the $20\mu m$ spacers is used. However, since the light is not diffused, the centre of the spot is even brighter than without a diffuser, causing more blooming and requiring a lower exposure setting of the camera. The same method as in section 4.3.1 is used by covering half of the light spot. At exposure setting -7, the covered part was almost at zero intensity and thus this exposure setting is used to calculate the size of the light spot without a diffuser. In Fig. 4.14a, the effect of the covered section is barely visible due to the small size of the light spot.

In Fig. 4.14b, the full light spot can be seen without a diffuser. The threshold is again set at intensity level 50 out of 255. The light spot is significantly smaller than with any of the diffusers. In table 4.3, the size of the light spot in pixels and average pixel intensity can be seen. The same method as in section 4.3.3 is used. From the results is can be seen that diffusers caused an increase in the spot size of almost 2 orders in magnitude.

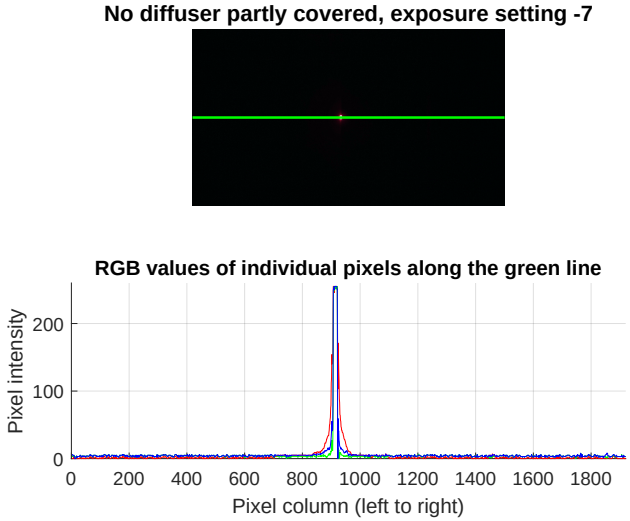

(a) Spot size without a diffuser, covered halfway to determine correct exposure setting.

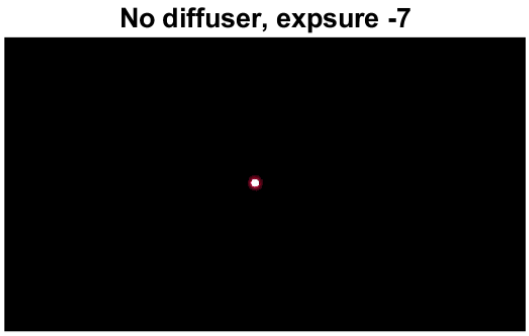

(b) Full light spot without a diffuser, with an intensity threshold set to 50 out of 255.

Figure 4.14

Diffuser type	Spot size [pixels]	Average intensity
No diffuser	2581	136

Table 4.3: Several diffusers from PyraSied Xtreme Acrylic [34]

4.4. Conclusion

In this chapter, the first experimental setup is designed for testing various types of diffusers. It is a simple setup where a camera looks from a short distance downwards directly to the light spot. A method is found to get a smooth cut of the plastic optical fibers by grinding the fiber ends after cutting with 2000 grit sandpaper. Several types of diffusers are tested; however, looking directly into the light source gave some issues since significant blooming of the light source occurred. An exposure setting with minimal blooming, but also not underexposed, is found by blocking a part of the light spot with an opaque object. With the camera exposure set to either -5 or -6, the spot size of the diffusers in pixels is between 82000 and 240000, with the diffuser PRIMO® XT N381 being the most diffuse. Therefore, this diffuser type has been used in the remainder of the research. Comparing the spot size of this diffuser to a spot size without a diffuser of 2581 pixels, a significant increase is achieved.

5

Experimental setup 2: Fiber to fiber transmission

In this chapter, a new setup is designed and its results are discussed. This setup will look into the light transmission of the transmitting fiber into the receiving fiber, using a diffuser placed above the fiber ends. First, the updates on this new setup are discussed and a motion system, with a reference object, is designed. Factors leading to possible inaccuracies in the setup are discussed and the distortion of the images is corrected. Lastly, the accuracy of the motion system is measured and the settings for both cameras are given.

5.1. Design updates

In this section, the design of the updated experimental setup investigating the receiving fiber will be shown. The requirements and wishes as given in section 4.1 are still valid. In this setup only the most diffusing diffuser, the PRIMO® XT N381 type diffuser, will be used. Some results might vary with the other diffusers; however, the principle will remain the same. The same optical fibers as from the previous setup will also be used and the objects are sprayed with matt black paint to limit reflections. The three main differences of this updated setup compared to the setup as shown in Chapter 4 are the following:

1. The updated setup will not look directly into the light source to avoid blooming.
2. A motion system is added to simulate the movement of a rectangular object in the measurement plane. The object will reflect light back to the diffuser, creating a region of more intensity along with its motion.
3. The received signal by the receiving fiber is investigated.

A consequence of point 1 is that the placement of the camera will need to be changed. Instead of looking with the camera from the top down onto the light spot, the camera will be placed below the light spot, looking upwards. The design for the part looking at the created light spot can be seen in Fig. 5.1a. The optical fibers can go through the green camera holder to the PMMA plate (blue). The fibers are bend doing this, but the bending radius is below the maximum allowable bending radius of $10mm$ of the used plastic optical fibers [24]. The transmitting and receiving fibers are now directly placed in the vision of the camera, this does partly obstruct the vision of the camera on the light spot. An object can be moved over the measurement plane with two parts sealing the light spot from the ambient light. In Fig. 5.1b, the object coupling the receiving fibers to a second camera is shown. The receiving fibers will guide the received light from in the measurement plane to its other end, where it can be read out by the second camera. In Fig. 5.1c, the LED to fiber coupler can be seen. The same LEDs from the previous setup in chapter 4 are used.

The realised setup can be seen in Fig. 5.2a. In the figure each part is labelled. Since the camera looking at the light spot is placed looking upwards, the USB-cable has to come out of the bottom of the camera holder. If the cable of the camera would come out at an angle, due to the rigidity of the cable, the camera would also be at that angle. Thus, the setup will need to be placed at the edge of a table with the USB-cable hanging freely. A clamp is used to ensure that the setup does not fall over. In Fig. 5.2b, the placement of the diffuser can be seen, with the slider containing the moving object above it. In Fig. 5.2c the setup is closed from ambient light with the light covers in place. In the following subsections, the motion system, the second camera and the receiving fiber placement will be discussed in more detail.

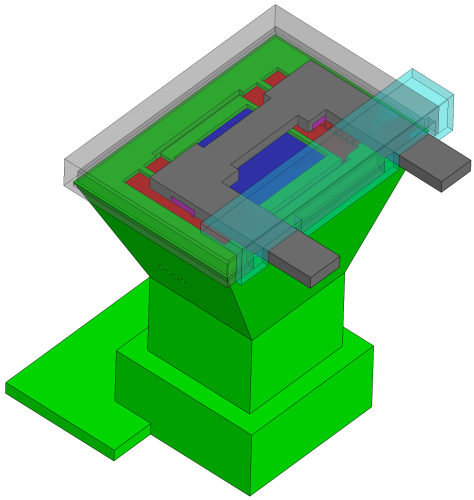

(a) The measurement block for the light spot. The green part is hollow from the inside, with the camera placed in it looking upwards towards the light spot. The PMMA plate (blue) is placed on a ledge inside the hollow section of the green part. The optical fibers are guided through the green part to the PMMA plate. The red and purple parts are for the motion system and fixed to the green stationary part and the grey slider respectively. The transparent parts are the covers to seal the light spot from the ambient light.

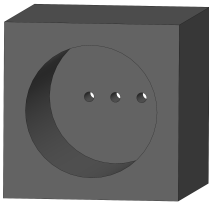

(b) The readout block where one end of the receiving fibers are placed. A second camera looking at the fiber ends will seal the fiber ends from the ambient light.

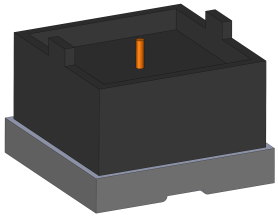

(c) The LED to fiber coupler. The same block from the first setup (Fig. 4.2b) is used, with a small segment of the transmitting fiber shown in orange.

Figure 5.1: SolidWorks models of the updated setup, showing the measurement block for the light spot (a), the block for the receiving fibers (b) and the LED to fiber coupler (c).

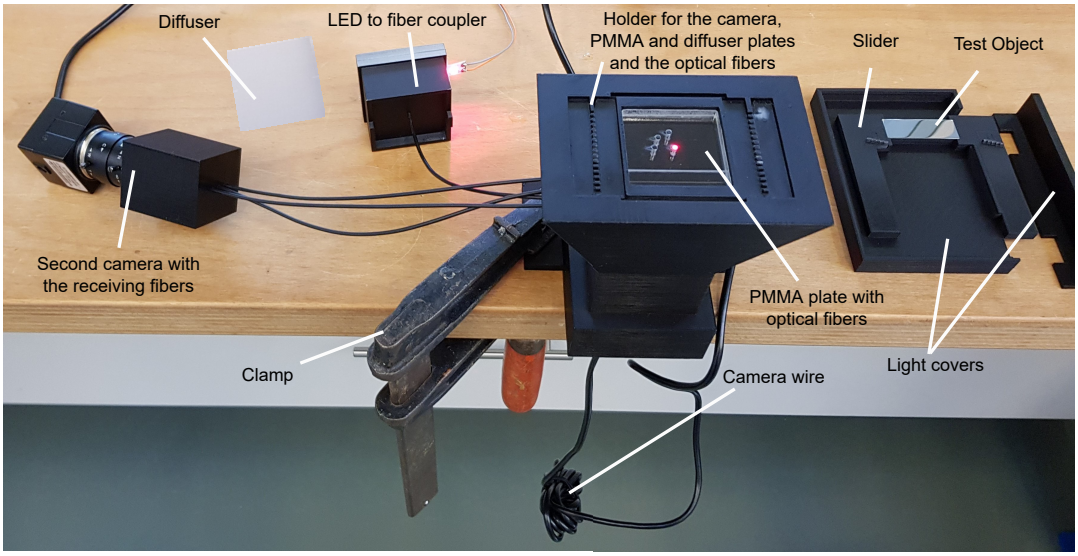

(a) The realised updated setup, with each part of the setup labelled in the figure.

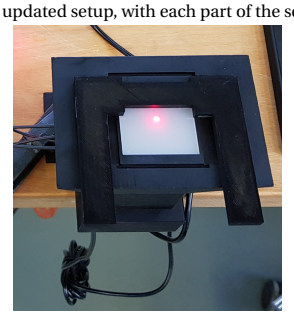

(b) The diffuser is placed on top of the PMMA plate containing the transmitting and receiving fibers. The moving object is placed over the diffuser.

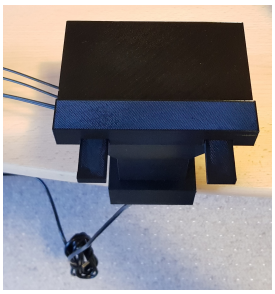

(c) The light covers in place, completely sealing the light coming out of the transmitting fiber from the ambient light.

Figure 5.2: The realised updated setup, with the camera looking looking from below the light source upwards.

5.1.1. Receiving fiber placement and symmetry

The receiving fibers and the transmitting fiber will need to be placed in the PMMA plate shown in blue in Fig. 5.1a, obstructing the vision of the camera on the light spot. This is not a problem, since the light spot is fully circular symmetric. However, for the to be designed motion system, a clear vision of the moving object is needed. The sensor should be able to detect an object coming from any angle; however, simulating a motion from every direction would be very cumbersome.

Instead of simulating every angle of motion, the receiving fiber will be placed at different angles around the transmitting fiber. Multiple receiving fibers can be placed in the same PMMA plate, thus allowing for multiple measurement points. In Fig. 5.3a the base position of the receiving fiber can be seen. The transmitting fiber is in the centre of the created light spot and the receiving fiber is direct to the right of the transmitting fiber. This base position of the receiving fiber is the 0-degree angle of motion of the object.

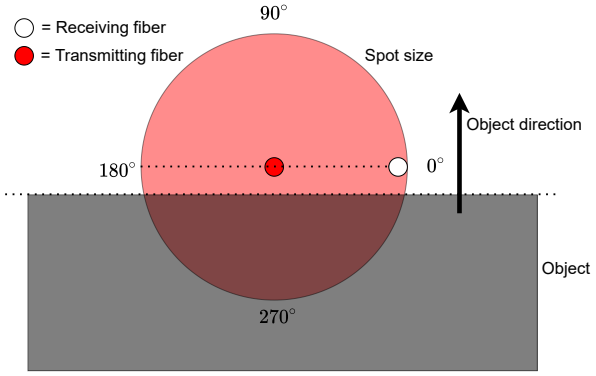

(a) The base position of the measurement fiber, with the object moving from bottom to top.

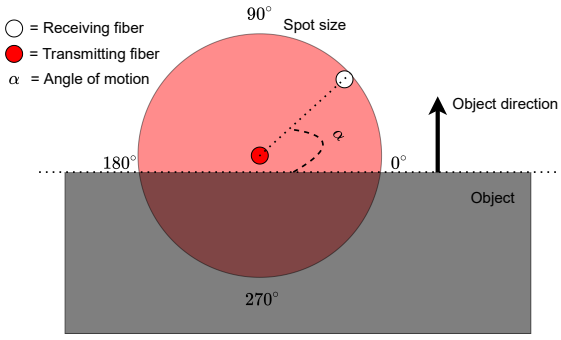

(b) The measurement fiber is now rotated around the transmitting fiber, with the object still moving from the bottom to the top.

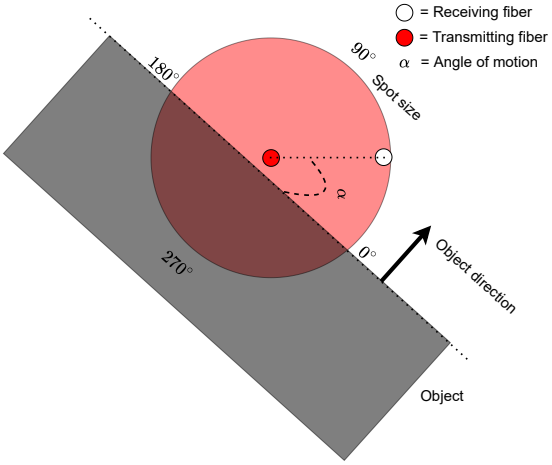

(c) Rotating the entire figure (b) so that the receiving fiber is back at its base position. The angle of motion of the object is now changed with respect to figure (a).

Figure 5.3: Schematics to show that only one angle of motion is needed. The transmitting fiber is the bright red dot at the centre of the larger red dot. The object is the black rectangle, made transparent for visibility of the light spot. The movement direction of the object is along the black arrow and the receiving fiber is the white dot at the edge of the light spot. The angle of motion is the angle between the edge of the object and the line from the transmitting to the receiving fiber.

The position of the receiving fiber is now rotated around the transmitting fiber. In Fig. 5.3b, it can be seen that there is an angle between the edge of the object and the line from the receiving fiber to the transmitting fiber. The motion of the object remains the same, namely from the bottom to the top. If the entire Fig. 5.3b

is rotated so that the receiving fiber is back at its base position, the object will also rotate. In Fig. 5.3c the result can be seen, showing that a rotation of the receiving fiber around the transmitting fiber is equivalent to a different angle of motion of the moving object. The zero degrees angle of motion is thus when the object is moving from the bottom to the top and the 180-degree angle of motion is when the object is moving from the top to the bottom.

From Fig. 5.3a, symmetry in the received signal of the receiving fiber for various angles of motion can be predicted. Four lines of symmetry can be defined: at 0, 90, 180 and 270 degrees. Any placement of the receiving fiber along the angles 0 to 90 degrees will give the same signal as placement of the receiving fiber along the angles 180 to 90 degrees, with the line of symmetry at 90 degrees as the axis of the mirror. In the top half of the circular spot, from 0 to 180 degrees, the transmitting fiber will always be passed first before the receiving fiber, while in the bottom half, angles 180 to 360 degrees, the receiving fiber will be passed first before the transmitting fiber by the moving object. Exceptions are the angles 0 and 180 degrees, at these angles both the transmitting and receiving fiber are passed at the same time by the moving object. This means that the signal received by the receiving fiber from the angles 0 to 180 for a full motion will be the reversed of the signal from 180 to 360 degrees.

To conclude, all angle of motions of the object can be predicted when only one-quarter of all angles, for instance from 180 to 90 degrees, is known. It is thus sufficient to simulate only one angle of motion with multiple receiving fibers rotated around the transmitting fiber.

5.1.2. Point of measurement

It is important to have a constant point for determining the position of the object for every angle of motion. It can be hypothesised that two types of transition can be observed: when the transmitting fiber gets covered by the object and when the receiving fiber gets covered by the object. Placing the point of measurement with equal distance between the receiving and transmitting fiber, the zero point of the object edge will always be in the middle of these two transitions. In Fig. 5.4, the position of three measurement points can be seen for three receiving fibers placed at different angles.

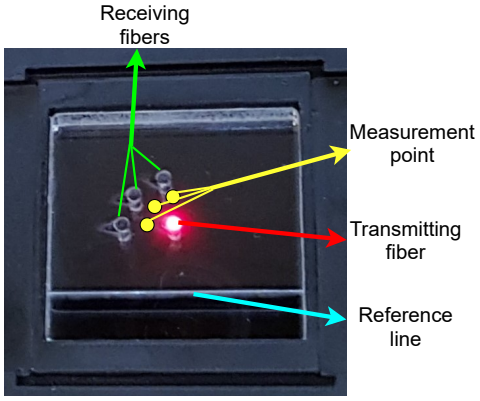

Figure 5.4: The PMMA plate holding the transmitting and receiving fibers. The yellow measurement points are not physically on the plate, but indicate the point of measurement for different angular positions of the receiving fibers. The use of the reference line will be explained in section 5.2.4 and it is engraved into the plate.

The placement of the receiving fibers, and thus the points of measurement, is dependant on the transmittance into the fibers. The optimal distance between the transmitting and receiving fiber will be calculated in section 6.3.1.

5.1.3. Replicating moving object

In order to simulate the motion of an object across the measurement plane as seen in Fig. 3.1, a motion system is designed. To keep the system compact, portable and adjustable, a motion stage with a defined path and error is not possible. Servo or stepper motors combined with an Arduino board would be possible but would make the system more complicated and less suitable for experiments at home. It is thus decided to

design a manual and step-wise discrete motion system.

The steps will need to be at well-defined positions and repeatable. To achieve this, an indexing type motion system is designed. The motion system will be printed with a 3D printer and limitations regarding the smallest feature size will limit the step size that can be obtained. The available 3D printers were an Original Prusa i3 MK3S extruder and an Original Prusa SL1 resin printer.

It was first tried to print the entire camera holder (Fig. 5.1a in green) including the motion system from one piece using the extruder printer. The tolerance of the extruder printer is around $0.3mm$ and the minimum feature size is limited to the nozzle diameter of $0.4mm$. A motion step of $3mm$ was achieved without breaking the protruding parts. This step size was considered too large; however, a smaller step is not possible with the extruder printer, since the protruding parts would become too fragile.

The SL1 resin printer is more accurate and precise than the MK3S extruder printer with a minimum layer thickness of $0.01mm$, it can however only print smaller objects. The protruding parts are of a sawtooth/trapezoid shape, with the base being wider than the top. Any tolerance between the two parts will be minimized when the fingers will be pressed together, as seen in Fig. 5.5a from the side and in Fig. 5.5b from the bottom. It can be seen that it is a two-step motion system, with the main step (main index) of $3mm$ (the red part) and the secondary step (subindex) of $0.6mm$ (grey part). The effective step size is thus $0.6mm$ over a motion range dependant on the number of main steps.

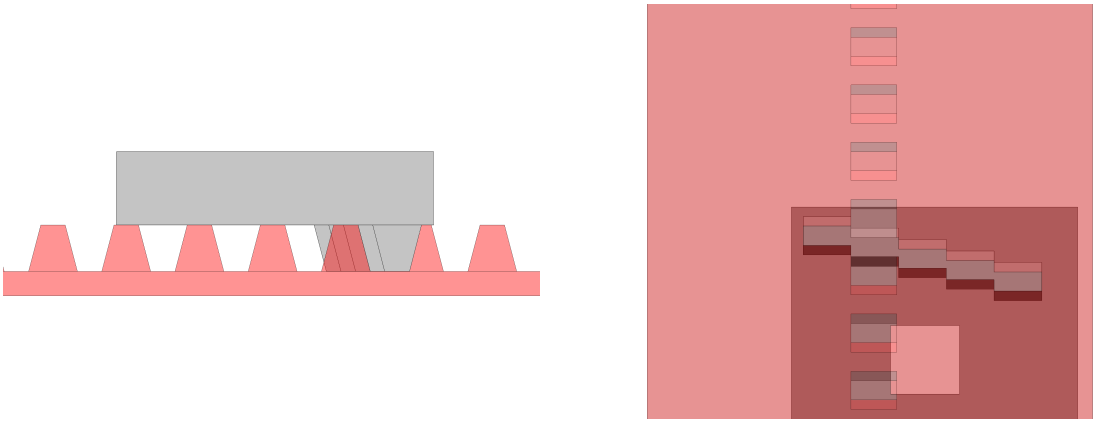

(a) Side view of the design of the discrete motion system.

(b) Bottom view of the design of the discrete motion system.

Figure 5.5: The discrete motion system, the red part holds the main steps, and the grey part holds the secondary steps (subindex) which moves slightly sideways and $0.6mm$ forwards or backwards.

The realised motion system can be seen in Fig. 5.6. The motion system consists of two parts, a part that can be seen as the ground and a part that is pressed into the moving slider. The ground part can be seen in Fig. 5.6a and holds the main steps. It is a thin layer pressed into the camera holder. The secondary steps are pressed into the moving slider as seen in Fig. 5.6b. With each secondary step, the slider also moves slightly sideways.

5.1.4. Reference object

In the slider, as shown in Fig. 5.6b, a reference object needs to placed. For this small setup, a full-size silicon wafer or solar cell is not suitable. A silicon wafer is highly reflective, like a mirror, while a solar cell might be less reflective. A solar cell can look blue, meaning that it will absorb some of the visible spectra of the light. A different colour LED, or any other light source, could be used to still achieve a reflection of the light.

Two extreme situations will be simulated: a fully reflective object, spreading the light in a specific direction and a fully diffuse object, spreading the light in any direction. For the reflective object, a metal piece is polished to a mirror finish, it can be seen in Fig. 5.7a. A glass mirror would have also been possible; however, this introduces an extra material interface, namely the glass layer, and the extra thickness of the glass. For the diffuse object, a metal piece is coated with white paint and can be seen in Fig. 5.7b. The reference object will

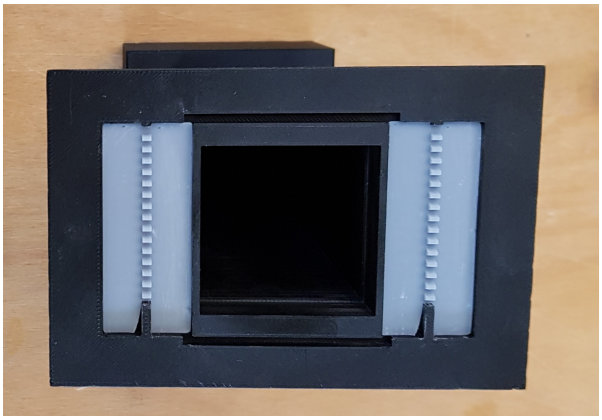

(a) The main steps of the discrete motion system. There are 14 main steps, each step main step is a $3mm$ movement.

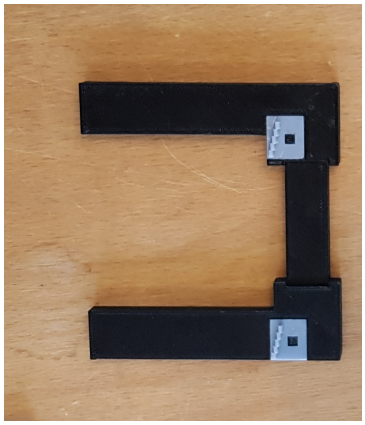

(b) The secondary steps, placed in the slider and holder of the reference object. The secondary steps divide the main steps into 5 steps, $0.6mm$ each.

Figure 5.6: The realised two step discrete motion system.

be rectangular to resemble a solar cell.

(a) The fully reflecting reference object, a metal piece polished to a mirror finish. The object is placed inside the slider.

(b) The diffuser object, a metal piece with a layer of white paint.

Figure 5.7: The two reference objects.

The metal piece is in both situations a $15.05mm$ by $45mm$ rectangle. The width of $15.05mm$ is slightly larger than the width of the slider from Fig. 5.6b of $14.90mm$. This ensures that the edges of the reference object are seen by the camera instead of the edges of the slider.

For the reflective object, the metal piece had to be polished. The edges of the metal piece are important, as the final sensor system should be able to detect the edges. Polishing sharp edges on a flat object proved to be difficult.

5.1.5. Second camera

In the previous setup from Chapter 4, only one camera was needed, facing the light spot. In this setup, next to the light spot, the transmission into the receiving fibers is also measured. In order to compare the vision of the camera looking at the light spot and the light transmission, two cameras are needed. The wishes for the new camera remain the same as explained in section 4.2.3 and since the ELP-USBFHD01M-BFV webcam worked well, the newer version of this webcam is bought.

The bought camera is the ELP-USB8MP02G-SFV with again a varifocal 2.8 to 12mm lens for close up pictures. This newer camera supports a higher resolution of up to 3264 by 2448 pixels, 4 times higher than the older webcam at a lower cost. The camera can be seen in Fig. 5.2a in the left side of the image.

5.2. Measurement uncertainties

In the previous setup in sections 4.3.1 and 4.3.2, it was found that there is some noise in the received pictures. This noise will lead to measurement uncertainties in finding the position of the reference object through the

camera. There are however also other factors that could influence the accuracy of the measurements. These factors are discussed in this section.

5.2.1. 3D print tolerance

The entire experimental setup is made out of 3D printed parts. An Original Prusa i3 MK3S extruder printer is used to print all object except the motion system as discussed in section 5.1.3. The tolerance of this printer is around $0.3mm$ in all directions. It is important to ensure that both of the cameras' positions are fixed, as well as the position of the PMMA plate holding the optical fibers. The 3D printed objects are designed with a small tolerance so that the cameras and the PMMA plate always fits. With layers of tape around the cameras and the PMMA plate, a tight fitting is created to minimize unwanted movement.

5.2.2. Camera distortion and off-centre

The wide view lens of the webcams allows for a short distance between the cameras and the object and thus for a compact setup. The downside is that a wide view lens will distort the images so that straight lines will look bent. For tracking the motion of the moving object it is important that the edge of the object is straight and not deformed. Since the distance between the camera sensor and the moving object is constant, the distortion can be calculated using chequerboard patterns at the object distance. With the distortion known, the images can be corrected for that distortion. This is only important for the camera directly looking at the light spot and the moving object. The second camera looking at the ends of the receiving fibers does not need to be corrected, since the fiber ends are at constant positions and only the intensity of those dots are of importance.

A MATLAB application, called camera Calibrator, is used to calculate this distortion. In Fig. 5.8a, the chequerboard pattern can be seen before being corrected for distortion. It can be seen that the PMMA plate holding the optical fiber is curved, as is the chequerboard pattern. The application recognizes the pattern and corrects the curvature. The result of the correction can be seen in Fig. 5.8b. The pattern is straight and the edges of the PMMA plates are no longer curved.

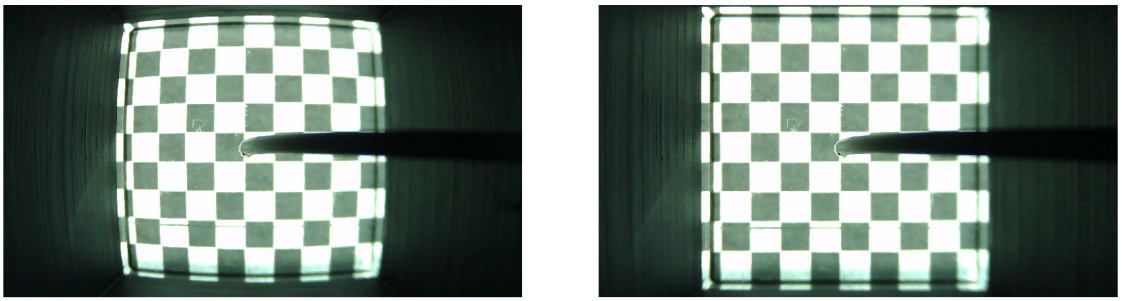

(a) The image of the chequerboard pattern before correcting for distortion. (b) The image of the chequerboard pattern, corrected for distortion.

Figure 5.8: Camera distortion.

It will also be important to have the transmitting fiber at the centre of the image. In Fig. 5.9a, the image corrected for distortion of the light spot can be seen. The white lines in the image indicate the centre lines of the image, at pixel row 540 and pixel column 960, since the resolution of this image is 1920x1080. In the image, it can be seen that the centre of the transmitting fiber is not the centre of the image. This can be corrected by finding the light spot in a similar way as done in section 4.3.3. The centre point of the light spot can then be calculated. The rows and columns of the image are moved till the centre point of the light spot is equal to the centre point of the image. The result can be seen in Fig. 5.9b.

5.2.3. LED to fiber coupler

The LED to fiber coupler, as seen in Fig. 5.2a, couples the light coming out of the LED into the transmitting fiber. The distance between the fiber end and the LED has a big influence on the power of the coupled light and thus the size of the light spot. A tight fitting for the transmitting fiber is made to minimize the motion; however, the distance can still vary slightly between two separate measurements.

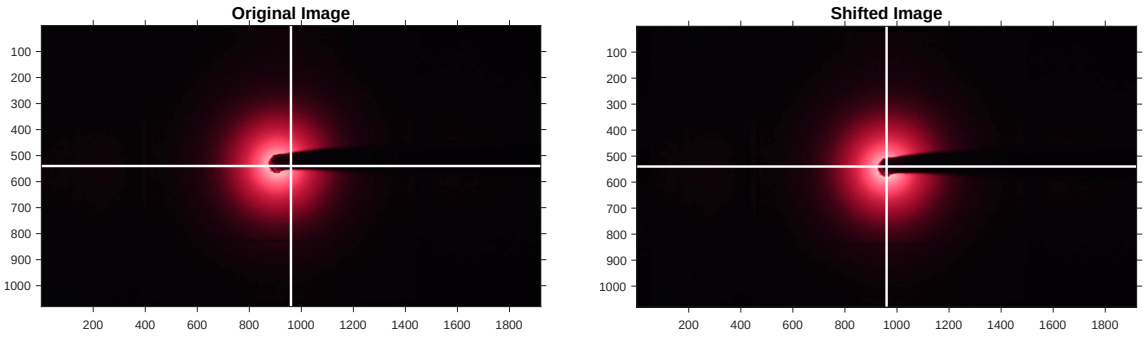

(a) A misalignment between the centre of the transmitting fiber and the centre of the image.

(b) The same image as (a), but corrected for the misalignment of the centres.

Figure 5.9: Misalignment of the camera. The white lines are at the centre positions of the image and the axis display the pixels column and row numbers.

During testing, it was found out that the LED itself had a non-constant brightness. When turned on, the brightness of the LED was at its highest and slowly decreased to a constant brightness. The settling time of the LED was found to be almost one hour.

5.2.4. Motion system calibration setup

The motion system is designed with a secondary step size of $0.6mm$ over 14 main steps for a total motion range of $41.4mm$. Main step 1 is when the object is fully at the bottom of the light spot and main step 14 is when the object is fully at the top of the light spot. A reference measurement is done with a digital calliper to find the actual step size after 3D printing. The distance that is measured will be between the bottom edge of the reference object, which is placed inside the slider and a fixed reference line. The reference line needs to be visible to the camera so that a pixel/mm value can be obtained by comparing the distance in pixels to the distance measured with the digital calliper in mm. The pixel/mm value is used as a conversion between pixels on the image and the real-world distance in mm and will be needed for later use.

The reference line will need to be straight, at a constant position and it needs to be visible to the camera. This limits the placement of the line to be on the PMMA plate holding the optical fibers. The reference line can be engraved into the PMMA by the laser cutter and can be seen in Fig. 5.4. The position of the line seen by the camera will be constant since the off-centre misalignment of the transmitting fiber is corrected for, as done in section 5.2.2 and seen in Fig. 5.9. The position of the transmitting fiber is fixed in the PMMA plate and thus correcting for its misalignment also ensures the constant position of the reference line. The reference line is placed at such a distance from the transmitting fiber that it can still be identified by image analysis during measurements free from the ambient light. This means that the line needs to be placed at the edge of the light spot. A downside of this is that the first steps, from main step 1 up to and including 5, can not be measured accurately.

5.3. Results

In this section, the results of the second experimental setup are given before image analysis is done. The accuracy of the motion system is calculated and the correct exposure setting for both cameras is discussed. Several steps of image analysis will be done in the next chapter.

5.3.1. Motion system accuracy and object position

The digital calliper used to measure the distance had a tolerance of $0.05mm$. Four separate experiments were done where all the steps between main step 6 up to and including 13 were measured. Step 14 was excluded since the object was fully out of reach of the light spot and main steps 1 up to and including 5 were also not measured. The result is shown in Fig. 5.10. It can be seen that the real distance is almost identical to the designed distance. Each measured step size is between 0.55 and $0.65mm$ for all four experiments, the variations are thus in the range of the tolerance of the digital calliper. The average measured step size of the four measurements is $0.5975mm$.

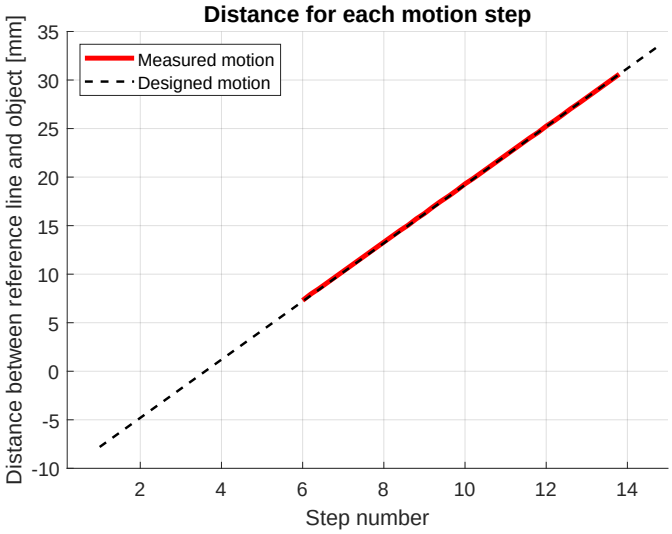

Figure 5.10: Measurement of each step of the motion stage. The step number refers to the main step number, of which there are fourteen. Each main step consists of five secondary steps. The dashed black line thus consists of 70 steps and the red line of 40 steps. The reference line is at a fixed distance of 13.05mm from the centre of the transmitting fiber. The distance measured is always the distance between the bottom edge of the object and the reference line. For step numbers 1 till 4 this becomes negative, meaning the bottom edge of the object is below the reference line.

The distance of the edge of the object to the reference line is now known for each step of the discrete motion system. The position of the reference line is fixed in the PMMA plate, as is the transmitting fiber and the distance between these is 13.15mm centre to centre. The distance between the bottom edge of the object and the centre of the transmitting fiber can thus be calculated for each motion step by subtracting the centre to centre value from Fig. 5.10.

5.3.2. Exposure settings

Camera facing the transmitting fiber

In the previous setup, in Chapter 4, one camera was used that looked directly into the light spot. In this updated setup, the position of this camera is changed so that it does not look directly into the light spot. In Fig. 5.11 the seen light spot by the camera can be seen for every exposure setting. Even though the camera does not directly look towards the light source, a blooming effect is seen. The blooming is caused by the diffuser which reflects light in every direction, also downwards to the camera.

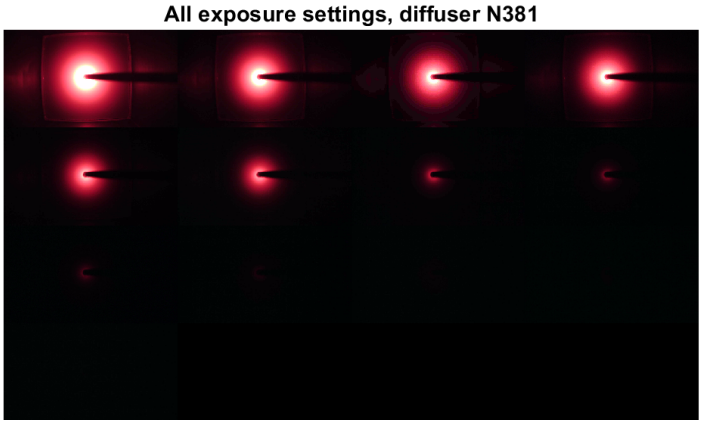

Figure 5.11: 13 images of the spot size of diffuser N381, with all possible exposure settings. The highest exposure is the top left image, counting down from left to right and from top to bottom.

To find the correct exposure setting, the same method as for the previous setup, as explained in section 4.3.1, is used. No extra object blocking the light source needs to be added since the transmitting fiber is already partially blocking the camera's view of the light source. In Fig. 5.12a, the pixel intensity values can be seen for the exposure setting -1 of the camera. At the position of the transmitting fiber, there is still some intensity captured. In Fig. 5.12b, the same picture is seen, but with exposure setting -5 of the camera. The intensity values are at zero as it should be, however at the centre of the light spot a slight blooming effect is still noticed. This also occurs at lower exposure settings and is thus unavoidable. All pictures with the camera looking at the transmitting fiber will be taken in both exposure setting -5 and -6.

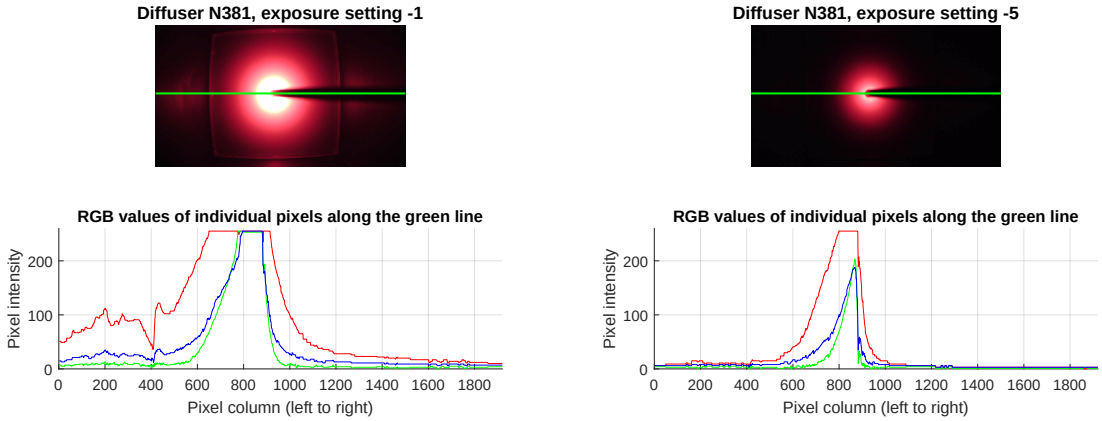

(a) Intensity values for the exposure setting -1

(b) Intensity values for the exposure setting -5

Figure 5.12: Using the transmitting fiber as a reference that should remain black: zero intensity values for all colour layers. The pixel intensity values are tracked along the green line and shown for all colour channels.

Camera facing the receiving fibers

A second camera is added that only looks at the ends of the receiving fibers. The intensity seen by this camera is much lower, as only the transmittance from the transmitting fiber to the receiving fibers is seen. In Fig. 5.13 the received picture can be seen for exposure setting -3. With a higher exposure setting, the maximum intensity of 255 is reached and with a lower exposure setting, the intensity will drop down too far. It is worth noticing that the new camera does not suffer from noise, as can be seen in the RGB values in the dark regions.

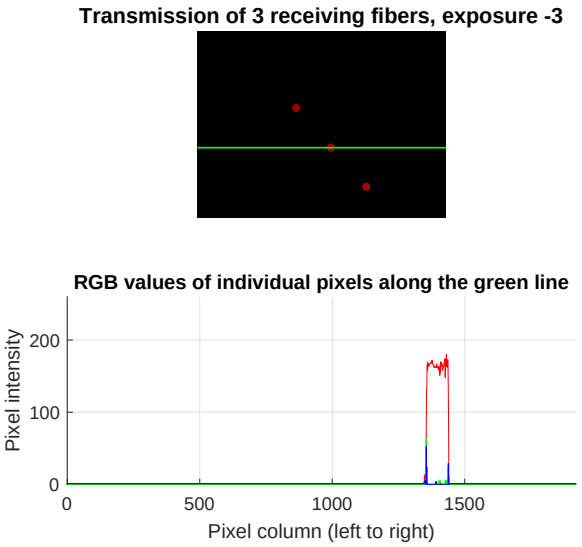

Figure 5.13: The received picture of the transmittance of the receiving fibers. In this case three receiving fibers were placed in the light spot area.

5.3.3. Reference object

As explained in section 5.1.4, two types of surfaces are used as a reference object. A white painted metal strip resembling a fully diffuse object and a metal strip polished to a mirror finish resembling a fully reflective object. Several pictures were taken with both objects in the same position. No visible difference was seen in the intensity of the spot between the two types of objects. In Fig. 5.14, the two different reference objects can be seen. Due to the similarity between the two objects, it was decided to continue the testing with only the polished piece of metal as its edge was slightly better defined than the painted piece of metal.

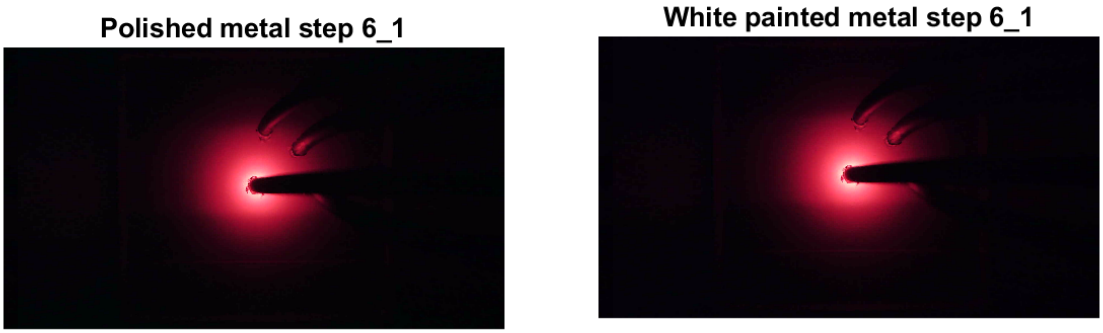

(a) A picture of the polished metal piece at main step 6, subindex 1.

(b) A picture of the metal piece coated with a white paint at main step 6, subindex 1.

Figure 5.14: Two pictures on the same motion step of the two different objects.

5.3.4. Object motion as seen through a diffuser

The position of the object during an experiment, so with only the light of the transmitting fiber and no ambient light, can be hard to track by eye. In Fig. 5.14, two edges can be seen, one edge slightly below the transmitting fiber (the centre point of the image) and one edge in the outer region of the light spot on the top. In Fig. 5.15, several positions of the object are shown moving from the bottom to the top. For clarity, the top edge of the object is indicated by a white line and the bottom edge of the object by a green line. The object is difficult to see; however, a rough change in the spot shape and intensity can be seen.

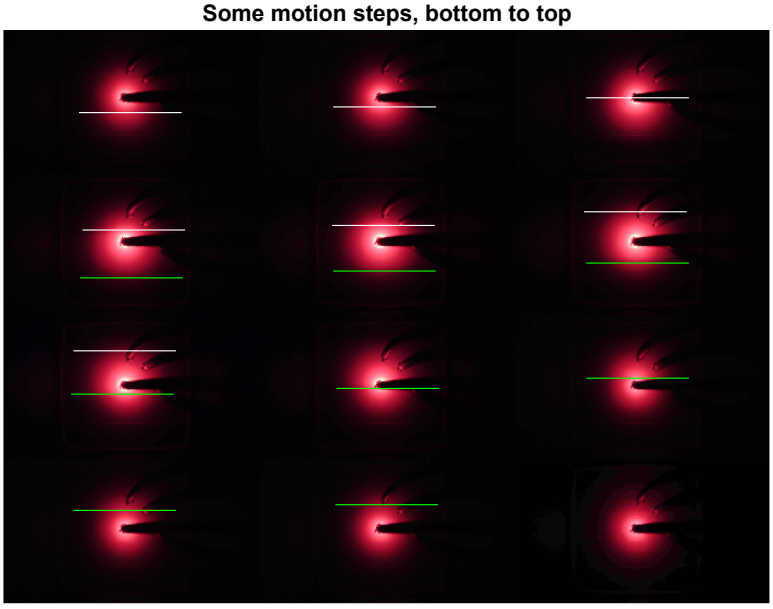

Figure 5.15: A few, but not all, steps of the full motion with the object moving from the bottom to the top. The top edge of the moving object is indicated by a white line and the bottom edge by a green line.

5.4. Conclusion

In this chapter, the second experimental setup is designed. It is an evolution of the first experimental setup from Chapter 4. This updated setup can look at both the received light spot and at the transmission into the receiving fibers. It was derived that rotating the position of the receiving fiber is equivalent to a different angle of motion of the moving object. It was also derived that symmetry in the received signal of the receiving fiber can be expected. This allows for a prediction of the behaviour for all possible angles of motion of the object while knowing information about only a few angles of motion. A simple, discrete motion system is designed which has an accuracy in the order of the tolerance of the used digital calliper of $0.05mm$. The real position of the object is known for every motion step of the discrete motion system. The received pictures are ready for image analysis and data manipulation, which will be done in the next chapter.

6

Image analysis and data manipulation

This chapter describes the intermediate steps between a received picture, from Chapter 5 and object tracking using optical fibers in Chapter 7. The steps that are required will be explained first, then the methods of each step are explained and their results are discussed.

6.1. Steps required

The final goal of this thesis is to show the feasibility of tracking the edge of a moving object by only looking at a small dot in the measurement plane. This small dot is the receiving fiber. In the previous chapter, the experimental setup has been made that captures images of a moving flat object across a plane. However, to track the edge of a moving object, image analysis has to be done on the received images. Several steps of image analysis will need to be made. Firstly, the edge of the moving object is tracked with the camera to compare the distance in pixels of each step to the measured distance. This gives a conversion value in pixel/mm. An optimization is done on the placement of the receiving fiber with respect to the transmitting fiber, based on a comparison between the vision of both cameras. After this, the received data is extrapolated to form a complete surface of all possible intensities for each angle of motion of the object. This surface is then fitted with a continuous equation.

6.2. Motion system and conversion factor

While measuring the distance with the digital calliper for each step, as done in section 5.3.1, a picture was taken with the camera looking at the object and the reference line. There were thus 40 pictures taken for each full experiment, for a total of 160 pictures. An image recognition algorithm is made using MATLAB that recognizes the position of the reference line and the edge of the moving object for each picture.

In Fig. 6.1a and 6.1b, two of those pictures can be seen for two different positions of the object. In the pictures, a vertical red line is drawn on the position where the pixels are read out and where the measurement with the digital calliper took place. In the graph below the pictures, the readout of that pixel line can be seen. Coloured rectangles are placed at sections with high and low intensities, and these can be identified by their colour in both the picture and the graph.

Points of interest are the reference line and the edge of the object. The reference line is placed at the red square and can be seen as a peak in intensity at around pixel row 820 to 840. This reference line is at a constant position throughout all pictures. The other point of interest, the edge of the moving object, is the transition between the higher intensities of the ambient light at the blue rectangle and the darker area of the slider, the green rectangle. This point changes with each new position of the slider. As explained at the beginning of this section, only the position of the bottom edge of the moving object is measured.

6.2.1. Reference line

The position of the reference line in pixel position is found using the fact that it is always at roughly the same position. All the pixel intensity values within a range of 50 pixels of pixel row number 810 are set to NaN. This

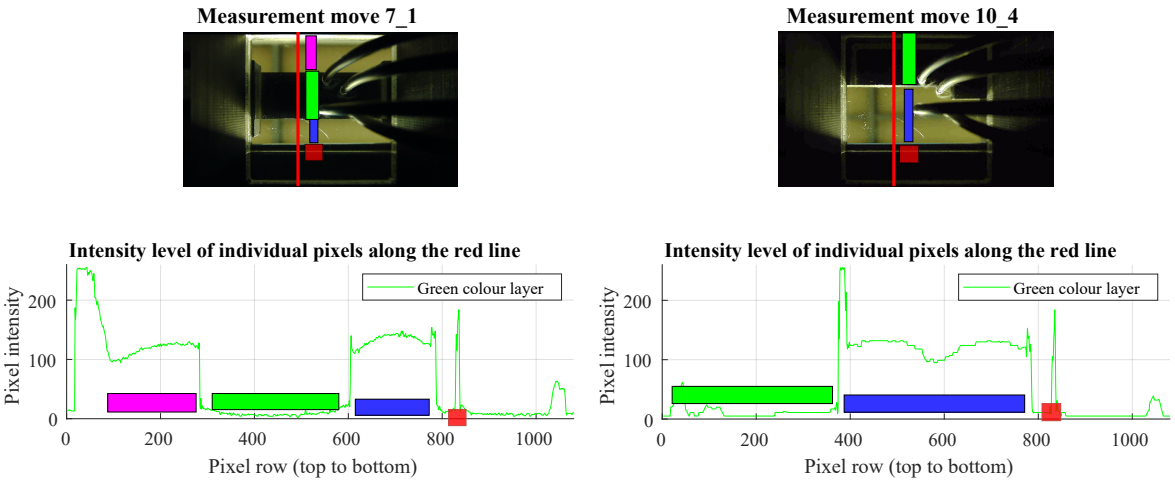

(a) Picture of the main step number 7 with secondary step 1 and the intensities of each individual pixel plotted in the graph for the green colour layer.

(b) Picture of the main step number 10 with secondary step 4 and the intensities of each individual pixel plotted in the graph for the green colour layer.

Figure 6.1: Two pictures of two separate positions of the object. The red rectangle is the intensity peak of the reference line. A dark object was placed over the reference line when taking the picture for visibility of the intensity peak. The blue rectangle is the ambient light that is captured by the camera between the moving object and the reference line. The green rectangle is the dark area of the moving object and the purple rectangle the ambient light at the other side of the moving object. The rectangles are placed in the picture and their corresponding position in the pixel intensity graph.

simplifies the entire graph as seen in Fig. 6.1a and 6.1b. To make it easy to recognize the reference line, a dark object was placed above it and thus the reference line can be seen as a peak of the pixel intensities. The peak is not constant in intensity, due to the variation of the ambient light. The ambient light is in some situations higher in intensity than the peak of the reference line, so selecting the maximum value does not yield the same pixel every time. Another approached proved to be working correctly, namely to find the biggest increase in pixel intensity within 3 pixels.

For all 40 pictures for each experiment, a position of the reference line is found. The results of the developed algorithm on the measurements are visualized in a box plot, seen in Fig. 6.2a and in a histogram, seen in Fig. 6.2b. In the box plot, the red line indicates the median position and the size of the box indicates the lower 25% and the upper 75% percentiles of the spread. The whiskers indicate the minimum and maximum value of the found pixel position. The outliers are indicated by the individual red markers. From the box plots, it can be seen that for experiment 1, 3 and 4 the spread of the points is so narrow that the box plot is reduced to only a line with a few outliers. For experiment 2, the box is much larger due to another position being found. This can be seen better in the histogram plot of experiment 2 in Fig. 6.2b. The actual position is pixel number 823/824, but due to the sunlight shining into the camera in some pictures, an offset is created leading to pixel number 837. The variation between each separate experiment is likely caused by a change in the position of the camera, even though efforts were made to minimize this. The developed algorithm can found in Appendix A, MATLAB code A.1.

6.2.2. Edge of moving object

The other point of interest is the edge of the moving object. In Fig. 6.1a and 6.1b this edge is the transition between the blue and green rectangle. Pixels beyond the range of motion of the slider edge will be set to NaN to avoid interference of those points. The algorithm for finding the edge of the moving object is in principle the same as for finding the reference line. The biggest increase in pixel intensity within 3 to 5 pixels is the edge of the moving object since the object is dark and the ambient light is much brighter. This gives accurate results for the first motion steps. At later steps, the edge of the slider becomes visible and reflects the sunlight, resulting in several intensity peaks, as can be seen in Fig. 6.1b between the green and blue rectangle. In the algorithm, it is recognized when this happens and corrected for. The step size of each motion step in pixels is calculated by taking the difference of the consecutive positions of the object edge. A consequence of calculating the step size this way is that an offset of 1 pixel in locating the edge of the moving object will lead to an error of 1 pixel of two calculated step sizes. This is because each position is used to calculate two step sizes.

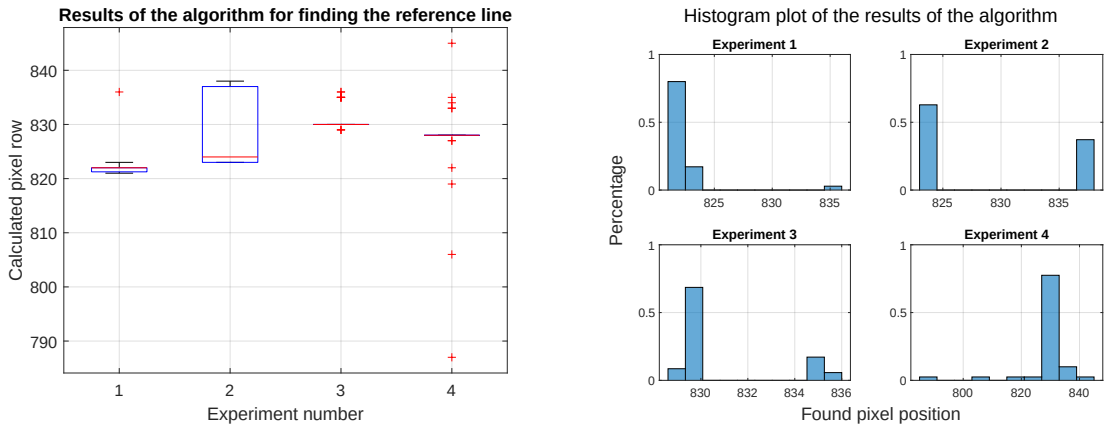

(a) The results of the algorithm for finding the pixel position shown in box plot form. The red line is the median of the spread, with the box indicating the size of the 25th to the 75th percentiles. The outliers are the red markers.

(b) Histogram plot of the same results leading to the box plot in (a). A measurement error due to the sunlight in experiment 2 led to the secondary peak at pixel position 837.

Figure 6.2: The results of the algorithm for finding the position in pixels of the reference line shown in box plot form (a) and in histogram form (b).

The results for each separate experiment can be seen in the box plots in Fig. 6.3. The box plot can be interpreted the same as in section 6.2.1, where the red line is the median of the spread and the size of the box indicate the lower 25% and upper 75% percentiles of the spread. The whiskers are different and are set to indicate the 5% and 95% percentiles. The average and median step size is -13 pixels with 90% of the data within the range of 11 to 15 pixels. The developed algorithm can be seen in Appendix A, MATLAB code A.2.

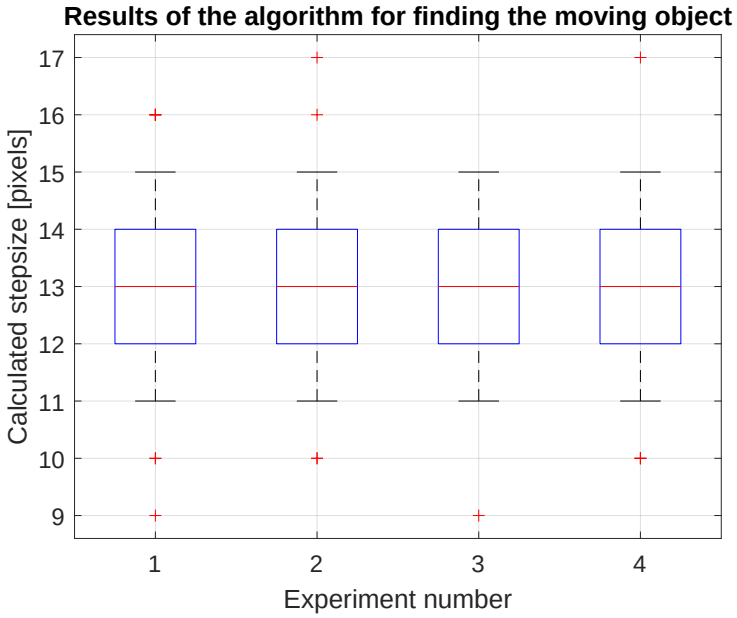

Figure 6.3: Box plot of the result of the algorithm for finding the edge of the moving object. Since the position in pixels of the edge of the object is different for every step, the result are shown in the form of the step size of each consecutive motion step. The red line is the median and the average value of the step size for each experiment. The size of the box indicates the size of the 25th to the 75th percentiles and the whiskers indicate the 5th to the 95th percentiles. The outliers are indicated by the red markers.

6.2.3. Pixel to mm conversion factor

With the position in pixels of the moving object and reference line known, the distance in pixels between the edge of the object and the reference line can be calculated. The most common found point for the refer-

ence line for each measurement is used. The distance in pixels is divided by the distance in mm to get the conversion factor:

$$\text{Conversion factor} = \frac{\text{Distance pixels}}{\text{Distance mm}} \tag{6.1}$$

The conversion factor is calculated for all the measured steps and averaged between the four experiments. The results can be seen in Fig. 6.4, plotted with one standard deviation. It can be seen that the uncertainty is higher at the earlier steps. This is because the edge of the moving object is not clearly seen. At later steps, the side of the slider becomes visible and the edge of the metal reference object can be identified more accurately. The average conversion factor across the entire picture equals to 21.7 Pixels/mm.

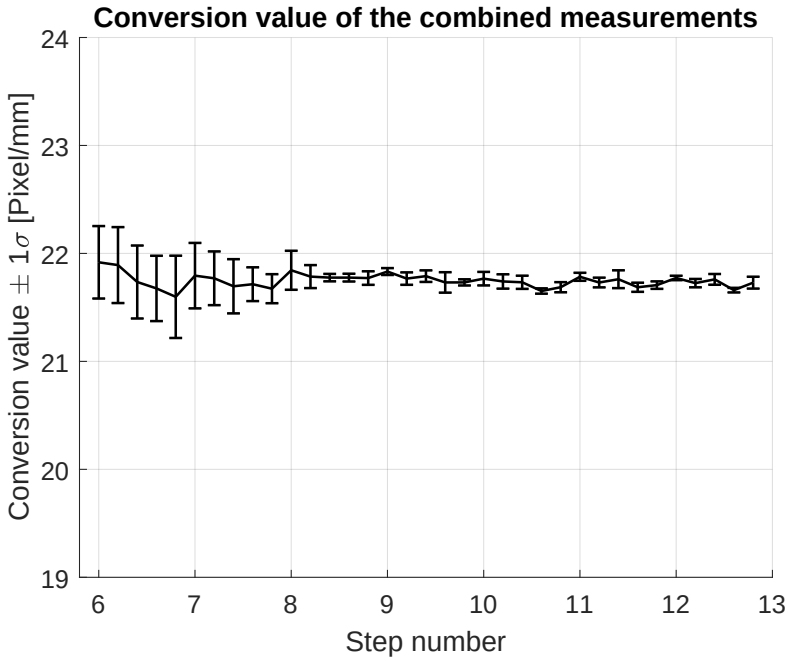

Figure 6.4: The conversion factor calculated for each measured step, with one standard deviation uncertainty plotted.

6.3. Simulation of the receiving fiber

Before the receiving fiber is placed in the PMMA plate, the received transmission of the receiving fiber can be simulated using the camera's vision of the light spot. A receiving fiber can be simulated by combining the pixel values of a group of pixels, at the same position and the same size as the optical fibers. The fiber core is $1mm$ in diameter and the conversion factor is 21.7 Pixel/mm, as calculated in Fig. 6.4. The intensity of the set of pixels will vary when the object moves over. The closer the receiving fiber is placed to the transmitting fiber, the more light it will receive. This is because the light spot is at is brightest in the centre and slowly dies out the further it will be from the centre.

Several positions of the receiving fiber and its transmittance can be seen in Fig. 6.5 below. The fibers are all placed at the 180-degree position so, in this situation, the object covers the receiving fibers and the transmitting fibers at the same time, as was schematically shown in Fig. 5.3a. The object moves from the bottom to the top and reflects the light back towards the diffuser, creating regions of higher intensity at its position. In Fig. 6.5 each simulated receiving fiber has its own colour. Its position in the light spot and its corresponding transmission graph can be seen. The receiving fiber placed closest to the transmitting fiber has indeed the highest intensity. The intensity is however constantly at the maximum value of 255 and no variation is detected of the moving object. Similarly, when the receiving fiber is placed far away from the light source, for instance 350 pixels (=12.6mm), the variation in low and high intensity is also low, as seen from the yellow line.

There is a visible transition between object not over the receiving fiber and object over the receiving fiber.

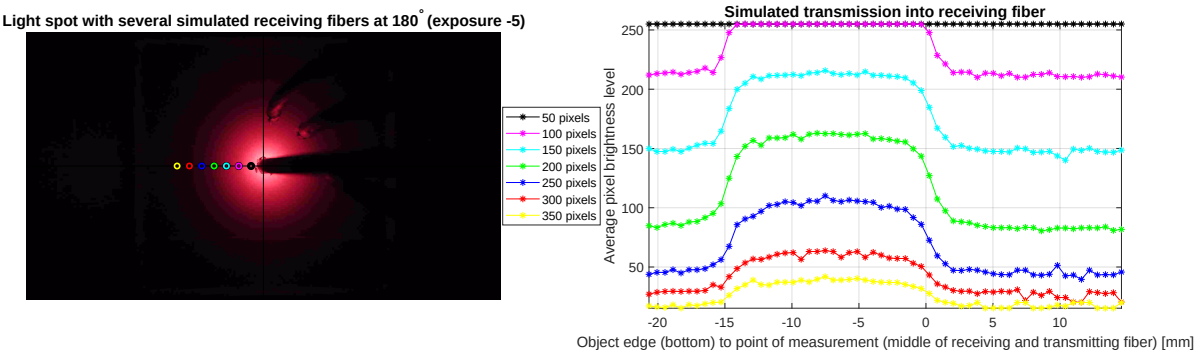

Figure 6.5: On the left side, a picture of the light spot is seen, with several receiving fibers simulated at various distances to the transmitting fiber (picture centre). The distance in pixels can be seen in the legend for each receiving fiber. On the right side, the simulated transmission can be seen for each motion step of the moving object, moving from the bottom to the top. In the graph, the transmission (average pixel brightness) is plotted against the known position of the object edge with respect to the point of measurement for each measurement step. The point of measurement is in the middle between the receiving fiber and the transmitting fiber, as was explained in section 5.1.1. Sections of high and low intensity can be seen in the graph, with a transition between the sections. The section of high intensity means the object is fully over both the receiving and transmitting fibers. The section of low intensity means that the object has no more influence on the light intensity at the position of the receiving fiber and is thus out of reach of the receiving fiber.

When the object is not over the receiving fiber, the intensity is low and when the object is over the receiving fiber, the intensity increases. With the receiving fiber placed at the 180-degree position, this transition happens exactly when the edges of the object move over the transmitting and receiving fibers, at $-15mm$ for the top edge of the object and at $0mm$ for the bottom edge.

With other angles of motion of the object, which is similar to a different angular position of the receiving fiber as was explained in section 5.1.1, different transitions can be expected. With the receiving fiber placed at 180 degrees, the object edge moves over both the transmitting and the receiving fiber at the same time. In Fig. 6.6 and 6.7, the angle of the receiving fiber is 135 and 90 degrees respectively. It can be clearly seen that the transmission signal is different for each angular position of the receiving fiber. It is also noticed that instead of one transition from low to high intensity, as in Fig. 6.5, two transitions occur. This is because the receiving and transmitting fiber are not covered by the object at the same time, as was the case when the receiving fiber is placed at the 180-degree position. The shift of each line for the different positions of the receiving fiber is caused by the shift of the point of measurement, as this is dependant on the distance between the receiving and transmitting fiber.

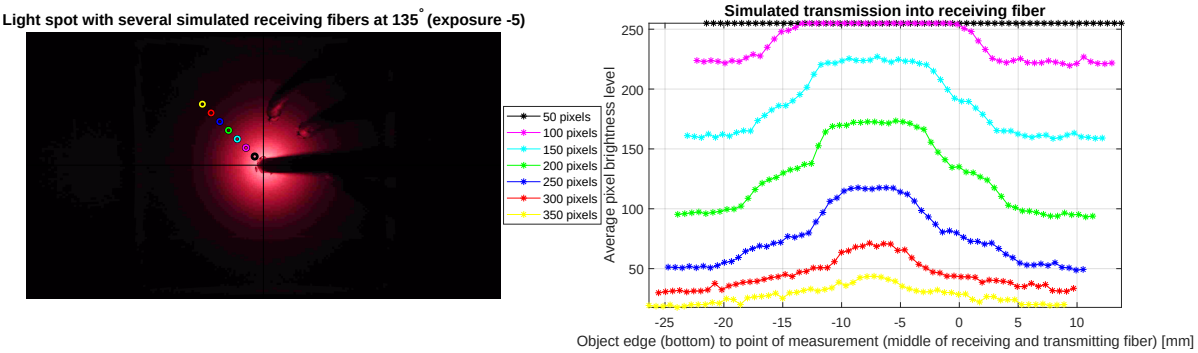

Figure 6.6: Similar situation as Fig. 6.5, but with the receiving fiber placed at the 135-degree position. It can be seen that instead of one sharp transition from high to low intensity, the transition is smoother and consists of two steps. The point of measurement shifts for each position of the receiving fiber, causing a shift in each line. This is because the point of measurement is dependent on the distance between the receiving and transmitting fiber, as explained in section 5.1.1. The zero point on the x-axis is thus always in the middle between the high and low intensity; in the middle between the receiving and transmitting fiber. Directly before and after the zero point, the object edge crosses over the transmitting and receiving fibers respectively. Similarly, at $-15mm$, for the other edge of the object, since the object is $15mm$ in diameter.

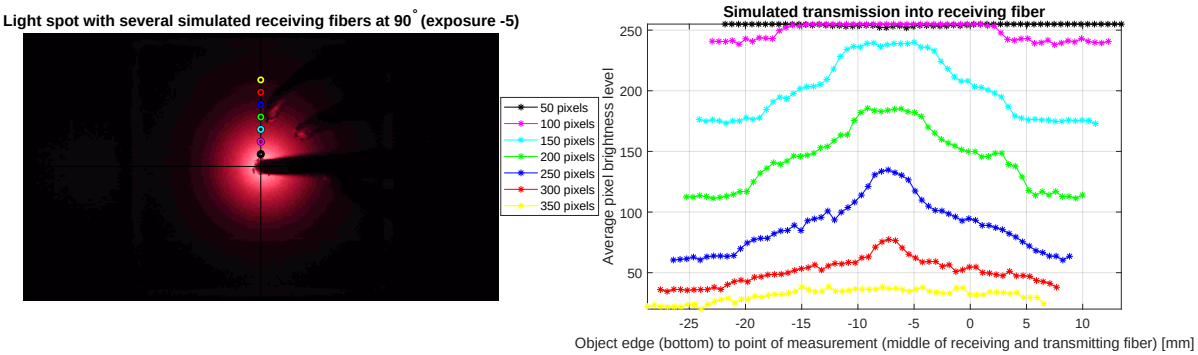

Figure 6.7: Similar situation as Fig. 6.6, but with the receiving fiber placed at the 90-degree position.

The measurement reach of the receiving fibers is equal to the length of the transition between the low and high intensity levels. From the figures it can be seen that this transition is dependant on the angle of motion of the object. The shortest transition is at the angle of motion of 0 and 180 degrees and is roughly $4.2mm$. The longest transition is at the angle of motion of 90 and 270 degrees and is roughly $10mm$. The larger the relative distance between the receiving and transmitting fiber, as seen from the moving object, the longer the transition is and thus the larger the measurement reach of the receiving fiber is.

6.3.1. Optimal placement of receiving fiber

As shown in the previous section, the height of transition between high and low intensity is dependent on the distance between the transmitting and receiving fiber. A higher transition would allow for a better and clearer distinction between the two intensity levels. It is thus desired to have a large difference between the high and low intensity levels.

From the figures in the previous section, Fig. 6.5, 6.6 and 6.7, it can be seen that when the receiving fiber is placed very close to the transmitting fiber, the transition goes to zero due to the low intensity level being too high. It can also be seen that when the receiving fiber is placed far away from the transmitting fiber, the transition also goes to zero, in this case, due to the high intensity level becoming too low. An optimum can thus be found on the position of the receiving fiber that would give the largest transition between the two intensity levels.

The way this is done is similar to the simulation as done in the previous section 6.3. Instead of simulating with a 50 pixel difference between the receiving fibers, a difference of 5 pixels is taken between 50 to 350 pixels from the centre of the transmitting fiber. This is equal to a distance of 2.3 to $16.1mm$, using the conversion factor of 21.7 pixels/mm as derived in section 6.2. The receiving fibers are also simulated on the angular positions between 180 and 90 degrees with a 1-degree step size.

Each simulated position of the receiving fiber has a different high and low intensity level. These levels are found and subtracted from each other. An optimum position is found for different exposure settings of the camera. For exposure setting -5, the optimum position was 250 pixels (=$11.5mm$) from the centre of the transmitting fiber. For exposure setting -6 of the camera, the optimum position was 200 pixels (=$9.2mm$) from the centre of the transmitting fiber.

What an actual receiving fiber will see can vary from the results of the described simulation. The camera is placed at a different position and has a larger numerical aperture compared to the optical fibers. Experimenting with a large array of receiving fibers at different positions with small steps in between is not possible due to the diameter of the optical fibers. Instead, the found optimal positions for the different exposure settings resulting from the simulations are used, along with one position closer to the centre of the transmitting fiber.

The results can be seen in Fig. 6.8 for a small part of the complete motion, with the receiving fiber at the 180-degree position. In the top graph, the transmission is shown with the receiving fiber placed $5mm$ from

the transmitting fiber. In the middle graph, the distance between the fibers is $9mm$ and in the bottom graph $11.35mm$. The lines in the graph show the experimental and simulated transmission into the receiving fiber. The trend of the lines is similar in shape, but different in intensity compared to the received trends of the simulations. The transition between high and low intensity happens at the same point as in the simulation and the difference between the two intensity levels is comparable to the differences resulted from the simulations.

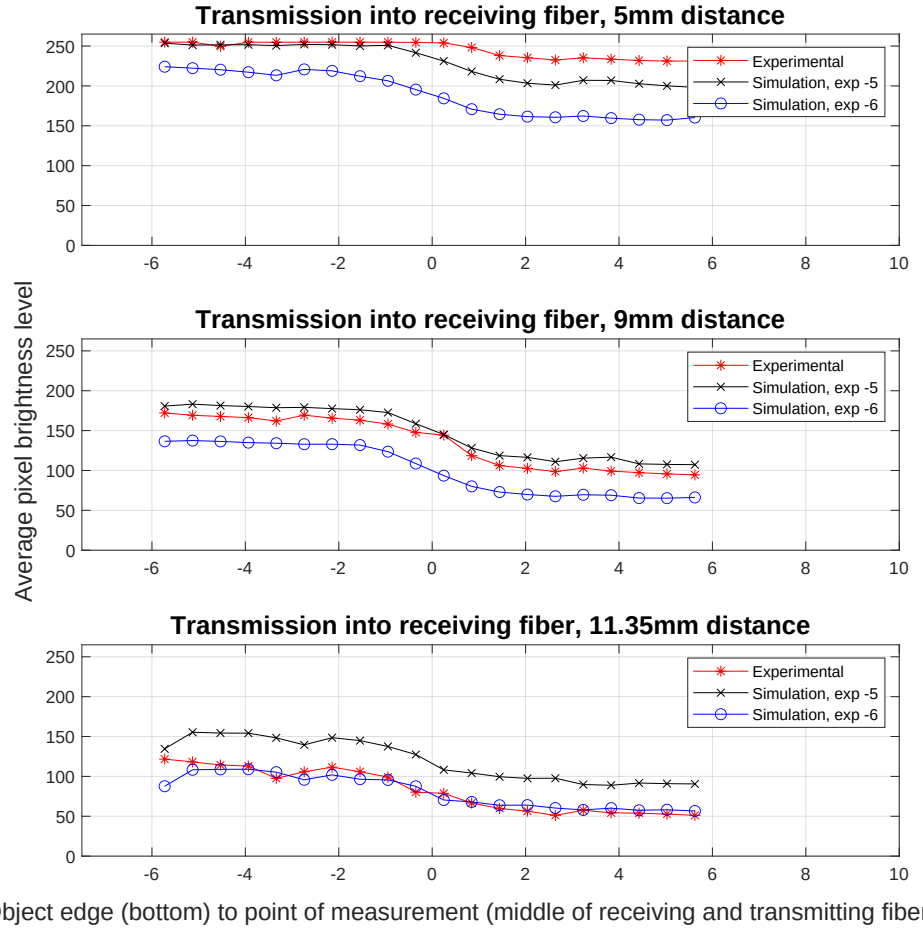

Figure 6.8: Three graphs of the receiving fiber placed at different distances from the transmitting fiber. The receiving fiber is at the 180 degree position. The three lines in each graph show the experimental and simulated transmission for the two different exposure levels. The experimental transmission was captured by the second camera looking directly at the ends of the receiving fibers, as is shown in Fig. 5.2a.

Of the three tested distances, placing the receiving fiber $9mm$ away from the transmitting fiber gave the largest difference between high and low intensity. This distance will be used for further testing of the transmission for different angular placements of the receiving fiber. The experimental measurement reach of the receiving fiber at this distance is the same as the simulated measurement reach given in the previous section of $4.2mm$ to $10mm$.

6.4. Comparison of the simulated vs experimental transmission

As explained in section 5.1.1, only one quarter of the circle of all angles of motion of the object is needed to fully define all angles of motion of the object. It was also derived that a rotation of the receiving fiber is equivalent to a different angle of motion of the object. Placing 90 different receiving fibers in the range of 90 to 180 degrees is however not possible due to the limited space available. Because of the limited space, three receiving fibers will be placed at the 0-, 40- and 80-degree positions, all placed at a 9mm radius from the centre of the transmitting fiber. This leaves half of the full light spot visible by the camera directly looking at the light spot and thus allowing a comparison between the simulated and experimental transmission into the receiving fiber.

6.4.1. Combining measurements

Eleven experiments have been done where the experimental setup was fully taken apart and set back up again. It was noticed that the coupling efficiency of the LED to fiber coupler was highly dependent on how close the fiber end was placed to the LED. This caused an offset between the different measurements for both the simulated and the experimental transmission. A segment of the full measurement can be seen in Fig. 6.9. In the top graph each separate simulation can be seen, uncorrected for the offset caused by the LED to fiber coupler. The offset is corrected by taking the average of a few points of each measurement that are in the low intensity region and setting them equal. The results of the simulation corrected for this offset can be seen in the bottom graph in Fig. 6.9.

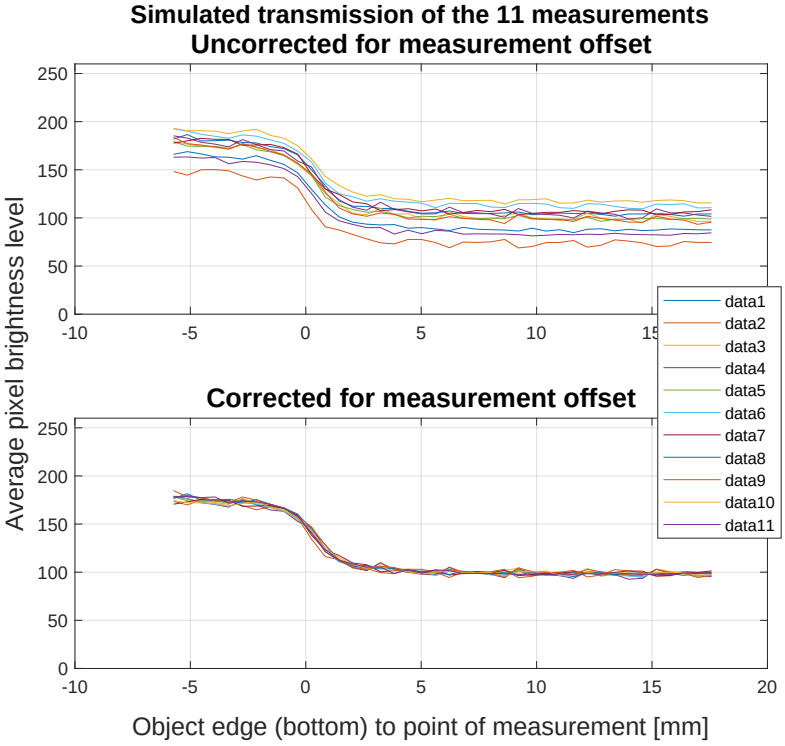

Figure 6.9: A section of the full motion for all eleven measurements. In the top graph the offset error is not corrected and differences in intensity across the entire trend can be seen. In the bottom graph the offset is corrected and the variation between the measurements is significantly reduced.

36 receiving fibers are simulated, spaced 2.5 degrees in between, across the range from 90 to 180 degrees. The results for the simulation can be seen in Fig. 6.10 in the top graph. The angles 180, 140 and 100 degrees are shown to compare with the results of the experimental transmission in the middle graph of the angles 0, 40 and 80 degrees. The shape of both graphs is similar as expected; however, in the simulated transmission, an increase in the low intensity level for each angle of motion can be seen. It is not known what causes this, as earlier in section 5.2.2, finding the full light spot showed a fully symmetric circle without any intensity increase in one half of the spot. This offset is corrected for by setting the low intensity levels for all angles equal to the low intensity level for the 180-degree position, as seen in Fig. 6.10 in the bottom graph. Each line is the average of the eleven measurements that were done and the one sigma uncertainty is indicated by the size of the marker on each point.

6.4.2. Data extrapolation

For the simulated transmission, 36 receiving fibers have been simulated at different angles between 90 and 180 degrees. The result of all the transmission trends at different angles in one surface plot can be seen in Fig. 6.11a. The separate transmission trends for all angles are plotted after each other, creating a surface of all possible transmission trends for the angles of motion between 0 and 90 degrees. A similar plot is also created for the experimental transmission, however for this only three transmission trends at different angles

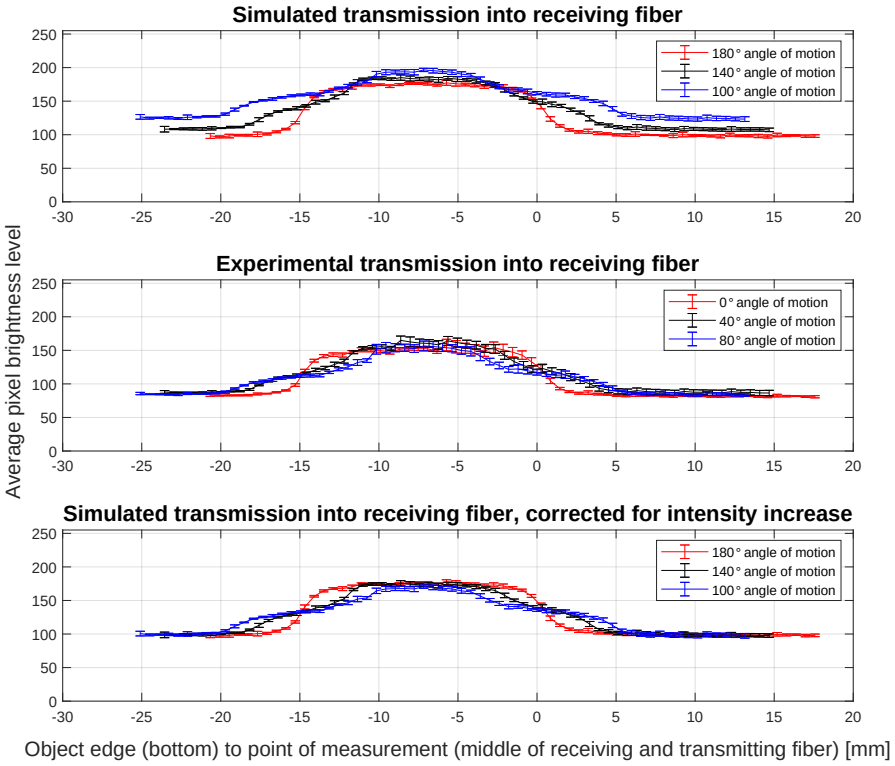

Figure 6.10: The results of the simulated and experimental transmission into a receiving fiber for three angles of motion. The drawn lines are the averages of the eleven measurements done, with one sigma uncertainty for each point indicated by the size of the marker. In the top graph the result of the simulation can be seen for the angles 180, 140 and 100 degrees. In the middle graph, the result of the experimental transmission can be seen, for the angles 0, 40 and 80. Due to the symmetry as explained in section 5.1.1, these result in the same transmission trends. For an unknown reason, the entire intensity level increases for different angles. With this corrected for, as shown in the bottom graph, the intensity trends match in shape.

are known, namely at 0, 40 and 80 degrees. The result can be seen in Fig. 6.11b, with one sigma uncertainty shown for each data point.

With the transmission of one quarter of all the angles of motion known, the data can be extrapolated to all angles of motion, as was explained in section 5.1.1. The transmission trends between 0 to 90 degrees are equal to the trends from 180 to 90 degrees. The transmission trends from 180 to 360 degrees are mirrored compared to the transmission trends from 0 to 180 degrees, with the plane of the mirror being in the centre of the high intensity section. This is at position $-7.5mm$, when the centre of the object moves over the measurement point since the object is $15.05mm$ in diameter. The result for both the extrapolated simulated and the experimental transmission can be seen in Fig. 6.12. The top figures, Fig. 6.12a and 6.12b, the surface is seen from the top. The black lines are of constant pixel intensity and the blue line are exactly in the middle of the high intensity section. The boundary conditions for extrapolating the data are that from 89 to 91 degrees, the blue lines must be constant and from 179 to 181 degrees, the black lines of constant intensity must be of the same value.

The resulting dataset of both the simulated and experimental transmissions show the same transmission trends. The transitions between the high and low intensity sections match; however, the intensities are different. This difference is caused by the fact that two different cameras are used for the simulated and the experimental transmission.

The dataset has to be interpreted as follows: for every motion direction (angle of motion) of a rectangular object and for all distances of the object edge to the measurement point, the intensity of the light that is received by the receiving fiber is known.

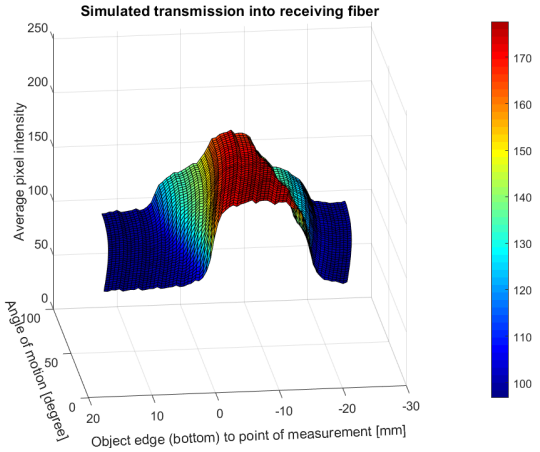

(a) The surface plot of the simulation, with 36 receiving fibers simulated at different angles, spaced 2.5 degrees apart.

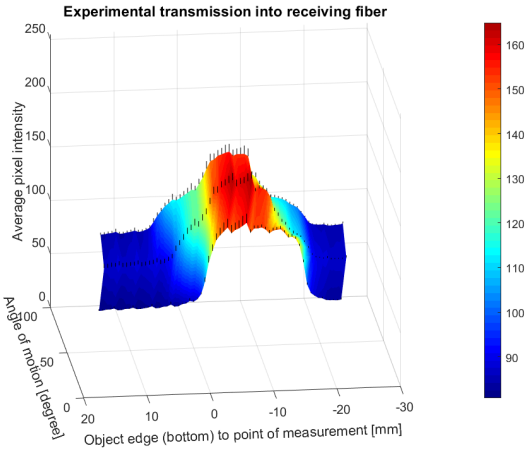

(b) The surface plot of the experimental transmission, created from three receiving fibers placed at 0, 40 and 80 degrees. The one sigma uncertainty of each point is indicated by the length of the markers.

Figure 6.11: Surface plots of all the simulated (a) and experimental (b) transmissions. The transmission trends for all angles are plotted after each other creating a surface of intensity levels for both the distance of the object edge to the measurement point and the angle of motion of the object.

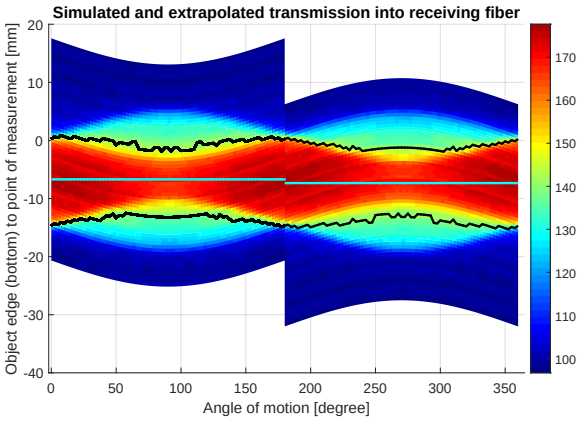

(a) The top view of the extrapolated simulated dataset. The black lines are of constant intensity and the blue lines indicate the middle of the high intensity section.

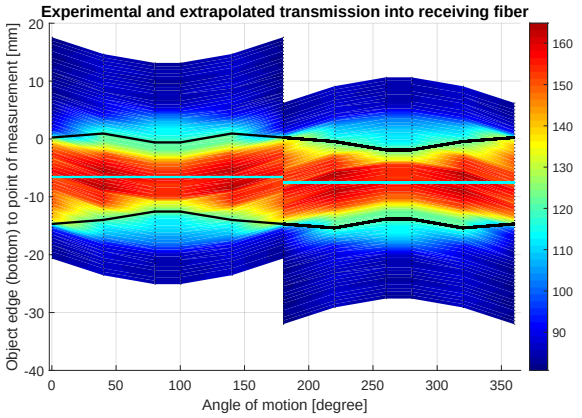

(b) The top view of the extrapolated experimental dataset. The black lines are of constant intensity and the blue lines indicate the middle of the high intensity section.

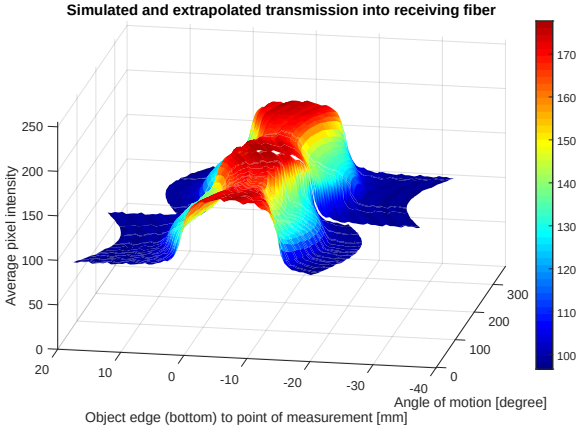

(c) The surface plot of the extrapolated simulation.

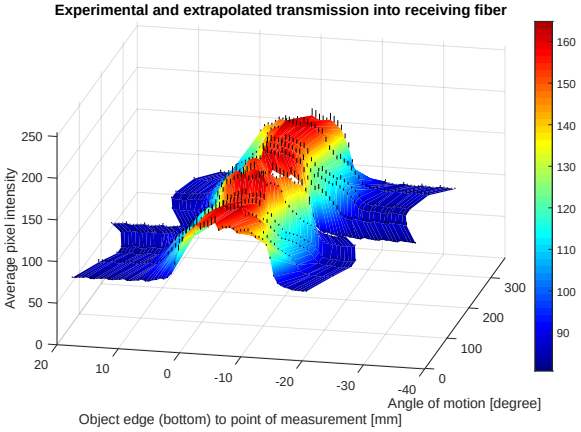

(d) The surface plot of the extrapolated experimental dataset. One sigma uncertainty is indicated by the length of the markers.

Figure 6.12: Surface plots of all the extrapolated simulated (a,c) and experimental (b,d) transmissions. The data as seen in Fig. 6.11 between 0 and 90 degrees is extrapolated to create an intensity plot for all angles of motion.

6.5. Equation fitting

The fully extrapolated data from the previous section is made up out of a limited number of transmission trends for the angles of motion. But next to this, it is also made up of discrete steps in the motion direction, since the motion system is a non-continuous system. This means that there is an interval, or gap, between the data points of each full motion range and angle of motion. By fitting a continuous equation into the data, any possible angle of motion and distance of object edge to measurement point as input would give an intensity as output. If successful, this can be inverted so that intensity as input would give an angle of motion and object position as output.

Ideally, a two-dimensional equation is fitted into the full surface as seen in Fig. 6.12. The equation would then completely describe the physics behind the data based on a hypothesis. The other option is to fit a one-dimensional equation separately into the transmission trends for a single angle of motion as seen in Fig. 6.10. With multiple equations fitted, the data can be combined and extrapolated again and its resulting surface fitted by a smooth interpolant. The last method is done in this section.

6.5.1. Equation type

From the transmission trend lines in Fig. 6.10, two main intensity levels can be identified, namely a high and low intensity level. The low intensity level indicates when an object is fully out of reach of the receiving fiber and the high intensity level indicates when an object covers both the receiving and transmitting fibers, as was explained in section 6.3. These intensity levels should be constant since no change should be observed besides the transitions between the intensity levels. The observed intensity differences in these levels are caused by the LED and the noise of the camera. An equation fit can filter out this noise.

Between the two intensity levels, two different shapes can be observed. The shape of the transition between low and high intensity is dependent on the angle of motion of the object and indicates when the receiving and transmitting fibers are covered by the edge of the object. At 0, 180 and 360 degrees, the edge of the object covers both the receiving and transmitting fiber at the same time, causing a steep slope between the intensity levels. The slope at these angles has the form of a single S-shape. At all other angles, the receiving and transmitting fibers are covered by the edge of the object separately, resulting in a double S-shaped transition.

A mathematical function that has an S-shape between two constant levels is the Sigmoid function. The base form of the function can be seen in equation 6.2. It is a smooth approximation of the Heaviside step function, which is zero for negative inputs and one for positive inputs. The base form of the Sigmoid function is also bound within zero and one.

$$S(x) = \frac{1}{1 + e^{-x}} \tag{6.2}$$

The Sigmoid function can be altered by adding some extra parameters in equation 6.2. The resulting equation will look like equation 6.3. In Fig. 6.13, the influence of changing the different parameters can be seen. d changes the height of the base level of the function and a the second level. c shifts the function and b changes the slope of the transition between the levels.

$$S(x) = \frac{a}{1 + e^{-b(x-c)}} + d \tag{6.3}$$

6.5.2. Fitting of experimental data

The extrapolated simulated and experimental transmissions follow the same trends. Since in the goal of this thesis is to design a concept base of an edge detection sensor system with the use of optical fibers, only the experimental data will be fitted.

One Sigmoid function can thus fully describe one transition. In the case of an angle of motion of 0, 180 and 360 degrees, two Sigmoid functions are needed, from the low to the high intensity level and one function to return to the low intensity level. For all other angles of motion, four Sigmoid functions are needed, due to the double S-shaped transition.

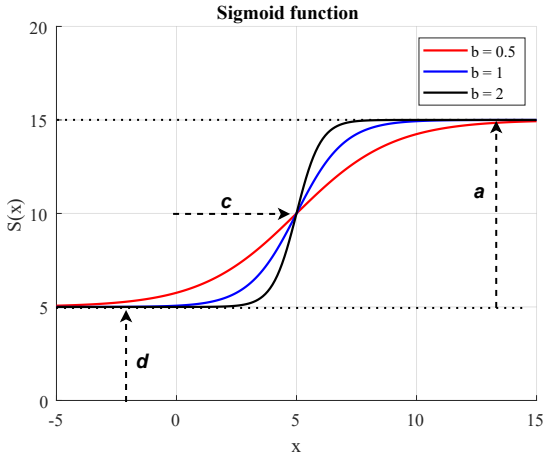

Figure 6.13: Three versions of the Sigmoid function plotted for $a = 10$, $b = [0.5; 1; 2]$, $c = 5$ and $d = 5$.

In equation 6.4, the double Sigmoid function can be seen and in Fig. 6.14a the fit can be seen. A few simplifications can be made to the equation.

- The slope of the transitions is equal, $b = b_1$.
- The low intensity levels are equal, $a_2 = -1$.
- The moving object has a width of $15.05mm$, thus $c_2 = c + 15.05$.

$$S(x) = \frac{a}{1 + e^{-b(x-c)}} \left(1 + \frac{a_2}{1 + e^{-b_1(x-c_2)}}\right) + d \tag{6.4}$$

In all other cases, four Sigmoid functions are needed to describe the full curve. The fits for angles of motion 40/140 and 80/100 can be seen in Fig. 6.14b and 6.14c respectively. In Fig. 6.15 the effects of the object covering and leaving the different fibers is schematically shown for the transmission trend of the angle of motion of 80 and 100 degrees. It can be seen that the transition from low to high and from high back to low are different. This is because in the transition from low to high ($-20mm$ to $-10mm$) the transmitting fiber is covered first (red arrow), followed by the receiving fiber (black arrow), while at the transition from high to low ($-5mm$ to $-7.5mm$) the transmitting fiber is left first (red arrow), followed by the receiving fiber (black arrow).

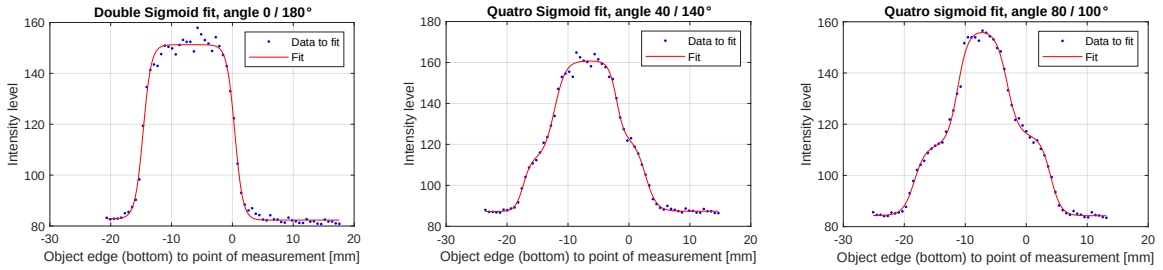

(a) Fit of the double Sigmoid from equation 6.4 into the transmission data of motion angle 0/180 degrees.

(b) Fit of the quadruple Sigmoid from equation 6.5 into the transmission data of motion angle 40/140 degrees.

(c) Fit of the quadruple Sigmoid from equation 6.5 into the transmission data of motion angle 80/100 degrees.

Figure 6.14: Results of the Sigmoid fits into the experimental data of the receiving fiber placed at three different angles.

Four Sigmoid functions are thus needed to fully describe the data. In equation 6.5, the quadruple Sigmoid function can be seen. Again, a few simplifications can be made to the equation.

- The slope of the transitions is equal, $b = b_3$ and $b_2 = b_4$.
- The low intensity levels are equal, $a_4 = -1$.
- The moving object has a width of $15.05mm$, thus $c_3 = c + 15.05$ and $c_4 = c_2 + 15.05$.

$$S(x) = \frac{a}{1 + e^{-b(x-c)}} \left(1 + \frac{a_2}{1 + e^{-b_2(x-c_2)}}\right)\left(1 + \frac{a_3}{1 + e^{-b_3(x-c_3)}}\right)\left(1 + \frac{a_4}{1 + e^{-b_4(x-c_4)}}\right) + d \tag{6.5}$$

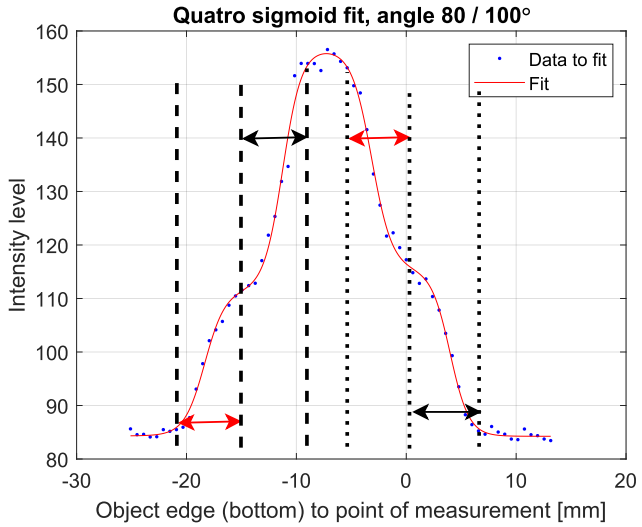

Figure 6.15: The transmission trend of the 80 and 100 degree angle of motion fitted with the quadruple Sigmoid function. The transition from low to high intensity ($-20mm$ to $-10mm$, dashed lines) differs from the transition from high to low intensity ($-5mm$ to $-7.5mm$, dotted lines). The red arrows indicate the section of the transition that is caused by the object covering the transmitting fiber and the black arrows indicate the section of the transition that is caused by the object covering the receiving fiber.

The equations are all fitted in MATLAB using the non-linear and least-squares method. All the variables a, c and d can be found visually using Fig. 6.13. The different values of b vary between 1.0 and 1.5.

6.5.3. Surface fitting

The resulting data fits of the transmission trends of the angles 0, 40 and 80 degrees can be extrapolated in a similar way as done in section 6.4.2. The resulting surface plot can be seen in Fig. 6.16. The transmission data is now continuous in the direction of motion of the object and it can be seen that the noise and measurement errors have been filtered out. It is however not continuous for all angles of motion, since only three transmission trends of three different angles of motion are fitted.

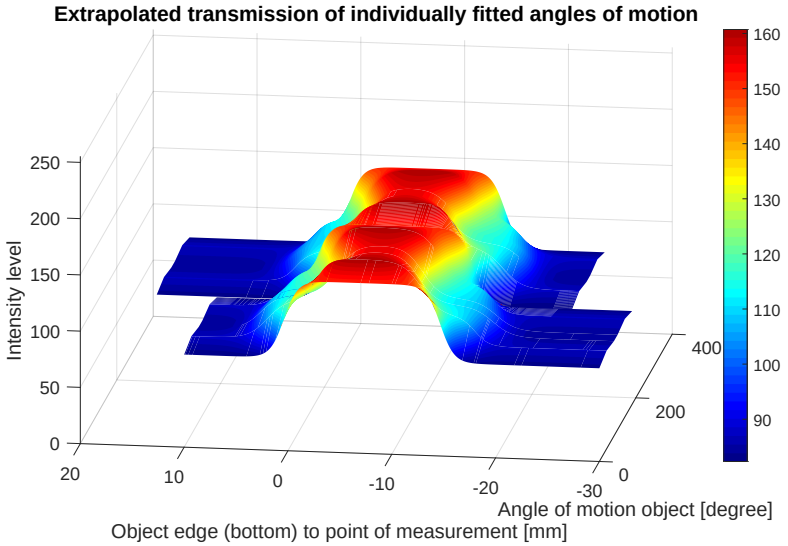

Figure 6.16: The resulting fits from Fig. 6.14 extrapolated to a full surface of intensities. The data set is continuous in the range of motion, but not in the angle of motion.

The entire surface of intensities can be made continuous in both the angle of motion, as well as the motion direction, by fitting a smooth interpolant into the surface as seen in Fig. 6.16. The resulting fit can be seen in Fig. 6.17 and remains in the same shape as before, but now continuous in all directions.

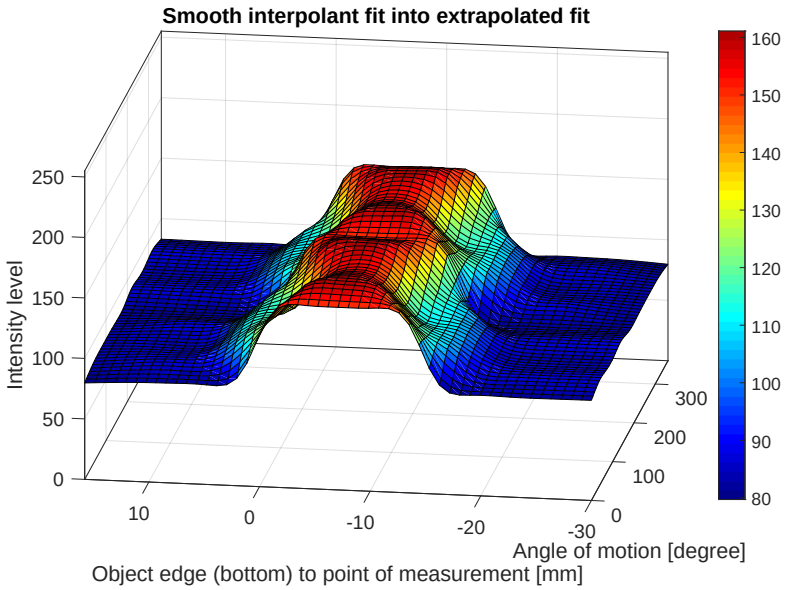

Figure 6.17: The partly continuous data set from Fig. 6.16 made fully continuous by fitting a smooth interpolant. Every possible intensity level received by the receiving fiber can be traced back to the object position and angle of motion.

6.6. Conclusion

In this chapter all image processing and data manipulating steps needed to track a moving object using optical fibers were done. The moving object is tracked by the first camera, resulting in pixel shift for every motion step. This shift in pixels is compared to the shift in mm from Chapter 5 to give the conversion factor of 21.7 pixel/mm. The conversion factor is used to find the optimal placement of the receiving fiber that followed from a simulation. The results of the simulation of the receiving fiber and the actual experimental transmission into the receiving fiber were compared and showed matching behaviour. The measurement reach of an individual receiving fiber is between $4.2mm$ and $10mm$, dependant on the angle of motion of the moving object. The limited amount of data points are extrapolated to form a complete surface of all possible intensities transmitted into the receiving fiber for each angle of motion. The data is made continuous by fitting several orders of the Sigmoid function into the data points.

7

Backwards calculations to object position and angle of motion

With the fully continuous result of the previous chapter, the edge detection can be validated with the experimental data, which is done in this chapter. Firstly, the observed intensity signals from one receiving fiber are processed to validate the possibility of sensing distances with an optical fiber. After that, the signals from multiple fibers are combined to define the angle of motion out of differences in intensities.

7.1. Data preparation

7.1.1. From pixel intensity to coverage percentage

In this thesis, only one set of receiving and measurement fiber is investigated; however, in a full sensor system with many of these building blocks, the base intensity seen by a receiving fiber can slightly vary. The continuous data set of the intensity level of the receiving fiber for all angles of motion of the object and for all distances of the object edge to the measurement point from Fig. 6.17 can be altered so that the intensity level goes from 0% to 100%. 0%, or near 0%, would indicate that the object is fully out of reach of the receiving fiber and 100% would indicate that the object is fully over the receiving fiber. This can also be seen as a calibration step for each building block of receiving and transmitting fiber. The resulting surface plot can be seen in Fig. 7.1.

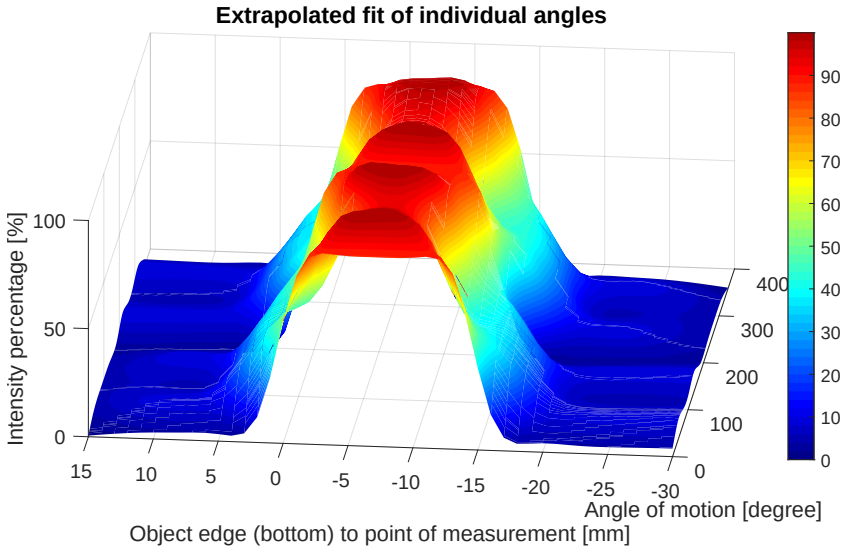

Figure 7.1: The surface plot from Fig. 6.17 with the pixel intensities on the z-axis swapped to intensity percentages.

7.1.2. Object approach and departure

The dataset shown in Fig. 7.1 shows the full motion of an object across a receiving fiber. The transition from low intensity to high intensity only occurs once: when the object is approaching the receiving fiber. This is between $-20mm$ and $-7.5mm$, and this transition is caused by the front edge of the object moving towards the measurement point. This is schematically shown in Fig. 7.2a. If a change in intensity is observed by the receiving fiber and the original intensity was low, the edge of the moving object is approaching and only the half of the dataset from $-20mm$ to $-7.5mm$ needs to be taken into account.

Similarly, the transition from high to low intensity also only occurs once, when the object is fully covering both the receiving and transmitting fibers (high intensity level) and moves away from the fiber set. This high to low transition is between $-7.5mm$ and $5mm$ and is caused by the back edge of the moving object. It is schematically shown in Fig. 7.2b. Thus, if a change in intensity is observed by the receiving fiber and the original intensity was high, the edge of the moving object is 'departing away' and only half of the dataset, from $-7.5mm$ to $5mm$, needs to be taking into account.

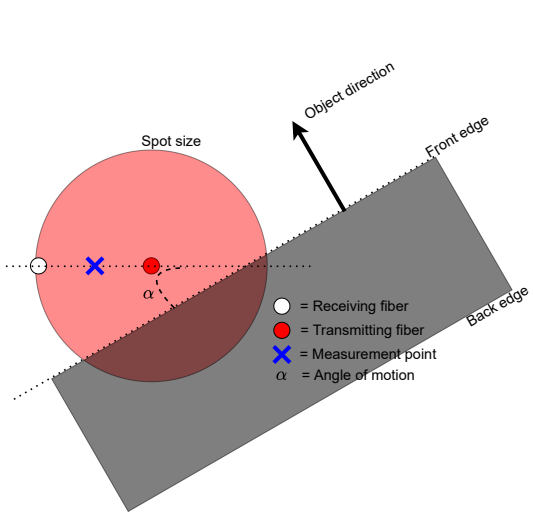

(a) The 'arrival' of the object. The seen intensity seen by the receiving fiber is low and increases when the front edge of the object moves closer towards the measurement point.

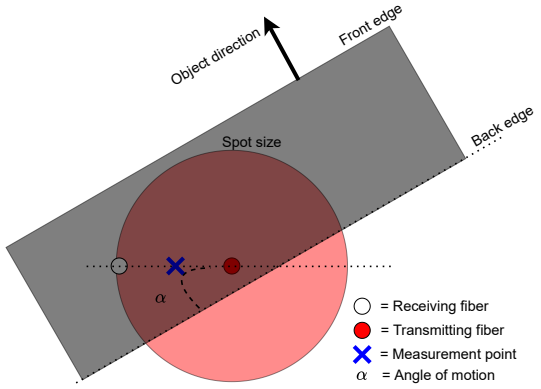

(b) The 'departure' of the object. The seen intensity seen by the receiving fiber is high and starts to decrease when the back edge of the object moves closer towards the measurement point.

Figure 7.2: The differences between arrival (a) and departure (b) of the edges of an object.

The full dataset from Fig. 7.1 can thus be separated into an 'approach' section and into a 'departure' section. This decreases the possible combinations of the angle of motion and object distance by half for a set of subsequent intensity points of the receiving fiber.

7.1.3. Inverse data-matrix

The continuous dataset from Fig. 7.1 is made up of an interpolant function with object distance and angle of motion as input, resulting in intensity as output. The function needs to be inverted so that intensity as input would give multiple possible combinations of the angle of motion and object distance as output. The interpolant function is however not invertible.

An alternative to the inverse of the function is to set up a data-matrix for all possible intensities. This is done by calculating the intensities using the interpolant function for all angles of motion with a one-degree difference and for all distances of the bottom object edge to the measurement point between $-30mm$ and $15mm$ with a difference of $0.01mm$. Any intensity level can then be given as input into the data-matrix, resulting in an object position for all angles of motion. This is shown in Fig. 6.12a and 6.12b in the previous chapter. In those figures, the black lines are at a constant intensity level for the 'approach' and 'departure' of the object, showing that any intensity level will give an object position for all angles of motion of the object.

7.1.4. Action plan

As explained in the previous section, any intensity level will give a range of possible positions of the object for all angles of motion of the object. Various methods can be used to determine the actual position and angle of motion of the object. One method is to measure in time, meaning that multiple subsequent intensity levels will be combined, assuming a constant velocity of the object. This comes down to finding a range of intensity points in Fig. 7.1, instead of finding only one intensity point. Measuring in time also allows the order in which multiple receiving fibers are covered by the object to be used as information to determine the actual position and angle of motion of the object.

Another approach to determine the actual position and angle of motion of the object is to look at the observed intensity signals from multiple receiving fibers at the same time. Each receiving fiber will give a unique intensity level, all leading to a range of possible positions of the object for all angles of motion. The actual angle of motion and position of the object could be deduced since the real distance between each receiving fiber and between their corresponding measurement points is known, due to their placement being fixed.

This thesis only looks at one set of transmitting and receiving fibers, as explained in the research objective in section 1.4 and in section 4.1. The second method where the observed intensity signals from multiple receiving fibers would be processed at the same time would be very suitable in the case of a large array of transmitting and receiving fibers. However, to show the achievable resolution of only one set of transmitting and receiving fibers, the first method will be done in this thesis.

7.2. Single fiber signal

In this section, the position and angle of the object are found only using the transmission signals of a single receiving fiber. In section 7.3, the transmission signals from multiple receiving fibers will be combined.

7.2.1. Angle of motion

A range of points of subsequent intensity levels is needed to define the angle of motion of the object. Due to the symmetry of the light spot, that was explained in section 5.1.1 and used to extrapolate the angles of motion between 0 and 90 degrees to a full range of motion between 0 and 360 degrees as done in section 6.4.2, four different possible outcomes can be expected when looking at half of the full dataset from Fig. 7.1. Two exceptions on this, is when the object is exactly at 0 or 180 degrees and exactly at 90 or 270 degrees, then only two outcomes of the angle of motion are possible.

An example can be seen in Fig. 7.3. If the real angle of motion of the object is for instance 10 degrees, an angle of motion of 170 degrees would give the exact same transition trend. Two other possible angles of motion would be 190 and 350 degrees, with the only difference that instead of the transmitting fiber, the receiving fiber is reached first, causing a slight difference in the intensity trend.

The real angle of motion can not be determined out of these four possibilities with one single receiving fiber. Multiple receiving fibers are thus needed to determine the angle of motion of the object.

7.2.2. From intensity to the position

Assuming the real angle of motion is known, the experimental data of all the measurements from section 6.4.1 can be used to determine the accuracy of a single receiving fiber. The received intensities of the experimental data are given as input into the data-matrix, as was explained in section 7.1.3. In Fig. 7.4a the experimental data can be seen for an angle of motion of 40 degrees, alongside the slice of the data-matrix at the 40-degree angle of motion. For each intensity sample, the nearest intensity in the data-matrix is found, resulting in a known position and angle, as can be seen in the figure.

An accuracy plot of all the experimental data of the intensities can also be made. This can be seen in Fig. 7.4b. The red line with the markers is the real distance that was measured with the digital calliper in section 5.3.1. In the figure, it can be clearly seen that when the low and high intensity levels are reached, the edge detection becomes inaccurate. The reason this happens is that the differences in intensities near the low and high intensity levels are very low. A small intensity difference can then lead to an error in the calculated position.

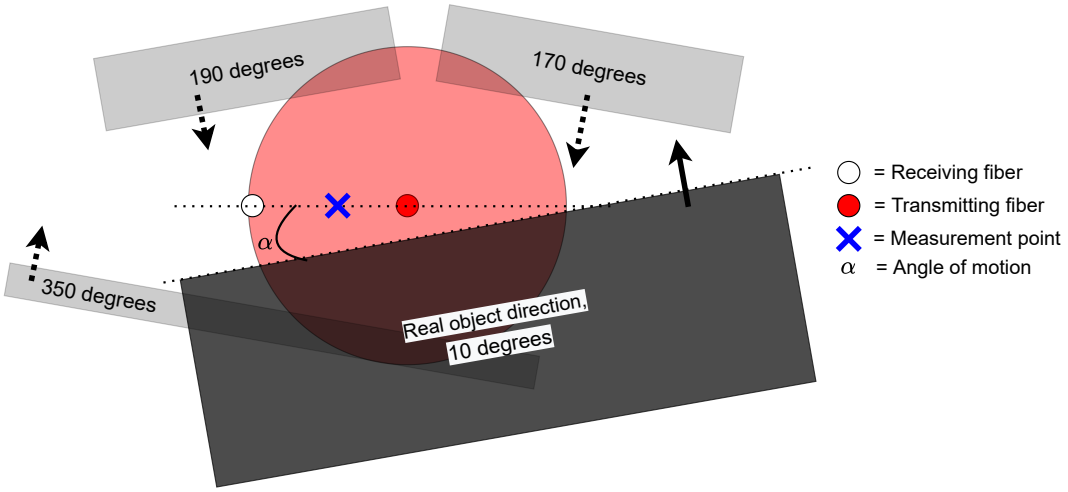

Figure 7.3: A schematic representation of the four possible outcomes when the real angle of motion is 10 degrees (big darker object). The three other possibilities for the angle of motion are drawn smaller for visibility.

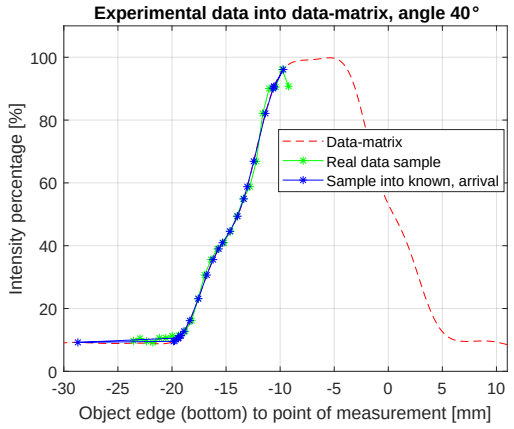

(a) Visualization of the experimental transmission data (green) as input in the data-matrix (red) for the 40-degree angle of motion. The result is the blue line.

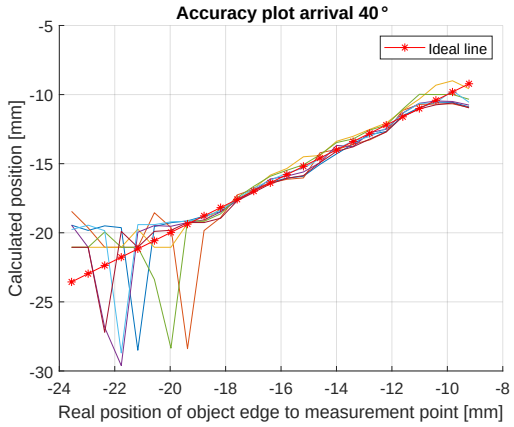

(b) Plot of all found positions, using the experimental transmissions, vs the real position. The red line is the ideal line.

Figure 7.4: Experimental data from section 6.4.1 is used as an input into the data-matrix from section 7.1.3. The resulting positions are compared in (b) with the actual position found in section 5.3.1.

A minimum and maximum intensity value can be set as a threshold. When an intensity value is below the minimum threshold, the edge of the object is out of reach of the receiving fiber. Similarly, when an intensity value above the maximum intensity is observed, the edge of the object is also out of reach of the receiving fiber. In Fig. 7.5a the same experimental data from Fig. 7.4a is used as input into the data-matrix. The threshold for the maximum intensity is set to the maximum intensity level minus three times the standard deviation of 3.7 in pixel intensity of all the experimental measurements. For the minimum intensity value, the threshold is set to the minimum intensity level plus three times the standard deviation of the experimental measurements. When these thresholds are reached, the calculated distance is set to a constant value, indicating the object is out of reach. These values are $-25mm$ when the intensity is below the minimum threshold and $-7.5mm$ when the intensity is above the maximum intensity threshold.

This also changes the accuracy plot from Fig. 7.4b to the plot seen in Fig. 7.5b. The number of points that can be differentiated, the measurement reach of he receiving fiber, will become less when the thresholds are set, however the overall accuracy increases. The algorithm for finding the positions is developed in MATLAB and can be found in Appendix A, MATLAB code A.3.

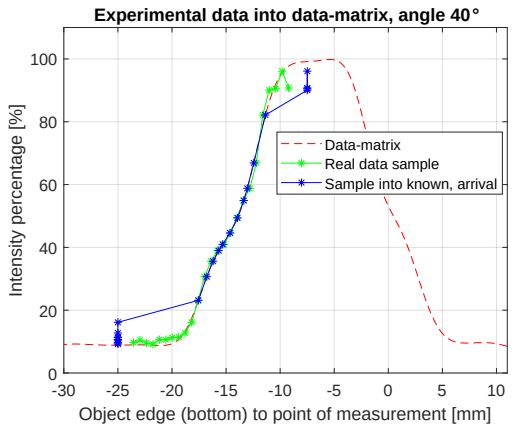

(a) The same situation as in Fig. 7.4a, but with the threshold values set.

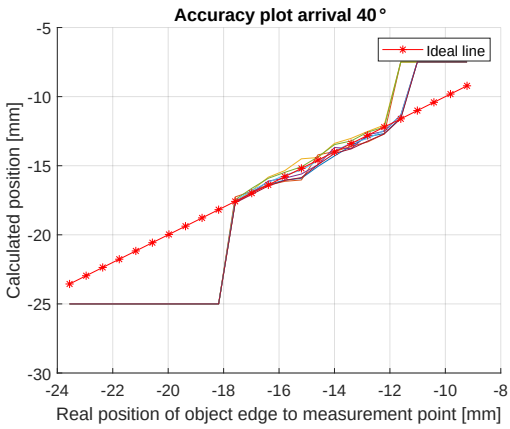

(b) The same situation as in Fig. 7.4b, but with the threshold values set.

Figure 7.5: To increase the accuracy of the edge detection system form Fig. 7.4, threshold values are set.

7.2.3. Accuracy in position

As was seen from Fig. 6.10 in the previous chapter, the transition trends between the two intensity levels depends on the angle of motion. Each angle of motion between 0 to 90 degrees has a unique transition, which is repeated three more times to form all 360 angles of motion. Only three receiving fibers, and thus only three angles of motion, were experimentally tested, so only three accuracy plots can be made of those angles of motion. In the previous section, the accuracy plot for the angle of motion of 40 degrees was already shown (Fig. 7.5b). In Fig. 7.7b and 7.6b the accuracy plots for 80 and 0 degrees are shown respectively, along with the visualization on how the position is calculated in Fig. 7.6a and 7.7a. The accuracy plots of the angles 0, 40 and 80 degrees are exactly the same as those of 180, 140 and 100 degrees respectively. The angles of motion of 220 and 320 degrees differ only slightly to that of 40 degrees, similarly, the angles of motion of 260 and 280 degrees differ only slightly to that of 80 degrees.

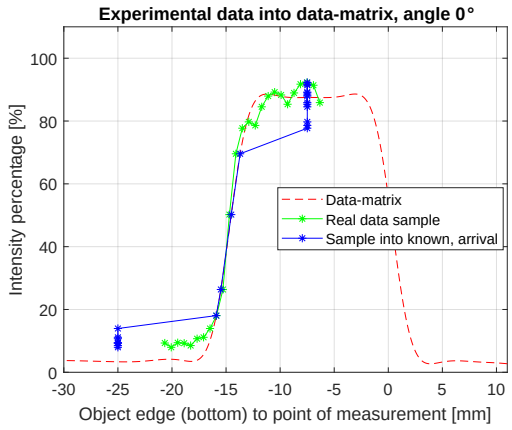

(a) Visualization of the experimental transmission data (green) as input in the data-matrix (red) for the 0-degree angle of motion. The result is the blue line. The found positions $-25mm$ and $-7.5mm$ indicate that the threshold values have been reached.

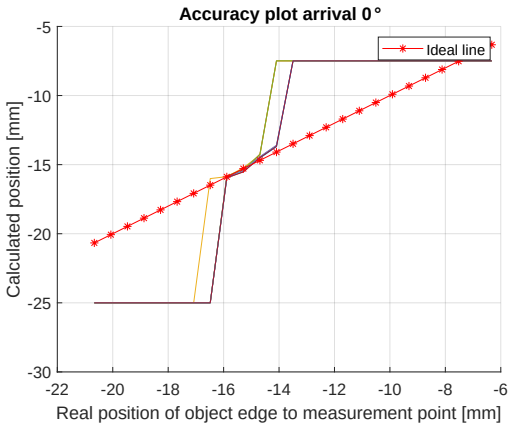

(b) Plot of all found positions, at the 0-degree angle of motion, using the experimental transmissions vs the real position. The red line is the ideal line.

Figure 7.6: The results of putting the experimental data of the 0-degree angle of motion into the inverse data-matrix.

As can be seen from the figures, the amount of data points that can be accurately traced back to a position (the measurement reach of an individual receiving fiber) depends on the steepness of the transition between the two intensity levels. For an angle of motion of 0 degrees, this transition is very steep and only four points can be accurately calculated, using the same threshold of three times the standard deviation, as in section 7.2.2. The transition at an angle of motion of 40 degrees is much more spread out and 11 positions can be accurately calculated.

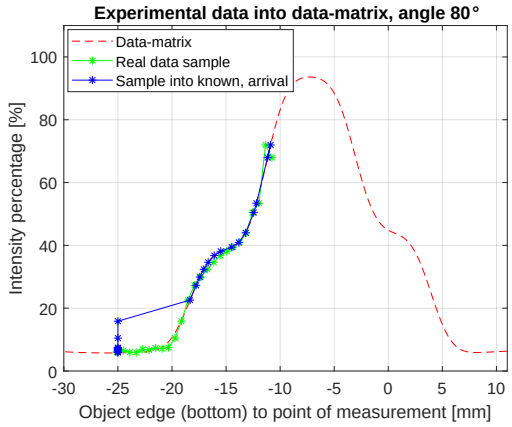

(a) Visualization of the experimental transmission data (green) as input in the data-matrix (red) for the 80-degree angle of motion. The result is the blue line. The found positions $-25mm$ indicate that the low threshold value has been reached.

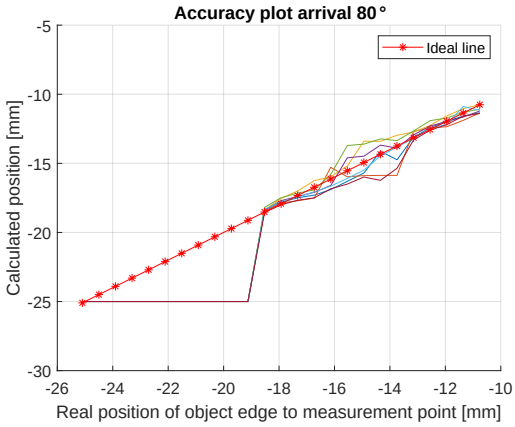

(b) Plot of all found positions, at the 80-degree angle of motion, using the experimental transmissions vs the real position. The red line is the ideal line.

Figure 7.7: The results of putting the experimental data of the 80-degree angle of motion into the inverse data-matrix.

The accuracy depends not only on the angle of motion but also on the position of the object. In Fig. 7.7b, it can be seen that at a position of $-15mm$ between the bottom object edge and the point of measurement the accuracy drops. In Fig. 7.7a at the same position of $-15mm$, there is a small segment where the increase in intensity is less. This is due to the large relative distance between the receiving and transmitting fibers, as seen from the edge of the object. At 0 degrees, both fibers are covered simultaneously and the relative distance is zero, but at an increased angle, the relative distance between the receiving and transmitting fibers increases. At 90 degrees, this distance is maximal, namely $9mm$, which follows from section 6.3.1. Decreasing the distance between the receiving and transmitting fibers would avoid this issue.

The minimum and maximum standard deviation for tested angles of motion can be seen in Table 7.1. The measurement reach of an individual receiving optical fiber is also given in the Table. It is calculated as the measurement reach within minimum and maximum intensity thresholds for each angle of motion of the object.

	Maximum standard deviation [mm]	Minimum standard deviation [mm]	Measurement reach [mm]
0-degree angle of motion	0.11	0.058	2.25
40-degree angle of motion	0.54	0.14	5.9
80-degree angle of motion	1.2	0.11	7.2

Table 7.1: The standard deviations of the calculated positions with the experimental data as input into the data matrix set up in section 7.1.3.

7.3. Multiple receiving fibers

In section 7.2.1, it was explained that the angle of motion of the object can not be determined with only the received signal from one receiving fiber. In this section, the signals of multiple fibers are combined so that the real angle of motion of the object can be determined.

Three receiving fibers are minimally needed to determine the angle of motion of the object. Two receiving fibers would be sufficient in most cases; however, if the angle of motion is either 0 or 180 degrees, both receiving fibers would be covered simultaneously, leading to two possible angles of motion. Another set of receiving and transmitting fibers could solve this, but in this thesis, only one set of receiving and transmitting fibers is investigated.

Two possible cases will be investigated: the case when three receiving fibers are positioned around the transmitting fiber and the case when four receiving fibers are positioned around the transmitting fiber.

7.3.1. Data fabrication

As shown in Fig. 5.4 from Chapter 5 and explained in section 6.4, due to the lack of space, only three receiving fibers could be placed within the range of 0 to 90 degrees. This does also mean that the experimental transmission data of only six angles of motion is known, namely 0, 40 and 80 degrees and due to the symmetry as explained in section 5.1.1, also that of 180, 140 and 100 degrees. If the transmission data is reversed, as also explained in section 5.1.1 and done in section 6.4.2, the experimental transmissions of 220, 240, 280 and 320 degrees would be received.

In the case when three receiving fibers are positioned around the transmitting fiber and the object moves from the bottom to the top, the experimental transmissions of 0, 120 and 240 degrees are needed as input for the inverse data-matrix from section 7.1.3. Similarly, when four receiving fibers are positioned around the transmitting fiber, the experimental transmissions of 0, 90, 180 and 270 degrees are needed, all assuming equal spacing of the receiving fibers. This does mean that the experimental transmission data of some of the angles of motion that are needed for these cases are not known.

To solve this issue, white noise has been added to the fitted surface from Fig. 7.1 to all angles of motion. This has been done twenty times, creating twenty different transmission datasets for all angles of motion. It is made sure that the added noise led to similar accuracy plots and has comparable standard deviations as seen in Table 7.1.

7.3.2. Three receiving fibers

As was explained in section 7.2.1, in most cases four possible angles of motion can be expected as output from one receiving fiber. The order in which each receiving fiber will start to observe intensity differences is used to determine the real angle of motion of the object. In this subsection, an example is given for the case when three receiving fibers surround one transmitting fiber. The receiving fibers are spaced 120 degrees apart, resulting in an equal spacing across the light spot. The placement of the receiving fibers around the light spot can be seen in Fig. 7.8.

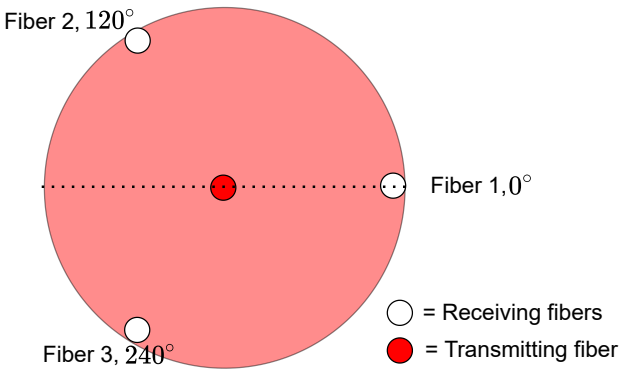

Figure 7.8: Schematic representation of the light spot created by the transmitting fiber in the centre. The three receiving fibers are spaced equally from each other, at 120 degrees apart. The number that each receiving fiber has been given can be seen in the figure.

The 0 degrees angle of motion is when the object is moving from the bottom to the top. The positive rotation of the angle of motion is counter-clockwise, so the 180-degree angle of motion is when the object is moving from the top to the bottom. The surface plot as seen in Fig. 7.1 is created with the receiving fiber at the base position, which is at the position of fiber 1, as was explained in section 5.1.1. The other two fibers, fiber 2 at 120 degrees and fiber 3 at 240 degrees will need to be shifted to the base position to get correct values

of position and angle of motion using the inverse data-matrix from section 7.1.3.

In Table 7.2, the shifting of each fiber to the base position can be seen. The global angle of motion is before any shifting of the angles, so with fiber 1 at the base position. To shift fiber 2 to the base position, the global angles need to be subtracted with 120 degrees, since fiber 2 is at 120 degrees, as can be seen in Fig. 7.8. Similarly, fiber 3 needs to be subtracted with 240 degrees. The resulting local angles of motion of the object for each fiber can be seen in the table, along with the corresponding global angle of motion of the object. The order in which each receiving fiber is covered by the object for the different angles of motion can be seen in the final column of the table.

	Fiber 1 at base position.	Fiber 2 at base position.	Fiber 3 at base position.	
Global angle of motion [degrees]	Local angle of motion [degrees]	Local angle of motion [degrees]	Local angle of motion [degrees]	Order of fiber
330 to 30	330 to 30	210 to 270	90 to 150	3→1→2
30 to 90	30 to 90	270 to 330	150 to 210	1→3→2
90 to 150	90 to 150	330 to 30	210 to 270	1→2→3
150 to 210	150 to 210	30 to 90	270 to 330	2→1→3
210 to 270	210 to 270	90 to 150	330 to 30	2→3→1
270 to 330	270 to 330	150 to 210	30 to 90	3→2→1

Table 7.2: Algorithm behind finding the real angle of motion of the object, in the case of three receiving fibers. The number of the fibers corresponds to its position as shown in Fig. 7.8. This table shows the general cases when the receiving fibers are not covered simultaneously by the edge of the object.

Table 7.2, contains the general cases, so when each receiving fiber is covered at a separate instance. There are also six cases in which two receiving fibers are covered simultaneously, these cases can be found in Table 7.3.

Global angle of motion [degrees]	Order of fiber
30	3 + 1→2
90	1→3 + 2
150	1 + 2→3
210	2→1 + 3
270	2 + 3→1
330	3→1 + 2

Table 7.3: Special cases in the algorithm, when two of the receiving fibers are covered simultaneously by the edge of the object.

Example situation, global angle of motion of 160 degrees
In Fig. 7.9, the situation for an angle of motion of 160 degrees can be seen. Fiber 2 is covered first, then fiber 1 and lastly fiber 3. With this specific order, looking at Table 7.2, it is already known that the real (global) angle of motion of the object lies between 150 to 210 degrees.

All receiving fibers measure the local angle of motion. Since fiber 2 is activated first, its signal will be also analysed first. The correct local angle of motion for fiber 2 would be 40 degrees (160 global angle - 120 shift). However, as explained in section 7.2.1, three other possible outputs of this specific angle of motion can also be received. These are 140, 220 and 320 degrees. All these angles can be filtered out knowing the order at which each receiving fiber is activated by the object, thus leaving out only the real local angle of motion of 40 degrees. The local angle of motion of the object can then be shifted back to the global angle of motion of the object knowing the angle of fiber 2 of 120 degrees, resulting in a global angle of motion of 160 degrees.

Fiber 1 will be activated after fiber 2 and since fiber 1 is already at the base position, no shifts are needed and the local angle of motion is equal to the global angle of motion. The correct output of fiber 1 would be 160 degrees. The three other possible outputs would be 20, 200 and 340 degrees. Using Table 7.2 again, it is

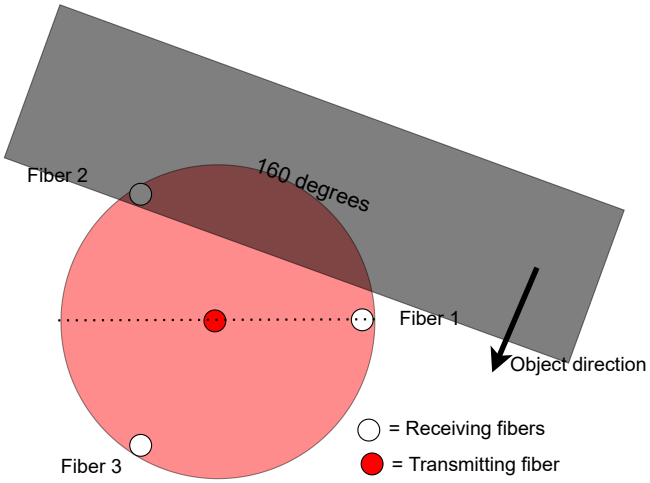

Figure 7.9: An example situation in the case three receiving fibers, for an angle of motion of 160 degrees. The order of the receiving fibers is, in this situation: 2, 1, 3.

known that the real angle of motion lies between 150 and 210 degrees. The angles of motion of 20 and 340 degrees can thus be filtered out. This does however still leaves two possible angles of motion: 160 and 200 degrees. The reason that besides the real angle of motion also another angle of motion is still possible, is because a line of symmetry is within the range of 150 to 210 degrees. As was explained in section 5.1.1, there are four lines of symmetry, at 0, 90, 180 and 270 degrees. When a line of symmetry is thus within a range as given in Table 7.2, it is possible that the real angle of motion of the object can not be filtered out for each specific fiber.

The real angle of motion of the object can still always be found since the first fiber that will be activated never has a local range of angles that has a line of symmetry in it.

7.3.3. Four receiving fibers

To avoid the problem of having a line of symmetry within a range of possible angles, as was the case with three receiving fibers around one transmitting fibers, four receiving fibers can be used. The four receiving fibers are spaced 90 degrees apart to get and equal spacing between them. With fiber 1 at the base position of 0 degrees, the other fibers are at 90, 180 and 270 degrees, as is schematically shown in Fig. 7.10. All receiving fibers are thus placed on a line of symmetry.

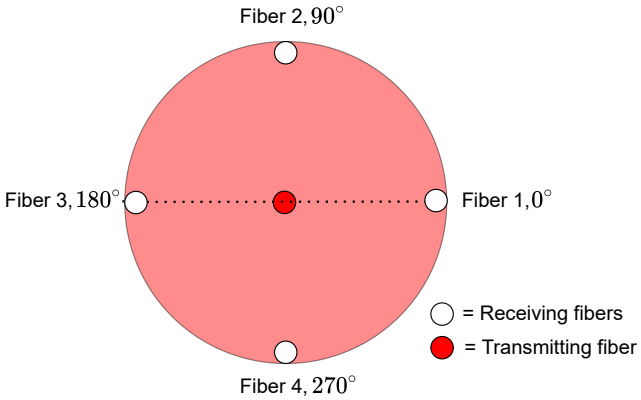

Figure 7.10: Schematic representation of the light spot created by the transmitting fiber in the centre. The four receiving fibers are spaced equally from each other, at 90 degrees apart. The number that each receiving fiber has been given can be seen in the figure.

The 0-degrees angle of motion and the positive rotation of the angle of motion of the object is the same as was described in the previous section for three receiving fibers. All the receiving fibers are again shifted to the base position to define the local angles of motion of the object. The local angle of motion of fiber 1 is again the same as the global angle of motion of the object. In Table 7.4 the shifting of each fiber to the base position can be seen, along with the global angle of motion and the order of activation of the fibers. Table 7.5 shows the eight special cases when two receiving fibers are activated simultaneously.

Global angle of motion [degrees]	Fiber 1 at base position. Local angle of motion [degrees]	Fiber 2 at base position. Local angle of motion [degrees]	Fiber 3 at base position. Local angle of motion [degrees]	Fiber 4 at base position. Local angle of motion [degrees]	Order of fiber
0 to 45	0 to 45	270 to 315	180 to 225	90 to 135	4→1→3→2
45 to 90	45 to 90	315 to 360	225 to 270	135 to 180	1→4→2→3
90 to 135	90 to 135	0 to 45	270 to 315	180 to 225	1→2→4→3
135 to 180	135 to 180	45 to 90	315 to 360	225 to 270	2→1→3→4
180 to 225	180 to 225	90 to 135	0 to 45	270 to 315	2→3→1→4
225 to 270	225 to 270	135 to 180	45 to 90	315 to 360	3→2→4→1
270 to 315	270 to 315	180 to 225	90 to 135	0 to 45	3→4→2→1
315 to 360	315 to 360	225 to 270	135 to 180	45 to 90	4→3→1→2

Table 7.4: Algorithm behind finding the real angle of motion of the object, in the case of four receiving fibers. The number of the fibers corresponds to its position as shown in Fig. 7.10. This table shows the general cases when the receiving fibers are not covered simultaneously by the edge of the object.

Angle of motion [degrees]	Order of fiber
0	4→3 + 1→2
45	4 + 1→2 + 3
90	1→2 + 4→3
135	1 + 2→3 + 4
180	2→1 + 3→4
225	2 + 3→1 + 4
270	3 + 4→1 + 2
315	4→1→3→9

Table 7.5: Special cases, when two of the receiving fibers are covered simultaneously by the edge of the object.

Example situation, global angle of motion of 160 degrees

The same example situation as from the case with three receiving fibers is done with four receiving fibers. The situation for an angle of motion of the object of 160 degrees can be seen in Fig. 7.11. In this case, fiber 2 is covered first, followed by fiber 1, 3 and lastly fiber 4. In Table 7.4 it can be found that in this situation, the real (global) angle of motion lies between 135 and 180 degrees.

The first activated fiber will again be analysed first, which is fiber 2 in this case. The correct local angle of motion for fiber 2 would be 70 degrees (160 global angle - 90 shift). The three other possible outputs are 110, 250 and 290 degrees. Using Table 7.4, it is known that the real local angle of motion for fiber 2 lies between 45 and 90 degrees. All of the wrong possible angles of motions are filtered out, leaving only the correct local angle of motion of the object at 70 degrees. The global angle of motion of the object can be found by shifting the local angle of motion of the object back to the global angle of motion, knowing the position of fiber 2 of 90 degrees. This gives the correct global angle of motion of the object of 160 degrees.

All the other receiving fibers would also lead to only the correct local angle of motion of the object, and thus the global angle of motion since no line of symmetry is within the ranges of angles as seen in Table. 7.4.

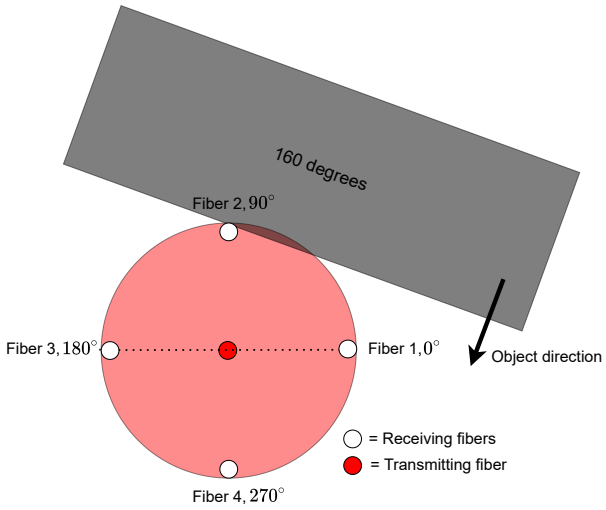

Figure 7.11: An example situation in the case four receiving fibers, for an angle of motion of 160 degrees. The order of the receiving fibers is, in this situation: 2, 1, 3, 4.

7.3.4. Accuracy in the angle of motion

With the fabricated experimental data from section 7.3.1 and the method for finding the real angle of motion out of four possible angles of motion, the accuracy of the sensor concept in determining the angle of motion can be calculated. A wrongly calculated angle can be identified by knowing at which quadrant the real angle is supposed to be. The four quadrants are separated by the lines of symmetry at 0, 90, 180 and 270 degrees, as was explained in section 5.1.1. If the real angle of motion would be 160 degrees and 203 is found, the angle is converted to its equivalent position in the correct quadrant, which would be 157 in the case of 203.

This is done for the twenty different datasets at various angles. In Fig. 7.12, the standard deviation can be seen for the various angles of motion of the object. It is found that near the lines of symmetry of 0, 90, 180 and 270 degrees, the accuracy is higher. The uncertainty increases after a symmetry point to decrease again when the next symmetry point is reached. The reason behind this is that at the lines of symmetry, the different transmission trend for each angle of motion are more distinguishable from each other. In the middle of the four segments, created by the lines of symmetry as seen in Fig. 7.12, the transition between each transmission trend line is smoother and thus less distinguishable.

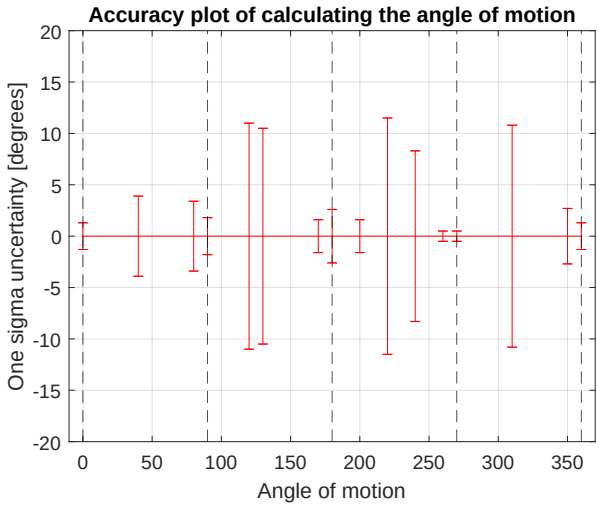

Figure 7.12: Accuracy plot for finding the correct angle of motion of the object. The lines of symmetry are indicated by the vertical dashed black lines. The one sigma uncertainty for finding various angles of motion of the object is indicated by the height of the red lines.

7.4. Conclusion

In this chapter, the final step is done of the experimental validation of using optical fibers combined with a diffuser as a method of tracking the edge of a moving object. An inverse data-matrix is set up of the continues dataset that resulted from the previous chapter. With this inverse data-matrix, any intensity level of a receiving fiber can be given as an input resulting in a distance of the object edge to the point of measurement for all angles of motion of the object. It is found that the measurement reach of the receiving fibers and the uncertainty in the measured positions of the object edge vary for the different angles of motion of the object. A sharp transition between the intensity levels limits the reach of the receiving fiber but increases the measurement accuracy. On the other hand, a smoother transition between the intensity levels allows for a greater reach of the receiving fiber, but at the cost of reducing the accuracy. The angle of motion of the object can be deduced by combining the transmission signals from multiple receiving fibers around one transmitting fiber. The order in which the receiving fibers are activated by the object is used as a filter to cross out the duplicate angles of motion of the object. The measurement reach of a single optical fiber with thresholds for the maximum and minimum intensity values set lies between $2.25mm$ and $7.2mm$, depending on the angle of motion of the object. The one-sigma uncertainty in the position of this experimental setup for the novel measurement concept lies between $0.06mm$ and $1.2mm$, also depending on the angle of motion of the object. The one-sigma uncertainty in the angle of motion of the object is on average 4.8 degrees across all angles.

8

Conclusion

In this thesis report, a concept for a design base for an edge detection sensor and tracking system with the use of optical fibers is designed and experimentally tested. The starting point of this thesis was a previous design concept made by a group of bachelor students [8]. Increasing the vision of the optical fibers that are used to guide and distribute the vision of a camera across the measurement plane would significantly increase the potential of their system. Increasing this vision of an optical fiber is set as the main goal of this thesis. This chapter presents the final conclusions of the work done in this thesis.

8.1. Theoretical analysis

Out of the literature research followed two possible approaches to achieve an increased vision of the optical fibers. One possibility was to make smart use of lenses to increase the numerical aperture of the optical fibers. The conclusions that followed from the theoretical analysis are the following:

- The vision of an optical fiber can be easily increased in various manners, for example by simply placing the optical fiber further away from the measurement plane.
- The vision of the optical fiber receiving the light (the receiving fiber) of a specific light source cannot be increased with the use of lenses and is limited to its own diameter.

8.2. Experimental validation

The other approach to achieve an increased vision of the optical fibers was to use light diffusers. A light diffuser spreads the light across its surface. If placed directly after a light source, it can act as an infinite number of light sources. This avoids the limitation that the vision of the receiving fiber of a light source is limited to its own diameter. The effect of a light diffuser on the vision of an optical fiber is experimentally tested.

The vision of the optical fiber is visualized by guiding light from a light source through the optical fiber. The area of the created light spot is increased by two orders of magnitude when placing a $2mm$ thick diffuser on top of the end of the optical fiber.

A second experimental setup showed that with the use of diffusers, the vision of an optical fiber is also increased. A discrete motion system with a step size of $0.60mm$ is successfully implemented to simulate a moving object in the measurement plane. The one-sigma uncertainty of this motion system is measured to be around $0.05mm$.

Different light intensity values are observed when an object is moving above the optical fiber. It is found that the intensity level has two constant levels: a low intensity level, indicating that the object is out of reach of the receiving optical fiber and a high intensity level indicating that the object is fully covering the receiving optical fiber. A transition between these intensity levels is also observed, which is an improvement over the past experimental setup without a light diffuser from the bachelor group that only observed the two intensity levels [8]. This indicates that the vision of the receiving fibers has been successfully increased.

The transition between the two intensity levels was found to be dependant on the distance between the light source and the receiving fiber. A large transition would allow for a clearer distinction between the intensity levels. An optimization is done to find the most optimal position of the receiving fiber, with the largest possible transition for a particular diffuser type. The optimal distance was found to be $9.2mm$. This distance is dependant on the size of the light spot, which is in turn dependant on the following factors:

- Type of diffuser.
- Intensity of the light source.
- In the case of using a duplicate optical fiber as the source of light, the coupling efficiency between the LED and the optical fiber.

The transition between the two intensity levels is also different for each angle of motion of the moving object if the object is rectangular. Besides tracking the object this also allows for determining the angle of motion of the object.

The one-sigma uncertainty in measuring the angle of motion of the object for this experimental design concept is found to be on average 4.8 degrees across all angles. The one-sigma uncertainty in measuring the distance of the object with respect to the constant measurement point is found to be anywhere between $0.06mm$ and $1.2mm$, depending on the angle of motion. The measurement reach of a single optical fiber with thresholds for the maximum and minimum intensity values set lies between $2.25mm$ and $7.2mm$, also depending on the angle of motion of the object. The factor of influence on the accuracy of the system is the steepness of the transition between the high and low intensity levels. A sharp rising or dropping transition increases the accuracy but decreases the vision of the optical fibers.

In conclusion, this research showed that light diffusers can be used to increase the measurement reach of optical fibers. Different intensity levels observed by the optical fiber can be successfully traced back to object position and object angle of motion.

9

Recommendations

This research is a follow up on previous research done by other students. The design concept for using optical fibers can be further improved. In this chapter, some recommendations are given to even further increase the potential of this sensor concept.

- Due to the COVID-pandemic at the time this research was done, most research had to be done at home. This is not ideal for building and experimenting with an experimental setup. The consequence of this is that the setup had to remain compact and portable and thus in this thesis only one building block of a receiving fiber and a light source has been investigated. To unlock the full potential of the sensor system, many building blocks can be combined. The separate results from each building block will increase the accuracy of the total sensor system.
- Another consequence of the compact design is the manual discrete motion system. The motion system itself proved to be quite accurate, but manually moving the object to the next position and taking a picture was a very tedious process to do. It also took a lot of time to perform all the measurements. This can be improved by integrating a continuous motion stage into the next experimental design for the sensor system.
- If a design is made out of multiple building blocks, it could be interesting to look into the combination of using different building blocks of a light source and receiving fiber. Higher accuracy can be achieved when the transition between the high and low intensity levels is steeper. It might be beneficial to integrate some building blocks where the measurement reach of the receiving fibers is lower but more accurate. This, combined with building blocks that have a larger measurement reach of the receiving fibers could provide both accurate measurements as well as a large sensing area of the optical fibers.
- In this thesis, the method used to find the real position and angle of motion of the object was by measuring in time the intensity signals of multiple receiving fibers. For a full-scale system made out of a large number of building blocks, the other method proposed in section 7.1.4 might be more suitable. Combining the intensity signals of multiple receiving fibers would also allow for live tracking of the motion of the object.
- In this thesis, the average of the experimental data has been fitted with a one-dimensional equation, followed by a two-dimensional interpolant fit. A more physical and better alternative would be to find and fit a suitable two-dimensional equation into the experimental data. This also allows better filtering of the measurement errors.
- The cameras used in this research are not the most ideal cameras. One camera suffered from significant noise and both cameras will need to be able to handle higher framerates to capture and track a fast-moving object.
- This research did not look into the integration of the sensor system into an air bearing. Some compromises might have to be made in both the sensor and actuator system to achieve an integrated contactless handler.

A

MATLAB codes

A.1. Algorithm for finding reference line

Listing A.1: Reference line finber

```
clear; close all;

%Loading in the desired picture
projectdir = 'C:\Users\TUDelft SID\Documents\MATLAB\Master\Thesis\Fotos\Setup ...
    3\Referentie metingen';
affectivepictures = dir( fullfile(projectdir, 'Measurement071020_exp5_5_move*.tif'));
sortedaffectivepictures=natsortfiles({affectivepictures.name});
filenames = fullfile( projectdir, sortedaffectivepictures);
numFiles = length(filenames);

%Loading in the correction matrix for the image distortion
load('C:\Users\TUDelft SID\Documents\MATLAB\Master\Thesis\Data points\cameraParams.mat')

%Correcting the offcentre of the image: using found values from script
rowsToShift = 16;
columnsToShift = 53;

vertical_offset = 155;      %offset where measurements and recognition takes place;
for K = 1 : numFiles
J = imread(filenames{K});
[Offcenter,newOrigin] = undistortImage(J,cameraParams);
I = circshift(Offcenter, [rowsToShift columnsToShift]);

%vertical line
x = [size(I,2)/2-vertical_offset size(I,2)/2-vertical_offset]; %left to right
y = [0 size(I,1)];
c = improfile(I,x,y);

%     Calling the functions
[edge_calibrator(K), index_min(K)] = Finder_calibrator(c);
[LineValue(K), LinePixel(K)] = Finder_calibrationLine(c);
end

%The developed algorithm for finding the pixelposition of the reference line
function [LineValue, LinePixel] = Finder_calibrationLine(c)

red_diff = c(1:1081,1,1);
green_diff = c(1:1081,1,2);

starting_point = 780;
ending_point = 847;
green_diff(1:starting_point)=NaN; %the first part of the picture is always rising, so ...
    ignore that part
green_diff(ending_point:1081)=NaN;

```

```
%calculate difference between one point and another 10 further
interval = 3; %interval between the points

for L = 1+interval:length(red_diff)-interval %do not start at one, because of the ...
    interval
Diff_difference(L) = green_diff(L)-green_diff(L-interval);
Diff_difference_tol3(L) = green_diff(L)-green_diff(L-interval+1);
Diff_difference_tol4(L) = green_diff(L)-green_diff(L-interval+2);
end

[Peak(1),index(1)] = max(Diff_difference);  % [difference, index in original vector]
[Peak(2),index(2)] = max(Diff_difference_tol3);
[Peak(3),index(3)] = max(Diff_difference_tol4);

[edge_calibrator, index_tussen] = max(Peak);
index_max = index(index_tussen);
LineValue = edge_calibrator;
LinePixel = index_max;
end
```

A.2. Algorithm for finding the pixel location of the moving object

Listing A.2: Moving object finder

```
clear; close all;

%Loading in the desired picture
projectdir = 'C:\Users\TUDelft SID\Documents\MATLAB\Master\Thesis\Fotos\Setup ...
    3\Referentie metingen';
affectivepictures = dir( fullfile(projectdir, 'Measurement071020_exp5_5_move*.tif'));
sortedaffectivepictures=natsortfiles({affectivepictures.name});
filenames = fullfile( projectdir, sortedaffectivepictures);
numFiles = length(filenames);

%Loading in the correction matrix for the image distortion
load('C:\Users\TUDelft SID\Documents\MATLAB\Master\Thesis\Data points\cameraParams.mat')

%Correcting the offcentre of the image: using found values from script
rowsToShift = 16;
columnsToShift = 53;

vertical_offset = 155;      %offset where measurements and recognition takes place;
for K = 1 : numFiles
J = imread(filenames{K});
[Offcenter,newOrigin] = undistortImage(J,cameraParams);
I = circshift(Offcenter, [rowsToShift columnsToShift]);

%Vertical line
x = [size(I,2)/2-vertical_offset size(I,2)/2-vertical_offset]; %left to right
y = [0 size(I,1)];
c = improfile(I,x,y);

%Calling the functions
[edge_calibrator(K), index_min(K)] = Finder_calibrator(c);
[LineValue(K), LinePixel(K)] = Finder_calibrationLine(c);
end


function [edge_calibrator, index_min] = Finder_calibrator(c)

red_diff = c(1:1081,1,1);
green_diff = c(1:1081,1,2);

starting_point = 180;
ending_point = 780;
scratch = 623:625;  %scratch in measurements 7 and 8 causes wrong readout
scratch2 = 711:715;  %scratch in measurements 7 and 8 causes wrong readout
scratch3 = 760:769;  %scratch in measurements 7 and 8 causes wrong readout
```

```
sunlight = 448:450; %picture 6 in measurement 8 suffered from direct sunrays
green_diff(1:starting_point)=NaN; %the first part of the picture is always rising, so ...
    ignore that part
green_diff(ending_point:1081)=NaN;
green_diff(scratch)=NaN;
green_diff(scratch2)=NaN;
green_diff(scratch3)=NaN;
green_diff(sunlight)=NaN;

%Calculate difference between one point and another 10 further
interval = 3; %interval between the points

for L = 1+interval:length(red_diff)-interval %do not start at one, because of the ...
    interval
Diff_difference(L) = green_diff(L)-green_diff(L-interval);
Diff_difference_tol3(L) = green_diff(L)-green_diff(L-interval+1);
Diff_difference_tol4(L) = green_diff(L)-green_diff(L-interval+2);
end

[Peak(1),index(1)] = max(Diff_difference);  % [difference, index in original vector]
[Peak(2),index(2)] = max(Diff_difference_tol3);
[Peak(3),index(3)] = max(Diff_difference_tol4);

[edge_calibrator, index_tussen] = max(Peak);
index_max = index(index_tussen);

%check to counter the effects of seeing the side of the slider
%%
tolerance = 15;
check2 = green_diff(index_max-tolerance:index_max);

tolerance2 = 4; %tolerance to find new minimum value near second peak

counter = 0;
difference_check = diff(check2);
for p = 1:length(difference_check)
if difference_check(p)≥50
counter = counter+1;
if (p-tolerance2)≤0
[antiPeak(counter),index_between(counter)] = min(check2(1:p));
index_check(counter) = p-tolerance2+index_between(counter)-1;
index_min_a(counter) = index_max-(tolerance-index_check(counter)+1);
else
[antiPeak(counter),index_between(counter)] = min(check2(p-tolerance2:p));
index_check(counter) = p-tolerance2+index_between(counter)-1;
index_min_a(counter) = index_max-(tolerance-index_check(counter)+1);
end
break
end
end

if counter≥1
index_min = index_min_a(1);
else
index_min = index_max;
end

end
```

A.3. Using inverse data-matrix

Listing A.3: Object position and angle finder

```
%Calculations with smoothed fit;
clear; close all

%Load in data from images and fits
directory = 'C:\Users\TUDelft SID\Documents\MATLAB\Master\Thesis\New reflectance data\';

%Correct zero point object edge
load(fullfile(directory,'Dataset_Experimental_doubleFIT_Symmetric360.mat'))      ...
    %Double fitted data, symmetric 360 full angles 4501 length

%Other data
load(fullfile(directory,'data_full_experimentEXP.mat'))         %Average data from ...
    the experiment
load(fullfile(directory,'data_unavg_experimentFirst.mat'))      %All data from the ...
    experiment
load(fullfile(directory,'data_unavg_experimentFirstCorrected.mat'))      %All data ...
    from the experiment, Corrected
load(fullfile(directory,'data_unavg_experimentLast.mat'))       %All data from the ...
    experiment
load(fullfile(directory,'offset_experiFirst.mat'))              %All data from the ...
    experiment, offsets

%Data experimentation
datasetnu = Dataset_Experimental_doubleFIT_Symmetric360;   %older 180 degree surface
datasetnu = datasetnu(:,1:181); %Half size dataset
datasetnuCirkel = Dataset_Experimental_doubleFIT_Symmetric360;

datasetnufirst = data_unavg_experimentFirstCorrected-offset_experiFirst;
datasetnulast = (data_unavg_experimentLast(:,:,[1 3:end]));

%Vectors for plotting
y_move = ones(4501,361);
y_move(:,1) = 15:-0.01:-30; %movement
y_move = y_move(:,1).*y_move(:,2:end);
y_move = [y_move y_move(:,1)];

x_angle = ones(4501,361);
x_angle(1,:) = 0:1:360; %hoek angle
x_angle = (x_angle(1,:)'.*x_angle(2:end,:)')';
x_angle = [x_angle; x_angle(1,:)];

%Set numbers for covered and not covered
[a, end_end] = min(abs(y_move(:,1)-(-25)));    %choose end points for the mean and ...
    find index
[a2, end_first] = min(abs(y_move(:,1)-(14)));
[a3, highestend] = min(abs(y_move(:,1)-(-9)));
[a4, highestfirst] = min(abs(y_move(:,1)-(-5)));
middlepoint = 2250;

CoveredFit = mean(datasetnu(highestfirst:highestend,:));
NotCoveredLastFit = mean(datasetnu(end_end:end,:));
NotCoveredFirstFit = mean(datasetnu(1:end_first,:));
DifferenceFit = CoveredFit-NotCoveredLastFit; %Difference between coverend and not ...
    covered
DifferenceFirstFit = CoveredFit-NotCoveredFirstFit; %Difference between coverend and ...
    not covered

maxcovered = min(CoveredFit);
maxnotcovered = max([NotCoveredLastFit' NotCoveredFirstFit']);
Margin = 1.1;  %added margin for covered or notcovered findings for all angles
maxcovered = maxcovered/Margin;
maxnotcovered = max(maxnotcovered)*Margin;

%Set vectors for plotting surface plot
movementxreff = -7.6400:0.5975:30.6;   %mm; distance reference to object
```

```
ref2center = 14.25-2.2/2-0.25/2;              %mm; line to outer center - width ...
    center - width ref lie
movementxfull = movementxreff-ref2center;     %mm; distance object to edge

angleFullEXP = [180:(-40):90 (80):-(40):0];   % Angular steps
angleFullEXPvarying = ones(size(movementxfull,2),size(angleFullEXP,2)).*angleFullEXP;
angleFullEXPvaryingCirkel = [fliplr(angleFullEXPvarying) ...
    fliplr(angleFullEXPvarying)+180];

moveAngle = 4.5*ones(size(movementxreff,2),1).*sind(angleFullEXP);
movementxvaryingEXP = movementxfull'.*ones(length(movementxfull),size(moveAngle,2)) - ...
    moveAngle;

%%%% Finding symmetry point For Correction (only if using half dataset)%%%%
drop = 40;  % percentage point of fully covered per angle
pointdrop = DifferenceFit*drop/100;
point = ones(size(CoveredFit)).*120;

valuesdiffREXP = zeros(size(point)); positionsEnteringEXP = zeros(size(point));
valuesdiffEXP = zeros(size(point)); positionsLeavingEXP = zeros(size(point));
valuesdiffREXPCirk = zeros(size(point)); positionsEnteringEXPCirk = zeros(size(point));
valuesdiffEXPCirk = zeros(size(point)); positionsLeavingEXPCirk = zeros(size(point));
for L = 1:length(point) %angles 0 40 and 80
    [valuesdiffREXP(L), positionsEnteringEXP(L)] = ...
        min(abs(point(L)-datasetnuCirkel(1:2250,L)'));
    [valuesdiffEXP(L), positionsLeavingEXP(L)] = ...
        min(abs(point(L)-datasetnuCirkel(2250:end,L)'));
    [valuesdiffREXPCirk(L), positionsEnteringEXPCirk(L)] = ...
        min(abs(point(L)-datasetnuCirkel(1:2250,180+L)'));
    [valuesdiffEXPCirk(L), positionsLeavingEXPCirk(L)] = ...
        min(abs(point(L)-datasetnuCirkel(2250:end,180+L)'));
end

positionsLeavingfullEXP = positionsLeavingEXP+2250;
positionsLeavingfullEXPCirk = positionsLeavingEXPCirk+2250;
middleEXP = round(positionsEnteringEXP + ...
    (positionsLeavingfullEXP-positionsEnteringEXP)/2);
middleEXPCirk = round(positionsEnteringEXPCirk + ...
    (positionsLeavingfullEXPCirk-positionsEnteringEXPCirk)/2);
tussenstap = y_move(:,1:181);
middle_mmEXP = tussenstap(middleEXP);
middle_mmMeanEXP = mean(middle_mmEXP(1,:));
tussenstap2 = y_move(:,181:end);
middle_mmEXPCirk = tussenstap2(middleEXPCirk);
middle_mmMeanEXPCirk = mean(middle_mmEXPCirk(1,:));

linksEXP = tussenstap(positionsEnteringEXP);
rechtsEXP = tussenstap(positionsLeavingfullEXP);
linksEXPCirk = tussenstap2(positionsEnteringEXPCirk);
rechtsEXPCirk = tussenstap2(positionsLeavingfullEXPCirk);

%Create dataset from zero to 100% for displaying
minim = min(datasetnuCirkel(:));
newset = datasetnuCirkel-minim;
maximaal = max(newset(:));
keer = 100/maximaal;
newset0_100 = newset.*keer;

h = figure;
surf(x_angle(1:20:end,:), y_move(1:20:end,:), newset0_100(1:20:end,:)); shading interp
colormap(jet(50)); colorbar
grid on; zlim([0 100]); hold on
xlabel('Angle of motion [degree]'); ylabel('Object edge (bottom) to point of ...
    measurement [mm]');
zlabel('Intensity percentage [%]')
set(gca,'FontSize',12,'FontWeight','demi')
title('Extrapolated fit of individual angles', 'FontSize', 14,'Interpreter', 'none');

%%%%Lines of constant intensity and middle position
plot3(x_angle(1:20:end,1:181), middle_mmEXP, ones(181,1).*240,'w*-', 'LineWidth', 3)
```

```
117 plot3(x_angle(1:20:end,181:end), middle_mmEXPCirk, ones(181,1).*240,'w*-', ...
        'LineWidth', 3)    %above 180 degs
118 plot3(x_angle(1:20:end,1:181), ones(181,1)*middle_mmMeanEXP, ones(181,1)*240,'c*-', ...
        'LineWidth', 3)
119 plot3(x_angle(1:20:end,181:end), ones(181,1)*middle_mmMeanEXPCirk, ...
        ones(181,1)*240,'c*-', 'LineWidth', 3)
120 plot3(x_angle(1:20:end,1:181), rechtsEXP, ones(181,1).*240,'w*-', 'LineWidth', 3)
121 plot3(x_angle(1:20:end,1:181), linksEXP, ones(181,1).*240,'w*-', 'LineWidth', 3)
122 plot3(x_angle(1:20:end,181:end), rechtsEXPCirk, ones(181,1).*240,'w*-', 'LineWidth', 3)
123 plot3(x_angle(1:20:end,181:end), linksEXPCirk, ones(181,1).*240,'w*-', 'LineWidth', 3)
124 view(2); zlim([0 255])
125
126 %% Algorithm for finding position and angle
127
128 %%%%% Choose desired data points here %%%%%
129 hoek = 3;   %1-2-3:: 0-40-80 degrees.
130 First_or_Last = 1;  %First part
131 plotss = 1;   %Plot visable fit
132 % plotss = 2;   %Plot accuracy
133 % plotss = 0;   %No plot
134 Fiber_amount = 1; Fiber_difference = 360/Fiber_amount;  %If multiple fibers: plot not ...
        accurate
135 beginpoint = 1;  endpoint = 25; endpointlast = 40;
136 rng(2^32-2)
137 noiselevel = 0.01; SNRlevel = 10;
138
139 %Add noise to simulate multiple measurements
140 out = cat(3,awgn(datasetnuCirkel,noiselevel,SNRlevel), ...
        awgn(datasetnuCirkel,noiselevel,SNRlevel), ...
        awgn(datasetnuCirkel,noiselevel,SNRlevel), ...
        awgn(datasetnuCirkel,noiselevel,SNRlevel), ...
        awgn(datasetnuCirkel,noiselevel,SNRlevel), ...
        awgn(datasetnuCirkel,noiselevel,SNRlevel), ...
        awgn(datasetnuCirkel,noiselevel,SNRlevel), ...
        awgn(datasetnuCirkel,noiselevel,SNRlevel), ...
        awgn(datasetnuCirkel,noiselevel,SNRlevel), ...
        awgn(datasetnuCirkel,noiselevel,SNRlevel), ...
        awgn(datasetnuCirkel,noiselevel,SNRlevel), ...
        awgn(datasetnuCirkel,noiselevel,SNRlevel), ...
        awgn(datasetnuCirkel,noiselevel,SNRlevel), ...
        awgn(datasetnuCirkel,noiselevel,SNRlevel), ...
        awgn(datasetnuCirkel,noiselevel,SNRlevel), ...
        awgn(datasetnuCirkel,noiselevel,SNRlevel), ...
        awgn(datasetnuCirkel,noiselevel,SNRlevel), ...
        awgn(datasetnuCirkel,noiselevel,SNRlevel), ...
        awgn(datasetnuCirkel,noiselevel,SNRlevel), ...
        awgn(datasetnuCirkel,noiselevel,SNRlevel), ...
        awgn(datasetnuCirkel,noiselevel,SNRlevel));
141 beginpointnew = 1; endpointnew = 2250; middle = 2100;
142 % skip = (endpointnew-beginpointnew)/25;
143 skip = 15;  %not all datapoints, since would take too long
144 %%%%%%%%%%%%%%%%%%%%%%%%%%%%%%%%%%%%%%%%%%%%%
145
146 errormargin = 3.2*3.8; %Error of one SD from experimental values
147
148 Approach_angles = zeros(1,Fiber_amount);
149 if First_or_Last==1 %First part, loops are the same, dataset is different
150     hoeknumber = (hoek-1)*40+1;  %Angle
151 %     getalfull = zeros((endpointnew)/skip,Fiber_amount);     %If start at index 1; ...
        created data
152     getalfull = zeros(endpoint,Fiber_amount);         %Real data
153
154 %Setting up matrix for RAM saving: only for if choosing created data
155 %     indexFirst = zeros(size(getalfull,1),361); DifferFirst = ...
        zeros(size(getalfull,1),361);
156 %     indexLast = zeros(size(indexFirst));       DifferLast  = ...
        zeros(size(getalfull,1),361);
157 %     Current_angle = zeros(1,size(out,3));
158 %     foundangle_Total = zeros(size(out,3),Fiber_amount);
159 %     foundangle_Entering_FirstSteps = zeros(size(out,3),Fiber_amount);
160 %     foundangle_Leaving_FirstSteps = zeros(size(out,3),Fiber_amount);
161
```

```
    for groteloop = 1:size(datasetnufirst,3)    %Real data
%     for groteloop = 1:size(out,3)    %Created data
        datanummer = groteloop;
        for Fiber = 1:Fiber_amount
            Approach_angles(Fiber) = hoeknumber+Fiber_difference*(Fiber-1);
            getalfull(:,Fiber) = datasetnufirst(beginpoint:endpoint,hoek,datanummer); ...
                %Real data
             %Created data::
% getalfull(:,Fiber) = ...
%     ...
    out(beginpointnew:skip:endpointnew,hoeknumber+Fiber_difference*(Fiber-1),datanummer);

            location_Entering_edge = zeros(length(getalfull(:,Fiber)),size(out,2));
            location_Leaving_edge = zeros(length(getalfull(:,Fiber)),size(out,2));
            for getalstap = 1:length(getalfull(:,Fiber))
                getal = getalfull(getalstap,Fiber);
                if abs(getal-CoveredFit(hoeknumber))<errormargin
                    indexFirst(getalstap,:) =  middlepoint;
                    indexLast(getalstap,:) =  middlepoint;
                    location_Entering_edge(getalstap,:) = ...
                        y_move(indexFirst(getalstap,:),1);
                    location_Leaving_edge(getalstap,:) = ...
                        y_move(indexLast(getalstap,:),1);
                elseif (getal-NotCoveredFirstFit(hoeknumber))<errormargin
                    indexFirst(getalstap,:) =  end_first;
                    indexLast(getalstap,:) =  end_end;
                    location_Entering_edge(getalstap,:) = ...
                        y_move(indexFirst(getalstap,:),1);
                    location_Leaving_edge(getalstap,:) = ...
                        y_move(indexLast(getalstap,:),1);
                else
                    for hoekenn = 0:1:size(out,2)-1
                        [DifferFirst(getalstap,hoekenn+1), ...
                            indexFirst(getalstap,hoekenn+1)] = ...
                            min(abs(datasetnuCirkel(1:highestfirst,hoekenn+1)-getal));
                        [DifferLast(getalstap,hoekenn+1), ...
                            indexLast(getalstap,hoekenn+1)] = ...
                            min(abs(datasetnuCirkel(highestend:end,hoekenn+1)-getal));
                    end
                    location_Entering_edge(getalstap,:) = ...
                        y_move(indexFirst(getalstap,:),1);
                    location_Leaving_edge(getalstap,:) = ...
                        y_move(indexLast(getalstap,:)+highestend-1,1);
                end
            end

            %Choosing angle with minimal difference
            check = [0 40 80]+1; %check for experimental average
            Current_angle(groteloop) = check(hoek);

%%%%%%%Finding the angle of motion; only for the created data%%%%%%%%
%             findingAngleTotal =...
%                 sum(abs([location_Entering_edge(1:round(length(getalfull)/2)-1,:); ...
%                 location_Leaving_edge(round(length(getalfull)/2):end,:)]-...
%                 y_move(beginpointnew:skip:endpointnew, Approach_angles(Fiber))));
%             findingAngleEnteringFirst = ...
    sum(abs(location_Entering_edge-y_move(beginpointnew:skip:endpointnew, ...
    Approach_angles(Fiber))));
%             findingAngleLeavingFirst = ...
    sum(abs(location_Leaving_edge-y_move(beginpointnew:skip:endpointnew, ...
    Approach_angles(Fiber))));
%
% %             Calculate differente between found range of points and all known ...
    points for each angle of motion --> the minimum value of
% %             this difference is the found angle of motion
%             findingAngleTotal = ...
%                 sum(abs([location_Entering_edge(1:round(length(getalfull)/2)-1,:); ...
%                 location_Leaving_edge(round(length(getalfull)/2):end,:)]-...
%                 y_move(beginpointnew:skip:endpointnew, :)));
%             findingAngleEnteringFirst = ...
    sum(abs(location_Entering_edge-(y_move(beginpointnew:skip:endpointnew, :))));
```

```
215 %             findingAngleLeavingFirst = ...
        sum(abs(location_Leaving_edge-flipud(y_move(beginpointnew:skip:endpointnew, :))));
216 %
217 %             [¬, foundangle_Total(groteloop,Fiber)] = min(findingAngleTotal);
218 %             [¬, foundangle_Entering_FirstSteps(groteloop,Fiber)] = ...
        min(findingAngleEnteringFirst);
219 %             [¬, foundangle_Leaving_FirstSteps(groteloop,Fiber)] = ...
        min(findingAngleLeavingFirst);
220 %
221         end
222
223        %Plots; uncomment and comment some lines when using the created data
224         if plotss == 1
225             figure;
226             plot(y_move(:,hoeknumber), datasetnu(:,hoeknumber),  'r--')
227             hold on; grid on; ylim([0 255])
228             plot(movementxvaryingEXP(beginpointnew:endpoint, hoek), ...
                    datasetnufirst(beginpointnew:endpoint,hoek, datanummer), 'g*-')
229             plot(location_Leaving_edge(:,hoeknumber), ...
                    getalfull(beginpointnew:endpoint), 'b*-')
230             title(['Experimental data into data-matrix, angle ' ...
                    num2str(Current_angle(groteloop)-1) '\circ'])
231             ylabel('Intensity percentage [%]');
232             xlabel('Object edge (bottom) to point of measurement [mm]');
233             set(gca,'FontSize',12,'FontWeight','demi')
234             legend('Data-matrix', 'Real sample data', 'Sample into known, arrival', ...
                    'Sample into known, leaving')
235         elseif plotss == 2
236 %             p2(groteloop) = plot(y_move(beginpointnew:skip:endpointnew, ...
        hoeknumber), location_Entering_edge(:,hoeknumber)); %Created data
237             hold on; grid on
238             plot(movementxvaryingEXP(beginpoint:endpoint, hoek), ...
                    location_Leaving_edge(:,hoeknumber))  %Real data
239             title(['Accuracy plot arrival ' num2str(Current_angle(groteloop)-1) '\circ'])
240             xlabel('Real position of object edge to measurement point [mm]'); ...
                    ylabel('Calculated position [mm]')
241             set(gca,'FontSize',12,'FontWeight','demi'); ylim([-30 -5])
242         end
243
244 %         sdcalc(:,groteloop) = location_Leaving_edge(:,check(hoek));   %Calculating ...
        standard deviations
245     end
246
247     if plotss == 2
248         pideal = plot(movementxvaryingEXP(beginpoint:  endpoint,hoek), ...
                movementxvaryingEXP(beginpoint:endpoint, hoek), 'r*-');     %Firstpart
249 %         pideal = plot(movementxvaryingEXP(beginpoint:  end,hoek), ...
        movementxvaryingEXP(beginpoint:end, hoek), 'r*-');     %Full
250 %         legend(p2 );
251         legend(pideal,'Ideal line')
252     end
253
254 end
```

Bibliography

[1] International technology roadmap for photovoltaic - 2016 results, 2017. Eighth edition.

[2] International technology roadmap for photovoltaic - 2018 results, 2019. Tenth edition.

[3] Andrew A. Berlin, David Biegelsen, Patrick C. F. Cheung, Markus P. J. Fromherz, David Goldberg, Warren G. Jackson, Bryan Preas, James E. Reich, and Lars-Erik Swartz. Motion control of planar objects using large-area arrays of mems-like distributed manipulators. 2000.

[4] Andrea M. Brown, Daniel V. Hahn, David M. Brown, Nathan W. Rolander, Chun-Huei Bair, and Joseph E. Sluz. Experimental implementation of fiber optic bundle array wide fov free space optical communications receiver. *Appl. Opt.*, 51(18):3995–4002, Jun 2012. doi: 10.1364/AO.51.003995. URL `http://ao.osa.org/abstract.cfm?URI=ao-51-18-3995`.

[5] Xavier F. Brun and Shreyes N. Melkote. Analysis of stresses and breakage of crystalline silicon wafers during handling and transport. *Solar Energy Materials and Solar Cells*, 93(8):1238 – 1247, 2009. ISSN 0927-0248. doi: https://doi.org/10.1016/j.solmat.2009.01.016. URL `http://www.sciencedirect.com/science/article/pii/S0927024809000324`.

[6] Stephen Carey, D. Martin Knotter, Eric Ooms, Johannes Boersma, Elfried van der Sar, Robbert Cop, Wim Gerritzen, Hans van Zadelhoff, and Henk Bouma. Yield impact of backside metal-ion contamination. In *Ultra Clean Processing of Semiconductor Surfaces X*, volume 187 of *Solid State Phenomena*, pages 287–290. Trans Tech Publications Ltd, 5 2012. doi: 10.4028/www.scientific.net/SSP.187.287.

[7] Curbell Plastics. Led lighting and diffusion solutions, (n.d.). URL `https://www.curbellplastics.com/Research-Solutions/Industry-Solutions/Markets/Lighting`. [Online; accessed 15-December-2020].

[8] J.F. Elfferich, F.J. van Melis, T. Neeft, and A.P. Tiktak. The simulation and design of a one-sided distributed optical sensor for wafer tracking, 2019. [Bachelor's thesis].

[9] FiberFin . Pof finishing tools, (n.d.). URL `https://fiberfin.com/product-category/hand-tools/pof-finishing-tools/`. [Online; accessed 21-January-2021].

[10] Takehiro Fukushima. Optical fiber multiplexer using a single grin-rod lens and a planar microlens array. In A. G. Mignani and H. C. Lefèvre, editors, *Fourteenth International Conference on Optical Fiber Sensors*, volume 4185, pages 271 – 274. International Society for Optics and Photonics, SPIE, 2000. doi: 10.1117/12.2302204. URL `https://doi.org/10.1117/12.2302204`.

[11] Daniel V. Hahn, David M. Brown, Nathan W. Rolander, Joseph E. Sluz, and Radha Venkat. Fiber optic bundle array wide field-of-view optical receiver for free space optical communications. *Opt. Lett.*, 35(21):3559–3561, Nov 2010. doi: 10.1364/OL.35.003559. URL `http://ol.osa.org/abstract.cfm?URI=ol-35-21-3559`.

[12] Daniela Hahn, David Brown, Andrea Brown, C.-H Bair, Mark Mayr, N.M. Rolander, Joseph Sluz, and Radha Venkat. Conformal free-space optical communications terminal designs for highly confined vehicles. *Johns Hopkins APL Technical Digest (Applied Physics Laboratory)*, 30:321–330, 01 2012.

[13] S. Harrison, O. Nos, A. Danel, D. Muñoz, J.P. Rakotoniaina, J. Gaume, C. Roux, and P.J. Ribeyron. How to deal with thin wafers in a heterojunction solar cells industrial pilot line: First analysis of the integration of cells down to 70µm thick in production mode. In *2011 37th IEEE Photovoltaic Specialists Conference*, pages 358–362, 2016. doi: 10.4229/EUPVSEC20162016-2BO.9.2.

[14] hifi, 2020. URL `https://hifieng.com/`. [Online; accessed Oktober 23, 2020].

[15] Christian Holz and Patrick Baudisch. Fiberio: a touchscreen that senses fingerprints. In *UIST '13*, 2013.

[16] J.F. ter Horst, J. Kuijper, V.H. Tsan, and A.C. Versluis. Levitating wafer tracking using an integrated sensor system, 2017. [Bachelor's thesis].

[17] Tzu-Chien Huang, Jian-Ren Ciou, Po-Hsun Huang, Kuo-Huang Hsieh, and Sen-Yeu Yang. Fast fabrication of integrated surface-relief and particle-diffusing plastic diffuser by use of a hybrid extrusion roller embossing process. *Opt. Express*, 16(1):440–447, Jan 2008. doi: 10.1364/OE.16.000440. URL http://www.opticsexpress.org/abstract.cfm?URI=oe-16-1-440.

[18] iXblue Photonics. Fbg sensor array. URL https://photonics.ixblue.com/store/fiber-bragg-gratings/fbg-arrays. [Online; accessed Oktober 23, 2020].

[19] S. H. Jeong, C. G. Choi, J. N. Oh, P. J. Yoon, B. S. Kim, M. Kim, and K. H. Lee. Low cost design of parallel parking assist system based on an ultrasonic sensor. *International Journal of Automotive Technology*, 11 (3):409–416, Jun 2010. ISSN 1976-3832. doi: 10.1007/s12239-010-0050-0. URL https://doi.org/10.1007/s12239-010-0050-0.

[20] D Kalymnios. Plastic optical fibres (pof). In Olivério D. D. Soares, editor, *Trends in Optical Fibre Metrology and Standards. NATO ASI Series (Series E: Applied Sciences)*, pages 747–770. Springer, Dordrecht, 1995.

[21] Peter Kan, Parham Yashar, Ciprian N. Ionita, Amit Jain, Stephen Rudin, Elad I. Levy, and Adnan H. Siddiqui. Endovascular coil embolization of a very small ruptured aneurysm using a novel microangiographic technique: Technical note. *Journal of NeuroInterventional Surgery*, 5(2), 2013. ISSN 17598478. doi: 10.1136/neurintsurg-2011-010154.

[22] Y Koike and M Asai. The future of plastic optical fiber. *NPG Asia Mater*, pages 22–29, 2009. doi: https://doi.org/10.1038/asiamat.2009.2.

[23] Coco Langens, Carmen Petsch, Daisy Robijns, and Myrthe Wiersma. Wafer tracking using an integrated and distributed system, 2018. [Bachelor's thesis].

[24] *HITRONIC POF SIMPLEX PE*. LAPP KABEL, June 2016. URL https://www.conrad.nl/p/lapp-28000001-pof-kabel-hitronic-pof-9801000-simplex-oranje-per-meter-609385. Product number 28000001.

[25] Liwei Lin, T K Shia, and C-J Chiu. Silicon-processed plastic micropyramids for brightness enhancement applications. *Journal of Micromechanics and Microengineering*, 10(3):395–400, jun 2000. doi: 10.1088/0960-1317/10/3/314. URL https://doi.org/10.1088/0960-1317/10/3/314.

[26] Shih-Jung Liu and Yu-Chin Huang. Manufacture of dual-side surface-relief diffusers with various cross angles using ultrasonic embossing technique. *Opt. Express*, 17(20):18083–18092, Sep 2009. doi: 10.1364/OE.17.018083. URL http://www.opticsexpress.org/abstract.cfm?URI=oe-17-20-18083.

[27] Zhe Liu, Sarah E. Sofia, Hannu S. Laine, Michael Woodhouse, Sarah Wieghold, Ian Marius Peters, and Tonio Buonassisi. Revisiting thin silicon for photovoltaics: a technoeconomic perspective. *Energy Environ. Sci.*, pages –, 2020. doi: 10.1039/C9EE02452B. URL http://dx.doi.org/10.1039/C9EE02452B.

[28] W. E. Knowles Middleton. Diffusion of ultraviolet and visible light by ground surfaces of fused quartz. *J. Opt. Soc. Am.*, 50(8):747–749, Aug 1960. doi: 10.1364/JOSA.50.000747. URL http://www.osapublishing.org/abstract.cfm?URI=josa-50-8-747.

[29] Newport. Fiber optic basics, (n.d.). URL https://www.newport.com/t/fiber-optic-basics. [Online; accessed 13-November-2020].

[30] Hyoung-Ghi Park and Dahl-Young Khang. High-performance light diffuser films by hierarchical buckling-based surface texturing combined with internal pores generated from physical gelation induced phase separation of binary polymer solution. *Polymer*, 99:1 – 6, 2016. ISSN 0032-3861. doi: https://doi.org/10.1016/j.polymer.2016.06.060. URL http://www.sciencedirect.com/science/article/pii/S0032386116305468.

[31] Rüdiger Paschotta. Plastic optical fibers, (n.d.). URL https://www.rp-photonics.com/plastic_optical_fibers.html. [Online; accessed 18-November-2020].

[32] Rüdiger Paschotta. Fibers, (n.d.). URL https://www.rp-photonics.com/fibers.html. [Online; accessed 18-November-2020].

[33] A. R. Patkar and P. P. Tasgaonkar. Object recognition using horizontal array of ultrasonic sensors. In *2016 International Conference on Communication and Signal Processing (ICCSP)*, pages 0983–0986, April 2016. doi: 10.1109/ICCSP.2016.7754294.

[34] PyraSied Xtreme Acrylic. Lichtdiffusers, (n.d.). URL https://www.pyrasied.nl/product-categorie/lichtdiffusers/. [Online; accessed 21-January-2021].

[35] PyraSied Xtreme Acrylic. Kies de juiste lichtdiffuser, (n.d.). URL https://www.pyrasied.nl/friksbeheer/wp-content/uploads/2018/05/Diffuserbrochure_NL_3de-druk_lowres.pdf. [Online; accessed 18-February-2021].

[36] D. Qian, W. Wang, and I. J. Busch-Vishniac. A method for measurement of multiple light spot positions on one position-sensitive detector (psd). *IEEE Transactions on Instrumentation and Measurement*, 42 (1):14–18, Feb 1993. ISSN 1557-9662. doi: 10.1109/19.206672.

[37] Xueguang Qiao and Michael A. Fiddy. Distributed optical fiber Bragg grating sensor for simultaneous measurement of pressure and temperature in the oil and gas downhole. In Achyut Kumar Dutta, Abdul Ahad Sami Awwal, Niloy K. Dutta, and Katsunari Okamoto, editors, *Active and Passive Optical Components for WDM Communications II*, volume 4870, pages 554 – 558. International Society for Optics and Photonics, SPIE, 2002. doi: 10.1117/12.475573. URL https://doi.org/10.1117/12.475573.

[38] Tom Reel. Mission solar producing solar panels, 2014. URL https://www.mysanantonio.com/business/local/article/Mission-Solar-producing-solar-panels-5768001.php#photo-6887994. [Online; accessed January 3, 2020].

[39] S. Shin, M. Kim, and S. B. Choi. Improving efficiency of ultrasonic distance sensors using pulse interval modulation. In *2016 IEEE SENSORS*, pages 1–3, Oct 2016. doi: 10.1109/ICSENS.2016.7808766.

[40] Jelle Snieder. Development of an air-based contactless transport demonstrator. Master's thesis, Technische Universiteit Delft, the Netherlands, 2017.

[41] SQS Vláknová optika. Fiber coupled microlens array, (n.d.). URL https://www.sqs-fiberoptics.com/fiber-coupled-microlens-array. [Online; accessed 13-January-2020].

[42] W. Suthabanditpong, M. Tani, C. Takai, M. Fuji, R. Buntem, and T. Shirai. Facile fabrication of light diffuser films based on hollow silica nanoparticles as fillers. *Advanced Powder Technology*, 27(2):454 – 460, 2016. ISSN 0921-8831. doi: https://doi.org/10.1016/j.apt.2016.01.028. URL http://www.sciencedirect.com/science/article/pii/S0921883116000443.

[43] Maria Temming, 2018. URL https://www.sciencenews.org/article/underwater-fiber-optic-cables-could-moonlight-earthquake-sensors. [Online; accessed Oktober 23, 2020].

[44] Thorlabs. Microlens arrays, (n.d.). URL https://www.thorlabs.de/newgrouppage9.cfm?objectgroup_id=2861. [Online; accessed 20-December-2019].

[45] Yoshihiro Tsukamoto. Tsukamoto. IEEE 802 POF Symposium, 2014. URL https://www.ieee802.org/3/GEPOFSG/public/Sep_2014/Tsukamoto_GEPOF_01b_0914.pdf.

[46] Eshan P Vagher. Contactless passive transport of thin solar cells. Master's thesis, Technische Universiteit Delft, the Netherlands, 2016.

[47] Yvonne Voorrips. The design of a distributed sensing system for contactless substrate transport. Master's thesis, Technische Universiteit Delft, the Netherlands, 2017.

[48] Phuc Vuong. *AIR-BASED CONTACTLESS ACTUATION SYSTEM FOR THIN SUBSTRATES*. PhD thesis, Technische Universiteit Delft, 2016.

[49] P. A. Wang. Industrial challenges for thin wafer manufacturing. In *2006 IEEE 4th World Conference on Photovoltaic Energy Conference*, volume 1, pages 1179–1182, May 2006. doi: 10.1109/WCPEC.2006.279391.

[50] Jasper Wesselingh. *Contactless positioning using an active air film*. PhD thesis, Technische Universiteit Delft, 2011.